

# **DEPOSITION OF SILICON NANOSTRUCTURES BY THERMAL CHEMICAL VAPOUR DEPOSITION**

by

**SFISO ZWELISHA KHANYILE**

Submitted in partial fulfilment of the

requirements of the degree of

**MASTER OF SCIENCE (NANOSCIENCE)**

UNIVERSITY of the  
WESTERN CAPE

in the

**DEPARTMENT OF PHYSICS  
UNIVERSITY OF THE WESTERN CAPE**

**SUPERVISOR : PROF. C. J. ARENDSE**

**CO-SUPERVISOR : DR. T. F. G. MULLER**

**JANUARY 2015**

This thesis is dedicated to:

The memory of my late loving father

**Samson Enoch Khanyile**

**(4 April 1944 – 9 September 1999)**



and

UNIVERSITY *of the*  
WESTERN CAPE

My loving and caring mother

**Agnes Sbongile Khanyile**

# **KEY WORDS**

---

## **SYNTHESIS AND CHARACTERIZATION OF SILICON NANOWIRES GROWN BY THERMAL CHEMICAL VAPOUR DEPOSITION**

**SFISO ZWELISHA KHANYILE**

Silicon nanowires

Thermal chemical vapour deposition

Scanning electron microscopy

Nanostructures

Fourier transform Infrared

Photoluminescence

Ultraviolet visible

Electron energy loss



# **ABSTRACT**

---

## **SYNTHESIS AND CHARACTERIZATION OF SILICON NANOWIRES GROWN BY THERMAL CHEMICAL VAPOUR DEPOSITION**

**SFISO ZWELISHA KHANYILE**

**M.Sc. Thesis, Department of Physics, University of the Western Cape**

In this thesis we report on the deposition of silicon nanostructures using a 3-zone thermal chemical vapour deposition process at atmospheric pressure. Nickel and gold thin films, deposited by DC sputtering on crystalline silicon substrates, were used as the catalyst material required for vapour-solid-liquid growth mechanism of the Si nanostructures. The core of this work is centred around the effect of catalyst type, substrate temperature and the source-to-substrate distance on the structural and optical properties of the resultant Si nanostructures, using argon as the carrier gas and Si powder as the source.

The morphology and internal structure of the Si nanostructures was probed by using high resolution scanning and transmission electron microscopy, respectively. The crystallinity was measured by x-ray diffraction and the high resolution transmission electron microscopy. For composition and elemental analysis, Fourier transform infrared spectroscopy was used to quantify the bonding configuration, while electron energy-loss spectroscopy in conjunction with electron dispersion spectroscopy reveals the composition. Photoluminescence and UV-visible spectroscopy was used to extract the emission and reflection properties of the synthesized nanostructures.

# **DECLARATION**

---

**I declare that**

## **“SYNTHESIS AND CHARACTERIZATION OF SILICON NANOWIRES GROWN BY THERMAL CHEMICAL VAPOUR DEPOSITION”**

is my own work, it has not been submitted for any degree or examination in any other university, and that all sources

I have used or quoted have been indicated and acknowledged by means of complete references.

**SFISO ZWELISHA KHANYILE**

**JANUARY 2015**

**SIGNED:**



# ACKNOWLEDGEMENTS

---

To God be, the glory, the honour and the praise for sustaining me throughout this journey and making this work successful.

***I would also like to thank the following people and organisations without whose assistance, advice and guidance, this thesis would not have been possible.***

Prof. Christopher Arendse (Department of Physics, University of Western Cape) for the excellent supervision of this thesis, his guidance, encouragement, understaning, support and his belief in my capabilities.

Dr. Theophilus Muller (Department of Physics, University of the Western Cape), for his excellent co-supervision, guidance, encouragement and assistance in many regards during the course of this work.

Electron Microscopy Unit (University of the Western Cape), for all the microscopy work done in the study.

Dr. David Motaung (Centre for Scientific and Industrial Research), for the co-supervision, encouragement, motivation and all the assistance with experimental work during the study.

The staff of the Physics Department, University of Western the Cape, for their hospitality, support and encouragement.

The staff of the National Nanoscience Teaching Platform at the University of the Western Cape for giving us the opportunity to be part of a new era in science and technology, and all the hospitality while we were under their care.

My mother and family for supporting me emotionally and otherwise during the long course of this work.

To my fiancée and son, THANK YOU for understanding, caring and supporting me throughout the journey without complaining of my absence.

My colleagues from the Nanoscience group and fellow Physics Department Postgraduate students for the friendship, support and motivation.

The Department of Science and Technology and the University of Western Cape for all the financial support during this study.



Thank you!!

---

# TABLE OF CONTENTS

1	INTRODUCTION AND LITERATURE REVIEW .....	3
1.1	INTRODUCTION.....	3
1.2	NANOTECHNOLOGY AND NANOMATERIALS.....	4
1.2.1	Importance of Silicon Nanowires (SiNWs) .....	5
1.3	DEVELOPMENTS ON THE SYNTHESIS AND GROWTH OF SILICON NANOWIRES.....	11
1.3.1	Top-Down Approach .....	11
1.3.2	Bottom-Up Approach.....	12
1.4	THE VLS GROWTH MECHANISM.....	13
1.4.1	The VLS Growth Model .....	14
1.4.2	The Metal Catalyst.....	15
1.4.3	The Si Vapour Source.....	17
1.4.4	Nucleation .....	18
1.4.5	Steady Growth of Si Nanowires .....	20
1.4.6	Termination of Axial Growth of SiNWs .....	22
1.5	SiNW GROWTH TECHNIQUES .....	23
1.5.1	Chemical Vapour Deposition (CVD).....	23
1.5.2	Plasma Enhanced Chemical Vapour Deposition (PECVD).....	25
1.5.3	Annealing in Reactive Atmosphere .....	27
1.5.4	Evaporation of Silicon Monoxide (SiO) .....	28
1.5.5	Molecular Beam Epitaxy (MBE) .....	29
1.6	AIMS AND OUTLINE .....	30
1.7	REFERENCES .....	32
2	EXPERIMENTAL TECHNIQUES .....	36
2.1	INTRODUCTION.....	36
2.2	SAMPLE PREPARATION.....	36
2.2.1	Substrate preparation .....	36
2.2.2	Au and Ni thin film sputter deposition .....	37
2.2.3	Thermal Chemical Vapour Deposition (TCVD) of Si-Nanostructures .....	38
2.3	CHARACTERIZATION TECHNIQUES .....	46
2.3.1	Scanning Electron Microscopy (SEM) .....	46

---

2.3.2	X-Ray Diffraction (XRD) .....	54
2.3.3	Fourier Transform Infrared Spectroscopy .....	60
2.3.4	Transmission Electron Microscopy .....	64
2.3.5	Optical Characterization Techniques .....	70
2.4	REFERENCES .....	77
3	RESULTS AND DISCUSSION .....	79
3.1	INTRODUCTION .....	79
3.2	EXPERIMENTAL .....	81
3.3	COMPOSITION AND STRUCTURAL PROPERTIES .....	84
3.3.1	The Effect of Metal Catalyst on Si Nanostructure Growth.....	84
3.3.2	The Effect of Temperature on the Growth of Si-Nanostructures .....	92
3.3.3	Effect of Source-to-Substrate Position on Si Nanofibre Growth.....	111
3.3.4	TEM Characterization of Si-Nanostructures .....	122
3.4	OPTICAL PROPERTIES of SiO <sub>2</sub> NANOWIRES .....	133
3.4.1	Photo-Luminescence (PL) of SiO <sub>2</sub> Nanowires .....	134
3.4.2	UV-VIS-NIR Spectroscopy of SiO <sub>2</sub> Nanowires.....	136
3.5	CONCLUSION .....	139
3.6	REFERENCES .....	141
4	SUMMARY AND CONCLUSION TERN CAPE .....	146

---

# CHAPTER 1

---

## 1 INTRODUCTION AND LITERATURE REVIEW

---

### 1.1 INTRODUCTION

The current worldwide energy and environmental crisis is an indication for the need of sustainable and efficient power generation technologies. The development of green technologies such as solar photovoltaic (PV) power has been greatly hindered by the low efficiencies and high production costs of existing solar cells [1.1]. Strategic interventions to alleviate such challenges involve intense research of alternative lower-cost materials that can enhance solar PV performance.

In recent years, one-dimensional silicon-based nanostructures such as silicon nanowires (SiNWs) have attracted a lot of research interest due to their unique and novel properties associated with the nanoscale dimension of such structures. These novel optical, electrical and mechanical properties have rendered SiNWs as ideal candidate materials for nanodevice fabrication for use in the electronic and photovoltaic industry [1.2]. The Si nature of such novel structures makes their integration within the already developed Si-based technologies feasible. The systematic incorporation of SiNWs with enhanced antireflective (AR) and absorption properties can help to alleviate and improve the low efficiencies of existing solar cells.

The synthesis of SiNWs can be achieved using several techniques which include; chemical vapour deposition (CVD), plasma enhanced CVD, annealing in reactive atmosphere, thermal evaporation, molecular beam epitaxy and other solution based

---

methods. In this thesis, the thermal chemical vapour deposition technique was used for the synthesis of SiNWs at atmospheric pressure. Safety, simplicity and low cost were among some of the factors that influenced the choice of this technique to be used.

## 1.2 NANOTECHNOLOGY AND NANOMATERIALS

In general, nanotechnology can be described as a diverse field of technology which involves the manipulation, fabrication and applications of nanostructures and nanomaterials. This technology (nanoscience) encompasses the study of basic physical properties and phenomena of nanostructures and nanomaterials including the understanding of their applications [1.1]. The prefix nano means  $10^{-9}$  hence nanostructures have a size range of about a few to several nanometres ( $10^{-9} - 10^{-7}$  m). These novel structures have dimensions ranging from zero dimensional (quantum dots and nanoparticles), to one dimensional (nanowires and nanotubes), and even two dimensional (nano-film) structures. These dimensional variations are not just shape variations but have a bearing on the physical properties of these materials [1.2].

Recently, there have been huge developments and research interests on several nanomaterials such as metal nanoparticles, SiNWs, carbon nanotubes (CNTs), metal oxide nanorods and single layer graphite (graphene). These novel structures possess unique and distinct structural, optical and electrical properties in comparison to their bulk or micron counterparts, hence the huge interests. CNTs have attracted a lot of interests since the beginning of the 90s when the facile synthesis of CNTs was reported and were believed to form the core of future generation electronic devices [1.3]. However, silicon (Si) has always been at the core of all technological

---

advancements made in semiconductor technology and electronic devices [1.4]. This is among the reasons promoting SiNWs to be the most suitable candidates for electronic applications since they can be easily integrated into existing Si devices. It is therefore crucial to study such materials at atomic scale in order to develop a fundamental understanding of the resulting unique properties and enhance the designing and integration of such structures into devices.

### ***1.2.1 Importance of Silicon Nanowires (SiNWs)***

SiNWs can be defined as one-dimensional wire, rod, whisker and cone-like structures that have a diameter of less than a 100 nm. In the quest to improve the cost-efficiency of electronic devices, the quantum confinement effects associated with nano-scale devices form a crucial part of microelectronic device design. Nano-scale semiconductor wires have therefore attracted a lot of attention as a result of their possible applications in mesoscopic research, nanophotonics, nanoelectronics, nano devices, chemical sensors and biological systems [1.5, 1.6].

#### ***1.2.1.1 Research developments in SiNWs***

The “first known” publication on Si wire growth which marked the first phase of Si wire research, was written by Treuting and Arnold in 1957 [1.7] whereby they presented their successful growth of Si whiskers (filamentary Si crystals) with macro dimensions. A few (7) years later, there was a drastic improvement in Si wire research which was marked by a major breakthrough in Si wire synthesis made by Wagner and Ellis [1.8]. Through their work, the vapour-liquid-solid (VLS) growth mechanism was born, paving way to a new research field which even today is the most popular synthesis method for Si wires. This new era lasted for almost a

decade, through which more fundamental aspects of VLS Si wire growth were discovered and thereafter became dormant.

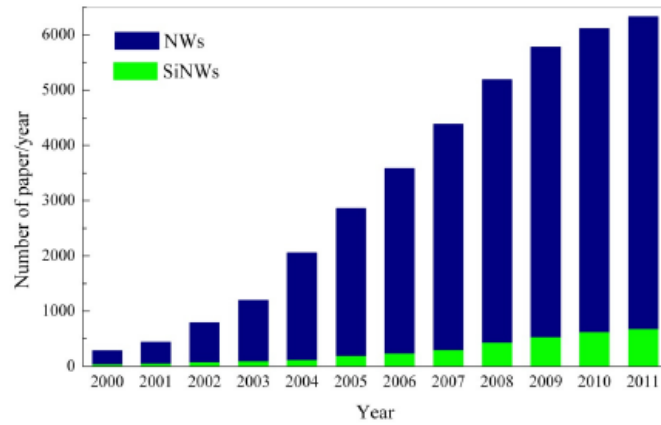


**Figure 1.1:** A graphical presentation showing the number of publications on nanowires and SiNWs specifically [1.9].

It was not until the mid-90s that the second phase of research on Si wires, with nano-dimensions (SiNWs) began as a result of advances in microelectronics. In this era, SiNW publications started outnumbering those on Si whiskers [1.9]. Since then, and over the last decade, there has been a huge increase on NW publications making it an active field of nanotechnology [1.9]. Most of the work done on SiNWs entails, the fundamental growth, physical properties, applications and models of metallic, semiconducting NWs. In the electronics industry, the majority of SiNW research focuses on the electrical properties of SiNWs, since they can be easily incorporated into existing electronic devices [1.9, 1.10].

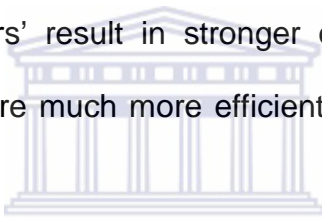
### **1.2.1.2 The novel physical properties and phenomena of SiNWs**

Developments in nanotechnology and quantum physics demonstrate that, materials do change their properties as they become smaller in size (nanoscale) and quantum physical effects such as quantum confinement become more dominant and apparent in determining material properties. At the nano-scale ( $10^{-9}$  m), a crystal cannot be

---

defined as an infinite periodic structure since boundary conditions and surface effects become very crucial when the size of the crystal is reduced to a very small size. Hence surface passivation, size and shape play a very huge role in determining the optical and electronic properties of nanostructures [1.11].

Consequently, silicon nanocrystals can emit light in the visible range due to quantized energy levels for electrons and holes, which assume higher energy levels within their respective energy bands when the size of the crystal is reduced. In silicon nanocrystals, the energy bands are different from those of their bulk counterpart since bulk silicon energy bands are based on principles of an infinite periodic lattice. Furthermore, the changes in band structure and the strong confinement of charge carriers' result in stronger overlapping of wave functions hence the optical transitions are much more efficient in silicon nanocrystals than in bulk silicon material.



Enhanced optical absorption properties within the visible and near-infrared regions, have been observed in crystalline SiNWs when compared to crystalline thin films. It has been demonstrated that, the band gap of SiNWs can be engineered by tuning the nanowire diameter within the range of 1-7 nm [1.12], which introduces strain [1.13]. Furthermore, amorphous SiNWs (a-SiNWs) and nanocones (NCs) when compared to a-Si thin films have exhibited enhanced absorption in the range between 400 to 800 nm. The surface of these a-SiNWs can be passivated and this passivation of surface defects is essential for improving the electron mobility in nanowire devices [1.13].

As the SiNW diameter is reduced to < 10 nm, the Si band gap gets transformed from an indirect to a direct band gap resulting in photoluminescence (PL) and electroluminescence (EL) of the SiNWs as a consequence of quantum confinement

---

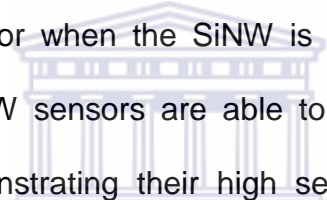
effects [1.10]. Experimentally, quantum confinement effects in nanostructured Si, were first reported by Canham (1990) [1.14] and Lehman and Gosele (1991) [1.15], where by electrochemical etching was used to synthesize c-Si nanostructures with visible luminescence at room temperature.

The unique mechanical properties of SiNWs have attracted a lot of interest due to their potential applications as building blocks for nano-devices. SiNWs have been found to exhibit superior mechanical properties than bulk Si such as the elastic modulus and fracture stress [1.16]. When etching a Si wafer to produce SiNWs, the synthesized NWs exhibit lower stiffness than the bulk Si as a result of the increased surface-to-volume ratio. This observation shows that in NWs, the surface layer has an elastic modulus and Eigen-strains different to those of bulk Si [1.17]. Lee and Rudd [1.18], demonstrated in their work on (100) SiNWs that the Young's modulus decreases as the surface to volume ratio increases, and the steep decline observed between 2 - 2.5 nm was attributed to compressive surface stress [1.18]. The study and fabrication of novel mechanical nanostructures with reduced Young's moduli and enhanced elastic properties has become a prominent field of research. This initiative seeks to resolve the problem of plastic deformation in materials which directly leads to fracture through broadening of the elastic region. However, these observed effects on pristine SiNWs cannot directly be linked to oxidised SiNWs since at the nanoscale, different surface treatments yield varying mechanical properties. Due to the increased surface to volume ratio, it follows that the nanoscale signature is encrypted on the surface of the SiNWs [1.17].

### **1.2.1.3 Potential applications of SiNWs**

The novel physical properties and phenomena of SiNWs have reinforced the idea of Si being the ideal material for present and future electronics, hence the rapid growth of SiNW research and development. SiNWs have a wide range of potential applications in several fields such as SiNWs-FETs, photovoltaic devices, lithium-ion batteries and in thermoelectric devices.

SiNW-FETs have a high sensitivity and surface to volume ratio which enables them to be applicable in a range of nanodevices such as pH sensors, gas sensors and biological sensors [1.10]. The sensing mechanism of the SiNWs relies on the changes in its electrical conductance which occurs when there is a loss or gain of electrons on the Si surface, or when the SiNW is exposed to charged biological molecules. Furthermore, SiNW sensors are able to achieve the detection limit of femtomolar molecules, demonstrating their high sensitivity due to the enhanced surface to volume ratio.



UNIVERSITY of the  
WESTERN CAPE

In solar cells and photovoltaic devices, the enhanced photon absorption capability of SiNWs is essential. During the fabrication of a SiNW solar cell, the SiNWs are doped such that they form p-i-n coaxial SiNWs such that each SiNW can act as a solar cell. Tian *et al.* [1.19], demonstrated using a single coaxial SiNW p-i-n junction solar cell with an efficiency of about 3.4% while efficiencies > 10% have been achieved by several groups using arrays of SiNW solar cells [1.10]. As mentioned previously, enhancement of SiNW solar cell performance can be achieved through surface passivation, limiting interfacial recombination.

Lithium-ion batteries are the most fundamental power source for modern portable devices such as cellular phones, laptops, camcorders, digital cameras etc. Conventionally, Li-ion batteries utilise graphite as the anode material which has a

capacity of  $372 \text{ mA.hg}^{-1}$  and has a lower performance capacity than SiNW anodes. Other materials with higher theoretical capacities include Sn, Al and Si having the highest capacity of about  $4200 \text{ mA.hg}^{-1}$  in the  $\text{Li}_{4.4}\text{Si}$  composition [1.20]. This high performance capacity results in even longer life cycles and enhanced resistance to pulverization during cycling. Several works published previously, have suggested that the enhanced cycling ability of amorphous Si compared to crystalline Si, can be attributed to the lower volume expansion and higher potential of a-Si when reacting with  $\text{Li}^+$  ions [1.21]. Furthermore, Cui et al [1.22], observed a life cycle extension in Li-ion batteries of about a 100 cycles when crystalline-amorphous SiNWs (core-shell), were incorporated as anodes for Li-ion batteries.

SiNWs have been found to possess a high thermal conversion efficiency, which is about a 100 times that of bulk Si. This characteristic behaviour renders SiNWs as one of the ideal materials for a range of thermoelectric device applications [1.23].

The electrical conductivity of SiNWs is comparable to that of bulk Si, while the thermal conductivity is about  $\sim 1.6 \text{ Wm}^{-1}\text{K}^{-1}$ , which is much lower than the  $150\text{Wm}^{-1}\text{K}^{-1}$  of bulk Si. Hochbaum et al [1.23], in his work illustrated that even lower thermal conductivity of SiNWs can be achieved by introducing structural defects and also by decreasing the SiNW diameter, which reduces phonon transport.

As a result of the rapidly increasing research, the novel properties and the exploration of a wide range of possible applications of SiNWs, the development of future technology hinges largely on SiNWs. As highlighted earlier on, the synthesis method and surface passivation are some of the key factors affecting properties and applications of SiNWs. It is therefore crucial to focus more research and growth into the SiNW field in order to achieve large-scale and high quality SiNWs at sustainable costs.

## 1.3 DEVELOPMENTS ON THE SYNTHESIS AND GROWTH OF SILICON NANOWIRES

In the last few decades, extensive research work has been done on one-dimensional, Si nanostructures such as SiNWs in order to improve the understanding of the various growth methods and formation of SiNWs. The common processes used for fabrication of SiNWs can be divided into, top down and bottom down approaches shown in figure 1.2. These two approaches form the basis of all the SiNW growth methods that are being studied extensively.

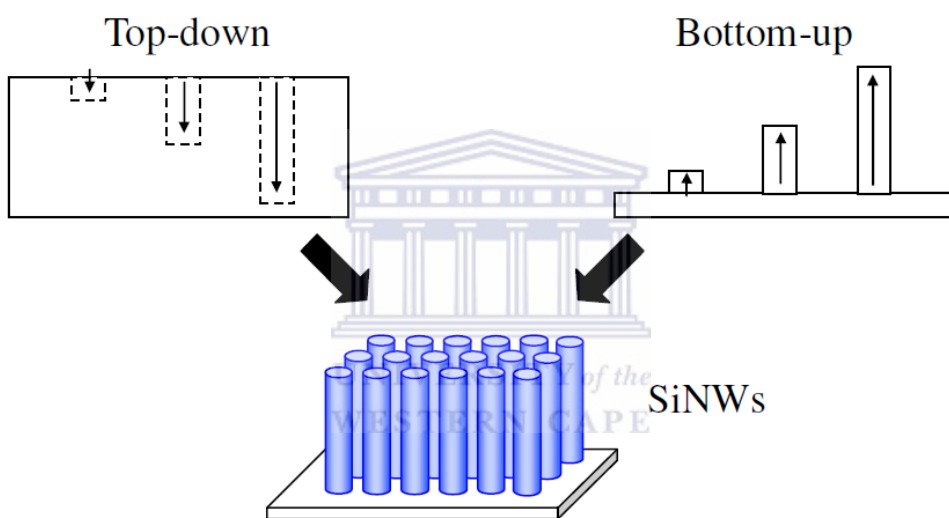


**Figure 1.2:** a schematic showing the top-down and bottom-up growth of SiNWs.

### 1.3.1 Top-Down Approach

This process usually involves etching of a Si substrate or an already existing layer of Si in order to form one-dimensional Si nanostructures. During the top-down approach, the etching process can be classified as either a dry or wet etching process. The dry etching process for SiNWs includes techniques such as electron beam lithography, reactive ion bombardment and plasma etching. Furthermore, these techniques require complex and costly optical equipment which can be fragile. In comparison, wet etching utilises liquid chemicals for etching which are easy and

safe to use such as hydrofluoric acid (HF) which is used for etching ( $\text{SiO}_2$ ). A simple illustration of this process was demonstrated by Peng *et al* [1.24], where by a silver (Ag) coated Si substrate was electro etched in HF/Fe( $\text{NO}_3$ ) solution [1.24]. During this process, Si is oxidised by the reduction of  $\text{Fe}^{3+}$  to  $\text{Fe}^{2+}$  yielding  $\text{SiO}_2$  surrounding the Ag. The HF is then used to etch the  $\text{SiO}_2$  away and further form SiNW arrays that are vertically aligned hence making the top down approach ideal for synthesis of vertically aligned and uniform SiNW arrays. However, limitations such as structural defects, impurities and surface imperfections of the synthesized SiNWs still hinder the development and applicability if this approach.

### **1.3.2 Bottom-Up Approach**

The bottom-up approach involves the formation of SiNWs from the atomic level into one-dimensional structures using various Si precursors. There are various SiNW growth techniques which utilise this approach include thermal evaporation, laser ablation, solution based growth, CVD, MBE and magnetron sputtering. The main distinction between all these growth techniques is the type of Si source used in each technique. The source material for laser ablation is a solid target composed of Si-Fe elements while solution based growth utilizes monophenylsilane ( $\text{SiH}_2\text{C}_6\text{H}_8$ ) as the source in order to achieve one-dimensional growth. During CVD growth, the commonly used sources are Si vapour containing gases like  $\text{SiH}_4$  or  $\text{SiCl}_4$  and even Si powder [1.25].

During bottom-up synthesis, the actual growth of SiNWs can be attributed to either of the several SiNW growth mechanisms which include, vapour-liquid-solid (VLS), vapour-solid-solid (VSS), solid-liquid-solid (SLS), solution-liquid-solid , oxide assisted growth (OAG), sulphide assisted growth, and template based growth. However, the VLS growth mechanism is the most commonly used mechanism [1.10]. Contrary to

the top-down approach, SiNWs synthesized using bottom-up approaches exhibit less structural defects and produce high quality c-SiNWs as a result of controllable growth conditions [1.26]. The naturally crystallinity of metal catalyst structure can be used to induce the formation of monocrystalline SiNWs , while epitaxially grown SiNWs can be achieved by using an etched c-Si substrate to remove oxide layer. When using the bottom-up approach, in situ doping of NWs can be achieved by adding dopants in the gas phase during CVD growth. Furthermore, this growth approach is capable of producing SiNWs with very small diameters, with Ma *et al.* [1.27], having reported the smallest diameter NW to be 1.3 nm through the OAG growth mechanism during thermal evaporation of  $\text{SiO}_2$  powder [1.27].

## 1.4 THE VLS GROWTH MECHANISM

The VLS mechanism is a growth model for one-dimensional structures which utilizes a metal catalyst to induce the nucleation and growth of one-dimensional structures such as whiskers, rods and wires. This growth model was proposed and promoted for wider use by Wagner in 1964 [1.8] and has developed through research over time.

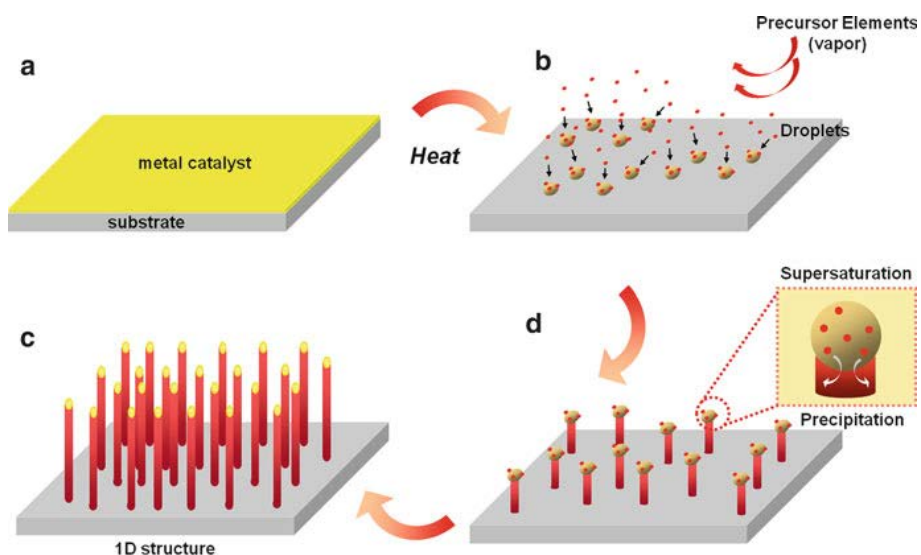


**Figure 1.3:** Shows the VLS growth mechanism of SiNWs on a Si substrate using a metal catalyst.

### 1.4.1 The VLS Growth Model

As indicated previously, the VLS mechanism utilizes a metal catalyst in order to initiate and control the growth of SiNWs. This growth model can be classified into three stages being; alloying, nucleation and growth as shown in figure 1.4(a). The first stage begins at elevated temperatures where by, the metal catalyst thin film dewets and alloys with the Si substrate to form liquid alloy droplets. The second stage, nucleation, commences as a result of the Si precursors in vapour form being adsorbed by the metal-Si alloy droplet. Due to the high growth temperatures and vapour pressure fluctuations, continuous adsorption of the vapour Si precursors occurs resulting into supersaturation of the liquid-alloy droplet. This supersaturation eventually results in precipitation of SiNWs at the liquid-solid interface, which is the growth stage. A schematic illustrating the VLS growth model is shown in figure 1.4 (b) as demonstrated by Schmid *et al.* [1.28] in his works, where by an in-situ SEM investigation was conducted on Au-catalyzed SiNWs.

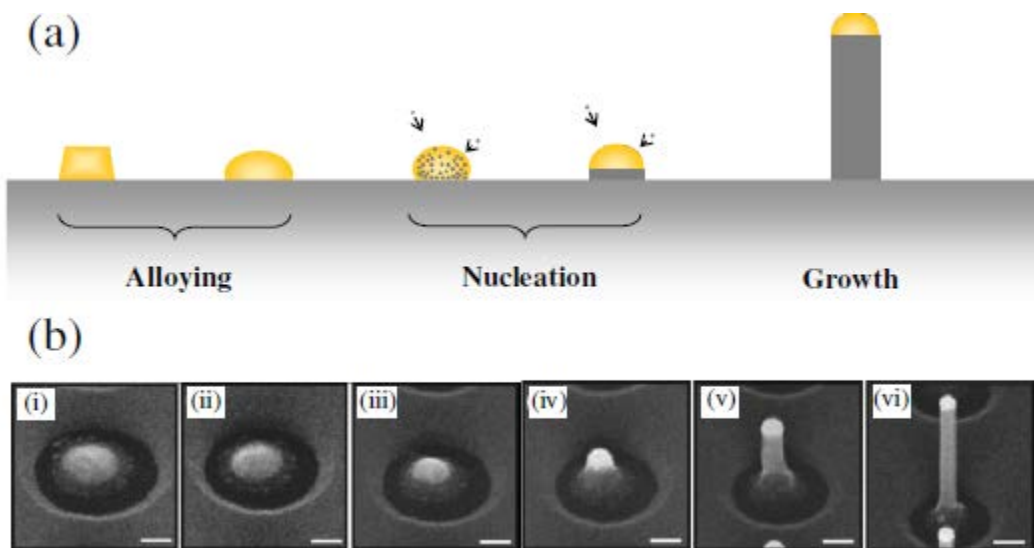


**Figure 3.4:** (a) VLS growth of SiNWs. (b) in-situ FESEM of SiNW growth using Au-catalyst. (scale bar = 100 nm) [1.28].

---

Furthermore, figure 1.4 (b) clearly shows the stages (i) to (vi) which represent the general transition from a simple metal catalyst coated substrate to a point where by the is SiNW growth. In order to fully comprehend the VLS growth mechanism, each of the different stages will be discussed individually in the following sub-section.

### **1.4.2 The Metal Catalyst**

The VLS growth mechanism is one of the most common growth methods for SiNWs. During the VLS growth process, a metal catalyst on its own or through alloying forms a nano-droplet which then plays a crucial role by providing an interface for Si precursor adsorption and hence becoming the nucleation site for SiNWs. One of the unique characteristics of nanowires grown using this method is the presence of a spherical metal eutectic particle at the tip of the nanowire [1.29]. Gold (Au) is one of the most frequently used metals for catalytic growth of NWs, including other metals such as nickel (Ni), aluminum (Al), copper (Cu), silver (Ag) etc. Furthermore, Zhou *et al.* [1.31] in his work showed that the diameter of the grown SiNWs is determined by the size of the metal catalyst nano-droplet from which they nucleate.

Most commonly, a metal catalyst thin film is deposited on the Si substrate using any of the physical vapour deposition methods and this thin film becomes the source for the catalyst material. In order to form the nano-droplet arrays on the substrate, a thermally-induced dewetting process of thin films is used. In metallic thin-films, solid-state dewetting is driven by the changes in surface energies of the thin film and the interface between thin film and substrate leading to the formation of liquid nano-droplets at temperatures that are even lower than melting point of the thin film. Some metals such as Ni, Au, Ag and Co have low activation energies enhancing metal atom migration on  $\text{SiO}_2$  due to weak interactions [1.31].

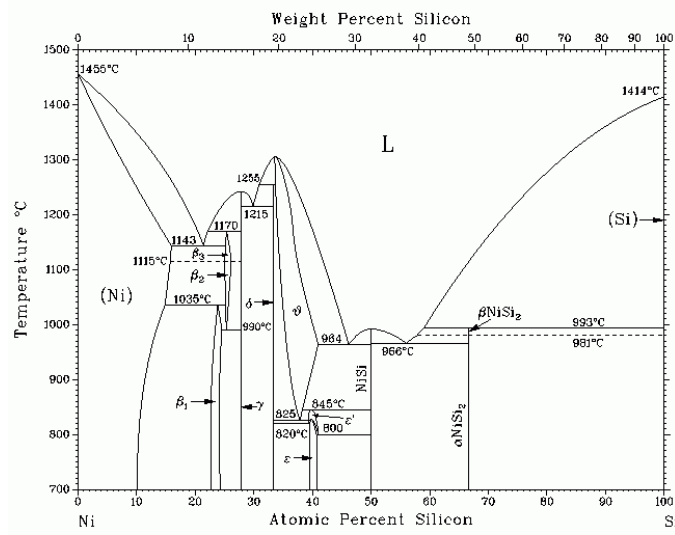
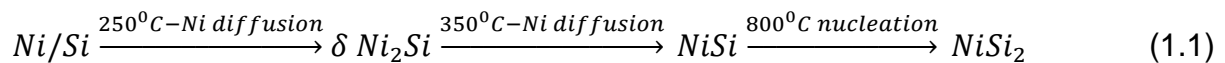


**Figure 1.5:** Phase diagram of Ni-Si binary alloy [1.32].

Recently, Ni has become the favourable catalyst material for SiNW growth due to it being thermodynamically compatible with the VLS growth of SiNWs. The choice of an ideal catalyst and temperature for the growth of SiNWs can be guided using the phase diagram of the metal-Si alloy. The Ni-Si alloy phase diagram shown in figure 1.5 indicates eutectic reactions at temperatures of about 964 °C, 966 °C, 1143 °C and 1215 °C where by SiNW growth occurs. As indicated in this bulk binary Ni-Si diagram, the eutectic point for  $\text{NiSi}_2$  is 993 °C which means that for nano-sized particles, the formation of the  $\text{NiSi}_2$  eutectic compound can occur at even lower temperatures than the 993 °C for bulk materials. During VLS growth, the vapour phase is highly saturated with Si atoms which have a high solubility in  $\text{NiSi}_2$  hence upon reaching the liquid droplet surface, these atoms get absorbed and diffuse within the nano-droplets. Continuous absorption of the Si atoms causes supersaturation of the droplet resulting in SiNW precipitation [1.33].

One of the advantages of using Ni as a catalyst is that, Ni-Si phases start forming at relatively low temperatures such as 400 °C. At this phase,  $\text{NiSi}$  forms and has a

lower resistance compared to the other phases. As the temperature increases, phase formation progresses and resistance increase in the sequence: Ni<sub>2</sub>Si (25  $\mu\Omega\cdot\text{cm}$ ) to NiSi (14  $\mu\Omega\cdot\text{cm}$ ) to NiSi<sub>2</sub> (40  $\mu\Omega\cdot\text{cm}$ ) while the silicidation sequence is:



At higher temperatures, the NiSi forms NiSi<sub>2</sub> which has a higher resistance and higher solubility of Si promoting higher absorption of Si precursors which consequently results in rapid growth of SiNWs.

According to Schmidt *et al.* [1.34], metal catalyst can be classified based on their interactions, such as, Au-like metals, silicide alloying metals, and low Si solubility metals. The low melting temperature of low solubility metals such as Sn, In, and Ga makes them the most favourable metals. In electronic applications, Indium (In) is known for inducing p-type doping of SiNWs and has a low melting point of about 156.6 °C hence SiNW growth is expected at such low temperatures. However, as a result of its low solubility ( $\sim 1 \times 10^{-15} \text{ cm}^2/\text{s}$ ), such a metal catalyst requires higher Si precursor pressure in order to achieve SiNW growth. The surface of the In nano-droplet readily oxidises into indium oxide (In<sub>2</sub>O<sub>3</sub>) which hampers the diffusion of Si precursors [1.35].

### 1.4.3 The Si Vapour Source

During SiNW synthesis, several growth techniques as highlighted previously can be used. The choice of the Si precursors is determined largely by the type of growth technique used and other factors such as anticipated growth temperature. Some of the most common Si precursors used during the synthesis of SiNWs include, the derivatives of silane (SiH<sub>4</sub>, Si<sub>2</sub>H<sub>6</sub>, Si<sub>3</sub>H<sub>8</sub>, SiH<sub>2</sub>C<sub>12</sub>), pure Si powder, SiO powder and

---

even bulk solid Si targets. In the early days, Wagner and Ellis [1.8] used  $\text{SiCl}_4$  for the synthesis of Si nano-whiskers at higher temperatures in order to thermally decompose the  $\text{SiCl}_4$ .

In recent times,  $\text{SiH}_4$  has become the dominant precursor owing to its lower decomposition temperature and absence of chlorine elements. Furthermore, the  $\text{SiH}_4$  precursor is more ideal for low-temperature CVD and even permits the use of variable types of substrates due to the low growth temperature. Other precursors such as Si powder are more appropriate for high temperature CVD due to their higher vaporization temperatures. Si powder has been found to be one of the most cost-effective sources for producing SiNWs on a large scale [1.9]. A small portion of Si powder is placed in a multi-zoned tube furnace whereby it is heated at high temperatures and thermally evaporated. In order for vaporization of the powder and growth to occur, a temperature gradient of about  $1350\text{ }^\circ\text{C}$  to  $900\text{ }^\circ\text{C}$  is necessary along the furnace tube. The Si powder is placed on the hotter end in order to induce vaporization of Si atoms which get carried downstream onto the substrate by an inert gas such as argon (Ar), supplied into the tube. As the Si atoms flow downstream, collisions and reactions occur such that upon reaching the cooler zone, Si atoms get absorbed and supersaturate the liquid nano-droplet resulting in nanowire growth [1.36].

#### **1.4.4 Nucleation**

When the Si atoms get absorbed into the eutectic alloy nano-droplet continuously, saturation occurs. From absorption at the surface of the nano-droplet, the Si atoms diffuse within the droplet towards the liquid-solid interface and this period is known as the incubation time. Continuous absorption of Si from the vapour precursor leads

to supersaturation at the droplet/Si-substrate interface which results in the precipitation and growth of SiNWs. This process is called nucleation and it marks the first stage of SiNW growth.

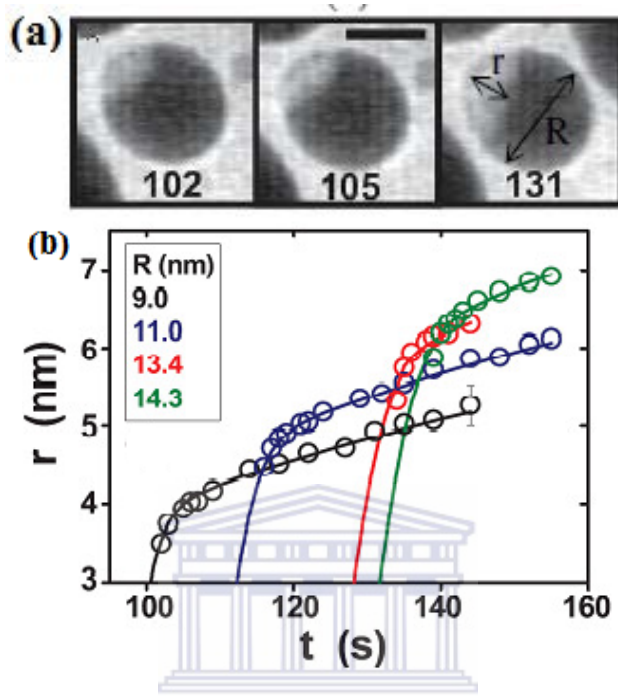


**Figure 1.6:** Shows (a) the BF TEM images of a precipitating SiNW at after 102 s, 105 s and 131 s (scale = 10 nm). (b) a plot of the linear variation  $r$  (length) of Si nuclei against time for different radii  $R$  of droplets [1.37, 1.38].

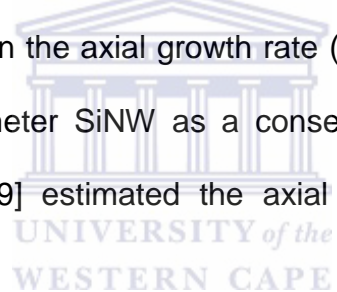
Hoffman *et al.* [1.37] and Kim *et al.* [1.38] conducted an in-situ investigation of the SiNW nucleation process. In their work, Au catalysed NW nucleation was monitored using a transmission electron microscope (TEM) with ultra-high vacuum. The summary of observations made at different time intervals are presented in figure 1.6 using the bright field (BF) TEM images (a). The BF images acquired at time,  $t = 102$ , 105 and 131 s, show the variation in the radial length  $r$ , as time progresses. This observation clearly shows the time-delay from when the Si precursors are supplied until radial growth of SiNWs occurs. A graphical presentation of the process is shown in figure 1.6 (b), where by the measured linear elongation  $r$  in nanometres, of the Si nuclei was plotted against the elapsed time  $t$  in seconds. It is observed from the

---

graph that beyond a certain critical point, the linear growth increases rapidly until it reaches a steady growth rate where it stabilizes. Furthermore it was observed that catalyst droplets with a bigger diameter  $R$ , took a longer nucleation time and slower growth rate.

#### **1.4.5 Steady Growth of Si Nanowires**

In the previous section, the different stages of SiNW growth have been highlighted as nucleation, rapid growth, steady growth and termination of NW growth. As indicated earlier, the continuous absorption of Si atoms by the catalyst nano-droplet leads to supersaturation at the liquid/solid interface which results in growth of SiNWs. As the growth progresses from being rapid initially, it reaches a steady stage where by there is no change in the axial growth rate ( $dR_{\text{axial}}/dt = 0$ ) observed on the NW resulting in a fixed diameter SiNW as a consequence of the stable catalyst diameter. Kikawa *et al.* [1.39] estimated the axial growth rate  $R_{\text{axial}}$ , using the relation:



$$R_{\text{axial}} = \frac{l_{\text{NW}}}{t_d} \quad (1.2)$$

Where by  $l_{\text{NW}}$  and  $t_d$  represent the NW length and deposition time respectively. To improve the accuracy of this approximation, it is crucial to incorporate the nucleation time  $t_{\text{nuc}}$  of that particular catalyst being used as presented by Schmidt *et al.* [1.34]:

$$R_{\text{axial}} = \frac{l_{\text{NW}}}{t_d - t_{\text{nuc}}} \quad (1.3)$$

As the SiNWs undergo axial growth, some of the Si precursor species get deposited and absorbed through the walls of the precipitated NWs. This process may result in radial growth of the NWs and hence the diameter of the NWs may increase or in

some cases result in tapered structures (non-uniform diameter). This radial growth  $R_{radial}$ , can be approximated using the NW radius  $r_{NW}$ , in the relation:

$$R_{radial} = \frac{r_{NW} - r_0}{t_d} \quad (1.4)$$

Where by  $r_0$  is the initial NW radius before radial growth. According to Schmid et al. [1.34], the  $R_{radial}$  is about ~ 2 orders of magnitude smaller than  $R_{axial}$ .

During VLS-SiNW growth, there are several kinetic processes which can affect the growth rate of NW. These kinetic processes are shown in figure 1.7 as (1) Si atoms transportation in vapour phase, (2) adsorption and absorption at the vapour/liquid interface, (3) diffusion of Si within liquid phase, and (4) incorporation of atoms in a crystal lattice.

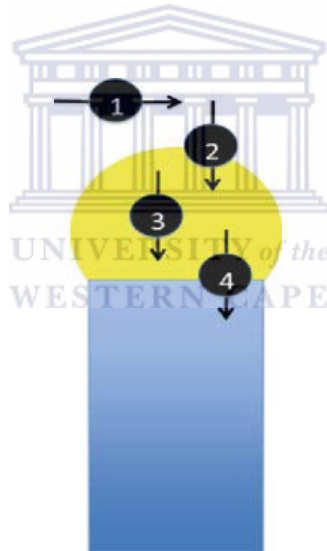


**Figure 1.7:** A schematic diagram showing the various processes involved in during VLS growth of SiNWs [1.40].

According to Choi et al. [1.40], the complexity of determining the actual process (es) that is responsible for determining the growth rate of SiNW as shown in figure 1.7 can be attributed to the three phases, the two interfaces and the chemical reactions involved during NW growth. Based on experimental evidence, He managed to individually isolate and eliminate each process in the following manner. Due to the high diffusivity of Si in liquefied metals and the fixed catalyst shape, step (3) was

found to have negligible contribution to the growth rate. For step (1), it is expected that the diffusion coefficient in the gaseous phase, be governed by the power law:  $D = D_0(T/T_0)^n(P/P_0)$ , where  $n=1.5\sim2$  [1.41, 1.42]. However, experimentally, this is not always observed hence step (1) cannot be considered as a rate-limiting process. Considering step (2) as a rate-limiting factor implies that the growth is proportional to the partial pressure of reactant gas which is in disagreement with the notion that, the growth process involves two activated processes in series [1.40]. This observations led to the conclusion that, the growth rate solely depends on the supersaturation hence step (4) can be considered as the rate determining factor since it involves the incorporation of atoms into the crystal lattice [1.40].

#### **1.4.6 Termination of Axial Growth of SiNWs**

During Axial growth of SiNWs, when the temperature is dropped below a certain critical point or all the metal catalyst is used up, axial growth is terminated [1.43].

During SiNW growth, the growth temperature is a vital parameter since it is responsible for maintaining the thermodynamic stability of the metal catalyst in its liquid phase. Schmidt and Gosele [1.44], observed that, during steady state growth, a slight drop in substrate temperature results in a drop of the NW growth rate which then explains the link between critical temperature and termination of growth. These observations show that, as the temperature is reduced, the growth rate decreases until there is no more growth observed below a certain critical temperature.

Furthermore, termination of NW axial growth can be induced by the evolution of the catalyst or migration through evaporation or incorporation of the catalyst into the NW matrix [1.45, 1.46]. These processes can result in size reduction of the catalyst which further promotes the diffusion of the catalyst from the tip of the nanowire into the

---

body. This migration of the catalyst results in the formation of NWs with sharp pointed needle-like tips.

## 1.5 SiNW GROWTH TECHNIQUES

### 1.5.1 *Chemical Vapour Deposition (CVD)*

CVD is one of the oldest, dominant and fast developing growth technique used for the synthesis of SiNWs using the VLS mechanism. In this technique, a gaseous or vaporised Si precursor such as SiH<sub>4</sub>, SiCl<sub>4</sub> and vaporised pure Si powder can be used as the Si sources. These precursor species are transferred by a non-reactive carrier gas from source to the deposition site where they are cracked into their constituents that get absorbed for SiNW growth. The CVD technique has various derivatives which can be classified using parameters which may include the operation pressure or the type of precursor.

Most commonly, CVD can be referred to as Thermal CVD (TCVD) since the various types of sources are thermally activated hence TCVD can be classified according to its operating temperature. These categories can be divided into; high temperature, moderate temperature and low temperature TCVD. In high temperature CVD, a quartz tube is used as the reactor chamber surrounded by heating elements on the outside. In this system, the substrate is placed at the middle of the hot zone of the tube while one end of the tube is connected to the Si precursor or carrier gas, while the other end is connected to an appropriate gas evacuation system. The operation temperature for such a system ranges from 700 – 1100 °C and is commonly used for SiCl<sub>4</sub> source which requires high temperatures for cracking. Furthermore, the choice of operation temperature is also influenced by the choice of metal catalyst used and its eutectic temperature. For example, Ni and Fe require temperatures of about 1000 °C to form eutectic alloys with a Si substrate for VLS growth to occur. Figure 1.8

shows a schematic representation of a CVD growth process using  $\text{SiH}_4$  as a Si precursor.

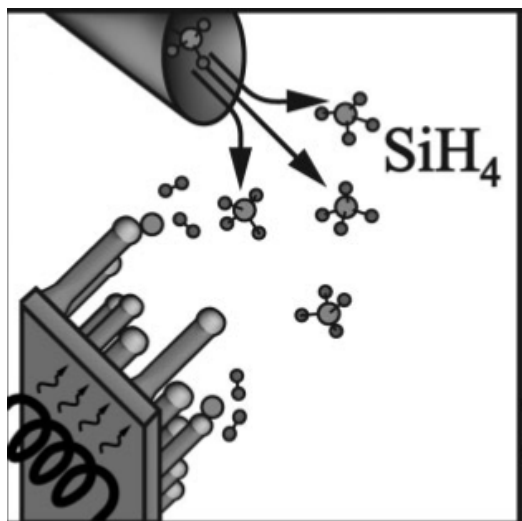


**Figure 1.8:** An experimental setup schematic for the CVD process [1.9].

Typically, the operation temperature for a moderate temperature CVD ranges between 400-700 °C with an internal heater element enclosed within the steel or quartz tube reactor. In this method, only the substrate is heated hence the method is also called the cold wall method. Due to the lower temperature, cracking or decomposition of the Si vapour or gaseous precursor takes place nearer to the surface of the substrate. Owing to the low decomposition temperature (~400 °C),  $\text{SiH}_4$  is the common choice of precursor for the moderate and low temperature CVD. However, to achieve effective decomposition of  $\text{SiH}_4$ , a higher temperature of about 600 °C is necessary. During decomposition,  $\text{SiH}_4$  (silane) is cracked into silylene ( $\text{SiH}_2$ ) which has a lower activation energy and suitable for absorption during VLS growth. This process can be summarised as:



The dominance of the thermal CVD technique is highly influenced by the wide operation temperature range resulting in a variety of applicable catalysts and the ability to epitaxially grow SiNWs at growth velocities of about  $10^{-2}$  to  $10^{+3}$  nm/min.

Several metal catalysts can be used in this technique include Au, Ag, Al, Cu, Ni, Fe, Ti, Pd, etc [1.9]. Furthermore, as a bottom-up synthesis method, small diameter NWs ranging from a few nanometres to several hundred nanometres can be synthesized and their length can be tuned with growth time. Several properties of the grown NWs can be altered in CVD growth through doping which can be easily achieved by introducing several precursors into the reaction chamber.

### **1.5.2 Plasma Enhanced Chemical Vapour Deposition (PECVD)**

In a PECVD system, the reactors can be classified according to the type of plasma source used to produce a gas discharge of the Si precursor. PECVD reactors can either be direct current (DC) or radio frequency (rf) reactor. Structurally, a reactor consists of two parallel plate electrodes separated by a few centimetres such that the top electrode is connected to a rf generator while the lower electrode also used for mounting substrate is grounded. The showerhead design of the system is such that the precursor or carrier gases can be directed into the generated plasma from the top to the bottom electrode as shown in figure 1.9.

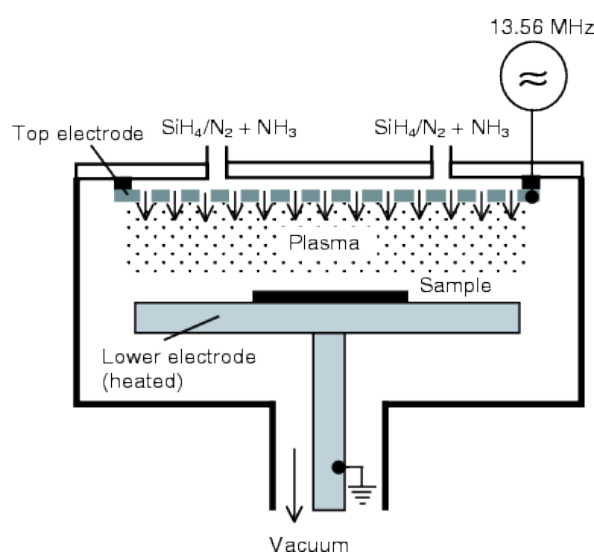


**Figure 1.9:** A schematic diagram showing a RF-PECVD reactor [1.47].

To produce silane plasma which can form a sheath between the two electrodes, a rf of at least 13.56 MHz is required and this creates a potential difference between the sheath regions and the electrodes. This produced plasma is made up of electrons, positively charged  $\text{SiH}_x$  and H ions and some neutral  $\text{SiH}_4$  molecules. As a result of the balanced positive and negative ionic species, the plasma remains electrically neutral.

Within the plasma, the electrons are accelerated which leaves a low electron density in the sheath. In a plasma, the typical electron densities range from about  $10^8 - 10^9 \text{ cm}^{-3}$  for pressures ranging from  $\sim 0.1$  to  $100 \text{ mbar}$  [1.47] while their kinetic energies are in the order of about  $10^1$  electron volts (eV). For the positively charged ionic species, kinetic energies range between 50-100 MeV.

When the neutral  $\text{SiH}_4$  precursor gas molecules are injected into the plasma, dissociation can occur leading to the formation of  $\text{SiH}_3$ ,  $\text{SiH}_2$ ,  $\text{SiH}$ ,  $\text{Si}$  and  $\text{H}$  while the carrier gas  $\text{H}_2$  dissociates to form atomic hydrogen depending on the chemical structure of excited states [1.48]. Perin *et al.*, in his work observed that, due to the high level of interactions involved, the off-spring species can still further react with the parent molecules ( $\text{SiH}_4$  and  $\text{H}_2$ ) since the short lifetime compounds like  $\text{SiH}_2$  and  $\text{SiH}$  and  $\text{Si}$  are highly reactive [1.49]. The long life time and dominant derivatives of silane such as  $\text{SiH}_3$  are less prone to interact and react with the parent species. Due to the dominance of  $\text{SiH}_3$  with a density of about  $10^{11} - 10^{13} \text{ cm}^{-3}$ , the  $\text{SiH}_3$  species is therefore the main precursor responsible for SiNW growth. The other higher order species of silane are most likely to form even bigger molecules making them unsuitable for NW growth.

In comparison, Hofmann *et al.* [1.49] achieved a higher growth rate of gold-catalyzed SiNWs when using PECVD by  $\sim 1$  order of magnitude compared to using thermal

CVD even though PECVD growth starts at lower temperatures. The low temperature dissociation of  $\text{SiH}_4$  in PECVD produces abundant  $\text{SiH}_x$  precursor species, allowing the use of low Si solubility catalyst such as Sn, In and Ga possible. The low melting points of these low solubility catalyst has attracted huge interests in recent studies hence SiNW growth has been achieved as low as 240 °C using In and Sn catalyst [1.50]. In PECVD, random growth of SiNWS is dominant rather than the epitaxial growth observed in CVD and this can be attributed to the random plasma process. Furthermore, PECVD grown SiNWs have been found to exhibit tapered structures implying dominant radial growth. The lack of crystallinity on PECVD grown NWs can be linked to the high energy ions bombardment leading to loss of crystallinity [1.49].

### **1.5.3 Annealing in Reactive Atmosphere**

This growth method was introduced in the early 1960s and used to synthesize Si whiskers. To synthesize SiNWs, a c-Si substrate coated with impurities such as a metal catalyst is exposed to a reactive gas ambient such as hydrogen, iodine, bromine and then heated up to temperatures of about 900 °C [1.9]. Figure 1.10 shows a schematic representation of annealing in a reactive atmosphere.

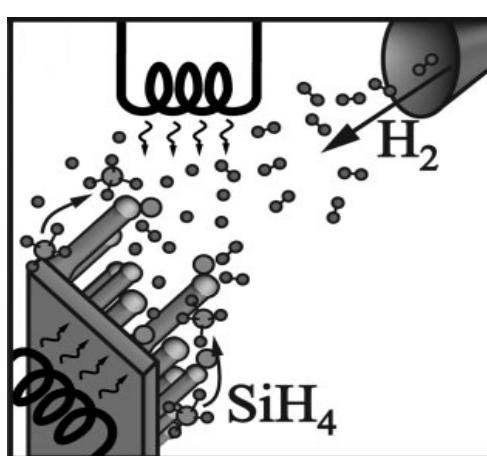


**Figure 1.10:** Shows schematic diagram representing the annealing in reactive atmosphere process [1.9].

These elevated growth temperatures, enable the reactive gases to react with the solid Si to form compounds such as  $\text{SiH}_4$ ,  $\text{SiL}_2$  or  $\text{SiBr}_2$ . These compounds react and get absorbed by the metal catalyst droplet leading to growth of structures similarly to normal CVD.

One of the advantages of this growth method is its technical simplicity which explains why it was favourable in the dawn of Si-wire growth. In this modern day technology, this method has been revised and used as the hot-wire CVD method.

#### **1.5.4 Evaporation of Silicon Monoxide ( $\text{SiO}$ )**

The evaporation of  $\text{SiO}$  is one of the cost-effective methods used for the synthesis of large scale SiNWs. To synthesize SiNWs,  $\text{SiO}$  granules or powders are evaporated in a two-zone tube furnace that is connected to an inert carrier gas supply. The main feature of this setup, is the temperature gradient that is maintained along the tube which drops from about  $1350\text{ }^{\circ}\text{C}$  to  $900\text{ }^{\circ}\text{C}$ . The  $\text{SiO}$  powder is placed on the hotter zone in order to evaporate and is transported downstream to the colder zone by the inert carrier gas, where by a disproportionate reaction occurs producing Si and  $\text{SiO}_2$  [1.36] as shown in figure 1.11.

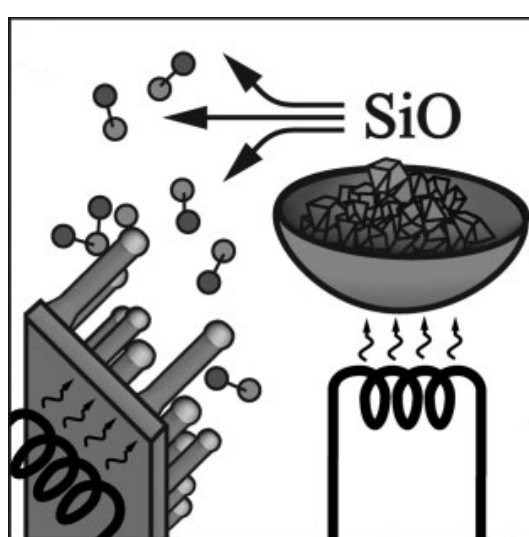


**Figure 1.11:** Schematic showing evaporation of  $\text{SiO}$  growth technique [1.9].

In this method, SiNW growth can be achieved with or without catalyst. However, high growth rates have been observed with metal catalysed growth since it follows the VLS growth mechanism [1.51]. Similarly to conventional CVD, the size of the catalyst determines the diameter of the NW, but the NW and catalyst interactions are more complex than those in normal CVD. During the metal catalyst-free growth, the  $\text{SiO}_2$  is used to catalyze the growth of SiNWs as originally observed in laser ablation growth of NWs [1.52]. This method utilizes the oxide-assisted growth (OAG) mechanism since  $\text{SiO}_2$  containing targets were found to produce a high yield of SiNWs in comparison to pure Si sources [1.53]. Extended growth periods (several hours) have been found to yield crystalline core-shell SiNWs with diameters ranging from 5 to 100 nm and an amorphous outer shell of several nanometres.

### **1.5.5 Molecular Beam Epitaxy (MBE)**

In this method, a pure Si solid source is heated until it starts to evaporate and then the generated beam of gaseous Si atoms is directed onto a substrate where they get adsorbed and crystalize as shown in figure 1.12.

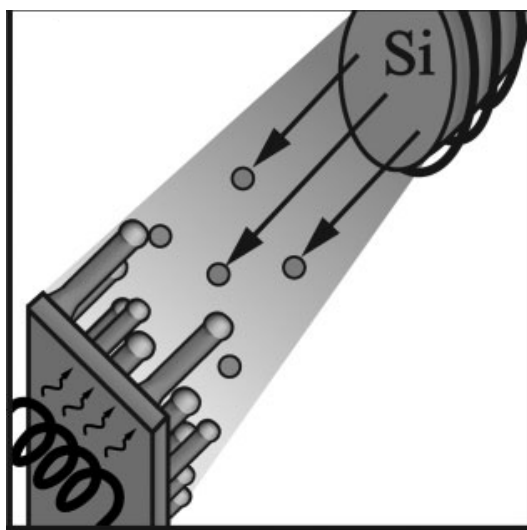


**Figure 1.12:** schematic representation of MBE growth of SiNWs [1.9].

---

This process occurs in ultra-high vacuum conditions which reduces the chances of contamination and permits the use of sensitive surface characterization methods to monitor the growth process [1.54].

The similarity between MBE and CVD is that, they had both been designed for epitaxial layer by layer deposition but suffered metal contamination and yielded NW growth. On the contrary, MBE does not involve the cracking of precursor gases for absorption by the liquid metal-Si alloy droplet hence the liquid droplet does not catalyse growth anymore in this method. During MBE growth, there are two fluxes that govern the growth of SiNWs and they are; the direct Si flux from Si source and the Si flux due diffusing atoms from the Si substrate. Due to the ability to control the incoming flux, it is therefore possible to grow doped NWs or heterostructures in a MBE system by simply alternating between the different desired sources [1.55]. One drawback with this growth method is that, the smallest diameter of the grown NWs limited to about 40 nm [1.53, 1.56] and such an occurrence can be attributed to the Gibbs-Thompson effect which limits MBE to small Si supersaturations. Furthermore, MBE has a low NW growth velocity, about a few nm/min [1.56].

## 1.6 AIMS AND OUTLINE

The aim of this thesis is to optimize a newly installed thermal CVD system for the growth of SiNWs and to characterize the grown structures. Furthermore, the effect of several parameters such as the; metal catalyst, growth temperature and source-to-substrate distance on the growth of the SiNWs will be investigated. This thesis is presented in four comprehensive chapters.

Chapter 1 presents the introduction and literature review on the developments involving SiNWs. The relevance of the study to current energy challenges and its

---

potential intervention is presented as the introduction. The literature review highlights the history and current developments in the field of SiNW research and the various growth techniques.

Chapter 2 of the thesis describes the sample preparation and operation of the TCVD 3-zone furnace procedure. The various analytical techniques and experimental set up used to analyse the various properties of the grown samples is also covered in this chapter. The focus of Chapter 3 is the presentation and discussion of results. This comprehensive chapter presents the different investigations conducted and a summary and conclusion of each study is also presented.

Chapter 4 of this thesis forms the summary of all the work done during the course of the study and also includes recommendations for future work.



---

## 1.7 REFERENCES

- 1.1. N. Gabrielyan, K. Saranti, K. N. Manjunatha, S. Paul, *Nanoscale Res. Lett.* 8(83), (2013).
- 1.2. P. Farzinpour, A. Sundar, K. D. Gilroy, Z. E. Eskin, R. A. Hughes, S. Neretina, *Nanotechnology*. 23 (2012) 495604 (10pp).
- 1.3. S. Iijima, *Nature*. 354(56), (1991) 6348
- 1.4. L. Cui, W. W. Xia, F. Wang, L. J. Yang, Y. J. Hu. *Phys. Rev. B*. 409(2013) 47-50.
- 1.5. S. T. Lee, N. Wang, C.S. Lee, *Mater. Sci. Eng., A*. 286, (2000) 16-23
- 1.6. A. T. Chu, T. T. N. Thi, T. T. Tran, B. N. Vu, T. T. Pham, V. T. Pham, T. H. Pham, H. D. Pham, *Adv. Nat. Sci.: Nanosci. Nanotechnol.* 2, (2011) 035004
- 1.7. R. G. Treuting, S. M. Arnold, *Acta Mater.* 5, (1957) 598.
- 1.8. R. S. Wagner, W. C. Ellis, *Appl. Phys. Lett.* 4, (1964) 89.
- 1.9. 3.11. V. Schmidt, J. V. Wittmann, S. Senz, U. Gosele, *Adv. Mater.* 21 (2009) 2681-2702.
- 1.10. C. S. Kong, MSc Thesis, University of Malaya, Kuala Lumpur (2012).
- 1.11. G. C. Yi, in 'Semiconductor Nanostructures for Optoelectronic Devices', Springer- Verlag publishers, Berlin Heidelberg (2012).
- 1.12. D. D. D. Ma, C. S. Lee, F. C. K. Au, S. Y. Tong, S. T. Lee, *Science.*, 299 (5614), (2003) 1874–1877.
- 1.13. M. M. Adachi, M. P. Anantram, K. S. Karim, *Nano Lett.*, 10, (2010) 4093-4098.
- 1.14. L. T. Canham, *Appl. Phys. Lett.*, 57(10), (1990) 1046.
- 1.15. V. Lehmann, U. Gosele, *Appl. Phys. Lett.*, 58(8), (1991) 856.
- 1.16. Y. S. Sohn, J. Park, G. Yoon, J. Song, S. W. Jee, J. H. Lee, S. Na, T. Kwon, K. Eom, *Nanoscale Res. Lett.*, 5, (2010) 211-216.

- 
- 1.17. R. Rurali, Colloquium, University of Autonoma, Barcelona (2009).
- 1.18. B. Lee, R. E. Rudd, Phys. Rev. B 75(4), (2007) 041305(R).
- 1.19. B. Tian, X. Zheng, T. J. Kempa, Y. Fang, N. Yu, G. Yu, Nature., 449(7164), (2007) 885-889.
- 1.20. N. Tamura, R. Ohshita, M. Fujimoto, M. Kamino, S. Fujitani, J. Electrochem. Soc., 150, (2003) A679.
- 1.21. J. P. Maranchi, A. F. Hepp, P. N. Kumta, Electrochem. Solid-State Lett., 6(9), (2003) A198-A201.
- 1.22. L. F. Cui, R. Ruffo, C. K. Chan, H. Peng, Y. Cui, Nano Lett., 9(1), (2009) 491-495.
- 1.23. A. I. Hochbaum, R. Chen, R. D. Delgado, W. Liang, E. C. Garnett, M. Najarian, Nature, 451(7175), (2008) 163-167.
- 1.24. K. Peng, J. Hu, Y. Yan, Y. Wu, H. Fang, Y. Xu, Adv. Funct. Mater., 16(3), (2006) 387-394.
- 1.25. A. I. Hochbaum, R. Fan, R. He, P. Yang, Nano Letters, 5(3), (2005) 457-460.
- 1.26. G. Cao, in 'Nanostructures & nanomaterials: synthesis, properties & applications', Imperial College Press publishers. (2004)
- 1.27. D. D. D. Ma, C. S. Lee, F. C. K. Au, S. Y. Tong, S. T. Lee, Science, 299(5614), (2003) 1874-1877.
- 1.28. H. Schmidt, M. T. Bjork, J. Knoch, H. Riel, W. Riess, P. Rice, J. Appl. Phys., 103(2), (2008).
- 1.29. S. D. Hutagalung, A. Ahmad, K. A. Yacoob, Solid State Sci. Technol., 16(1), (2008) 100-106.
- 1.30. W. M. Zhou, F. Fang, Z. Y. Hou, L. J. Yan, Y. F. Zhang, IEEE Electron Device Lett., 27, (2006) 463-465.

- 
- 1.31. D. Wang, P. Schaaf, J. Mater. Sci.: Mater. Electron., 22, (2011) 1067-1070.
- 1.32. K. L. Malsiki, A. Polman, Appl. Phys. Lett., 93, (2008) 191113.
- 1.33. H. F. Yan, Y. J. Xing, Q. L. Hang, D. P. Yu, Y. P. Wang, J. Xu, Z. H. Xi, S. Q. Feng, Chem. Phys. Lett., 333, (2000) 224-228.
- 1.34. V. Schmidt, S. Senz, U. Gosele, Nano Letters, 5(5), (2005) 931-935
- 1.35. P. J. Alet, L. Yu, G. Patriache, S. Palacin, I. Roca, P. Cabarrocas, J. Mater. Chem., 18(43), (2008) 5187-5189.
- 1.36. Z. W. Pan, Z. R. Dai, J. Phys. Chem. B, 105, (2001) 2507.
- 1.37. S. Hoffman, R. Sharma, C. T. Wirth, F. Cervantes-Sodi, C. Ducati, T. Kasma, Nat. Mater., 7(5), (2008) 372-375.
- 1.38. B. J. Kim, J. Tersoff, S. Kodambaka, M. C. Reuter, E. A. Stach, F. M. Ross, Appl. Phys. Lett., 322(5904), (2008) 1070-1073.
- 1.39. J. Kikkawa, Y. Ohno, S. Takeda, Appl. Phys. Lett., 86(12), (2005) 123109-123103.
- 1.40. H. J. Choi, J. G. Lee, J. Mater. Sci. 30 (1995) 1982.
- 1.41. E.I. Givargozov, J. Cryst. Growth, 31, (1975) 20.
- 1.42. T.I. Kamins, R.S. Williams, D.P. Basile, T. Hesjedal, J.S. Harris, J. Appl. Phys., 89, (2001) 1008.
- 1.43. K. W. Kolanski, Curr. Opin. Solid State Mater. Sci., 10(3-4), (2006) 182-191.
- 1.44. V. Schmidt, U. Gosele, Science, 316(5825), (2007) 398-399.
- 1.45. L. Cao, B. Garipcan, J. S. Atchison, C. Ni, B. Nabet, J. E. Spanier, Nano Letters, 6(9), (2006) 1852-1857.
- 1.46. L. Yu, F. Fortuns, B. O'Donell, G. Patriache, P. Cabarrocas, Appl. Phys. Lett., 98(12), (2011).
- 1.47. M. Surendra, D. Graves, IEEE Trans. Plasma Sci., 19(2), (1991) 144-157.

- 
- 1.48. A. Matsuda, J. Non-Cryst. Solids, 33-40(1SPEC.ISS), (2004) 1-12.
- 1.49. S. Hoffman, C. Ducati, R. J. Neill, S. Piscanec, A. C. Ferrari, J. Geng, J. Appl. Phys., 94(9), (2003) 6005-60012.
- 1.50. L. Yu, B. O'Donell, P. J. Allet, S. Conessa-Boj, F. Peiro, J. Arbiol, Nanotechnology, 20(22), 2009.
- 1.51. Q. Gu, H. Dang, J. Cao, J. Zhao, S. Fan, Appl. Phys. Lett., 76, (2000) 3020.
- 1.52. N. Wang, Y. H. Tang, Y. F. Zhang, C. S. Lee, I. Bello, S. T. Lee, Chem. Phys. Lett., 299, (1999) 237.
- 1.53. N. Wang, Y. H. Tang, Y. F. Zhang, D. P. Yu, C. S. Lee, I. Bello, S. T. Lee, Chem. Phys. Lett., 283, (1998) 368.
- 1.54. P. Werner, N. D. Zakharov, G. Gerth, L. Schubert, U. Go" sele, Int. J. Mater. Res., 97,(2006) 1008.
- 1.55. N. D. Zakharov, P. Werner, G. Gerth, L. Schubert, L. Sokolov, U. Go" sele, J. Cryst. Growth, 290, (2006) 6.
- 1.56. L. Schubert, P. Werner, N. D. Zakharov, G. Gerth, F. M. Kolb, L. Long, U. Go" sele, T. Y. Tan, Appl. Phys. Lett., 84, (2004) 4968.

---

# CHAPTER 2

---

## 2 EXPERIMENTAL TECHNIQUES

---

### 2.1 INTRODUCTION

This chapter presents the details of method used to prepare samples for the deposition of silicon nanowires (SiNWs) and a detailed description of the growth procedure. Furthermore, a detailed discussion of the various analytical techniques used to characterise the properties of SiNWs is also presented.

### 2.2 SAMPLE PREPARATION

#### 2.2.1 *Substrate preparation*

The substrates used in this work were prepared by cutting a (100) Si wafer into several 1 cm x 1 cm samples which are easy to handle and characterize. These samples were then carefully marked on the backside using a diamond-tip pen in order for them to be distinguishable from each other.

In order to clean the samples, a simple procedure was followed which began by, ultrasonic cleaning of the samples in acetone for 5 minutes followed by another 5 minutes of ultrasonic cleaning in ethanol. Furthermore, these samples were dipped in Isopropanol for another 5 minutes after which they were allowed to air dry before the final cleaning step. The final cleaning step involved dipping the samples in 5% Hydrofluoric acid (HF) solution for 1 minute and then allowed to air dry hence ready for Au or Ni thin film sputter deposition.

## 2.2.2 Au and Ni thin film sputter deposition

During the vapour-liquid-solid (VLS) growth of silicon nanowires (SiNWs), a metal catalyst such as gold, nickel, or copper is very essential since the main vapour – phase adsorption of Si atoms occurs at the metal catalyst droplet hence becoming the nucleation sites for the SiNWs growth. In this work the gold and nickel catalyst thin films were prepared using sputter deposition.

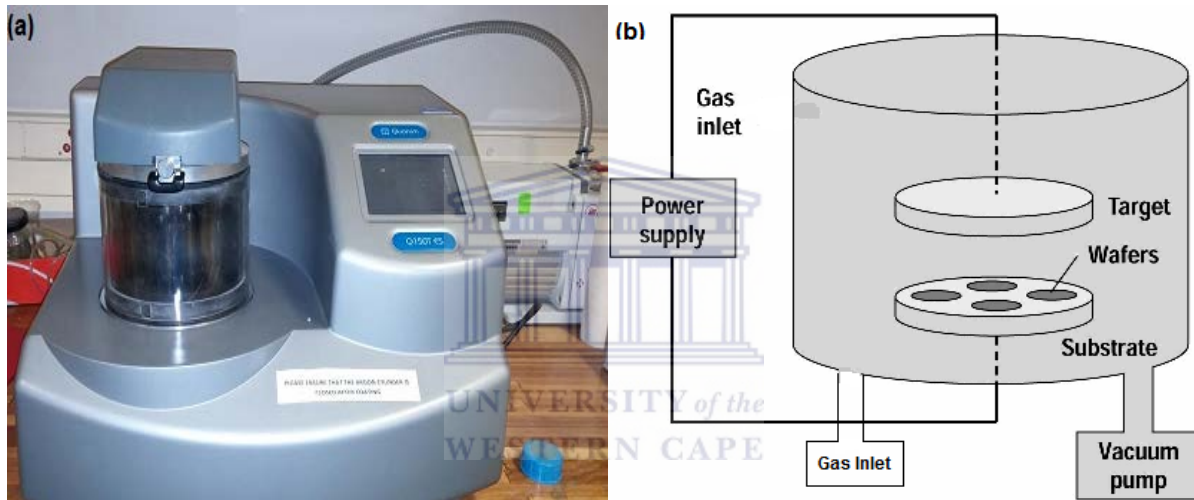


**Figure 2.1:** (a) An image of the Q150TES sputter coater and (b) is a schematic representation of the sputter coater.

Au and Ni thin films of varying thicknesses were deposited on the cleaned Si substrates using a Quorum 150TES sputter coater shown in figure 2.1(a). During sputter deposition, the Film Thickness Monitoring (FTM) profile was used such that whenever the desired film thickness was reached, the sputtering stops automatically. For the Au sputtering, a 99% pure Au target was sputtered with a current of about 20 mA at a pressure of about  $10^{-2}$  mbar for different durations to achieve the various thicknesses. The Ni thin films were also sputtered from a 99% Ni target with current of about 100 mA at a pressure of about  $10^{-2}$  mbar. After the metal thin film depositions, the samples were now ready for Si nanostructure growth.

## **2.2.3 Thermal Chemical Vapour Deposition (TCVD) of Si-Nanostructures**

### **2.2.3.1 The TCVD 3-zone furnace system**

The thermal chemical vapour deposition system used during the growth of the Si-nanostructures was a Brother XD 1600MT 3-zone tube furnace system which is designed and manufactured by Zhengzhou Brother Furnace Co.,LTD.

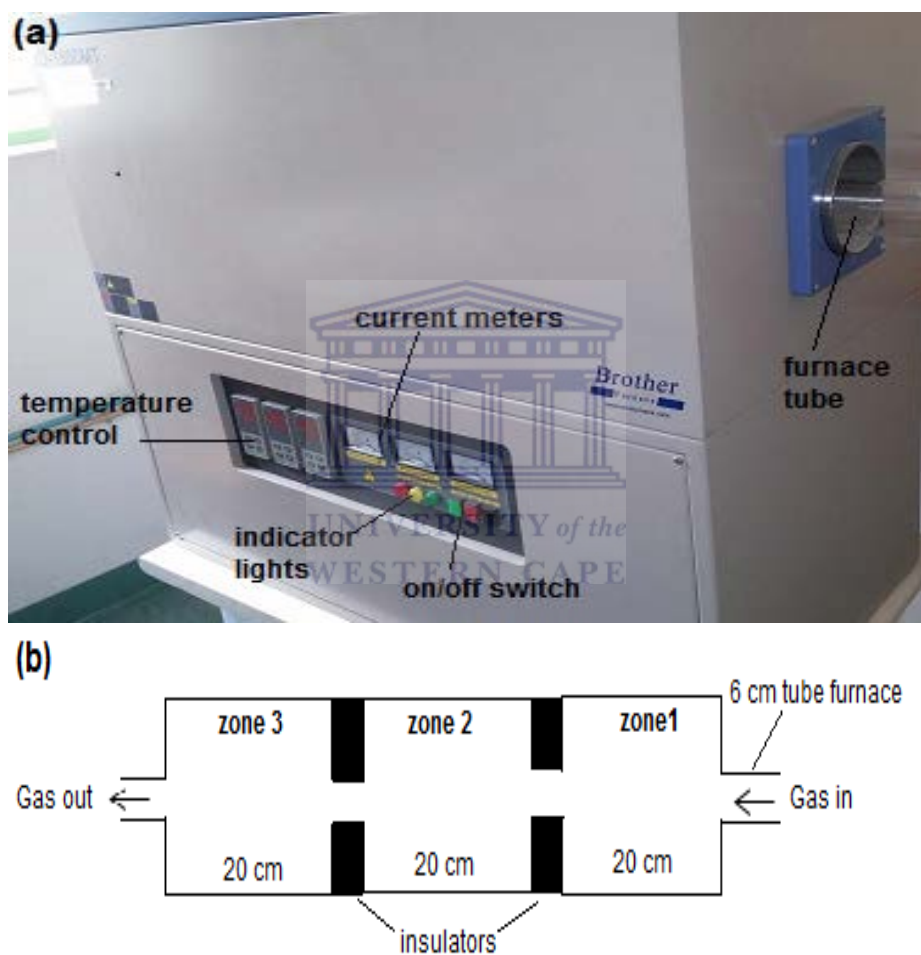


**Figure 2.2:** (a) The photographic image and (b) the schematic diagram of the XD-1600MT.

An image of the Brother XD-1600MT furnace and a schematic diagram is shown in figure 2.2 (a) and (b) respectively. Structurally, the XD-1600MT 3-zone tube furnace is made up of a double layer steel casing that has a three-fan cooling system which maintains the furnace surface at a lower temperature than inside the chamber. This

system has three separate box-shaped heating chambers that are 20 x 20 x 20 cm each and these chambers are partitioned by a 4 cm thick insulating material as shown in figure 2.2 (b). The temperature inside each heating chamber is monitored using three separate thermocouples mounted through the back of the system as shown in figure 2.3 (a). The current temperature (PV) of each chamber is then displayed alongside the set temperature (SV) for that chamber on the 708P temperature control display system as shown in figure 2.3 (b).



**Figure 2.3:** photographic images of; (a) the thermocouples (b) the temperature control and display. Furthermore, this system has a high quality 120 cm long alumina tube furnace with an outer and inner diameter of about 6 and 5 cm respectively. The gas flow in the system was regulated using a gas-flow meter mounted on the gas intake side. Since the system was operated at atmospheric pressure, vacuum pumping was not

required. For easy operation and mobility, the system was mounted on a wooden top trolley that is 100 x 60 x 60 cm.

The 3-zone XD-1600MT tube furnace is a high precision bench-top furnace which utilises high quality ceramic MoSi<sub>2</sub> rods and high quality resistance wires as heating elements. The maximum achievable operating temperature inside the tube furnace under vacuum or with gas flow is 1600 °C and the temperature profile can be set up by 30 segments and run automatically by the 708P advanced temperature controller. The temperature accuracy of the controller is about ± 1 °C making the system ideal for various materials research to develop new materials. .The technical specifications and operating conditions of the system are summarised in table 2.1 as supplied by the manufacturer.

**Table 2.1:** Technical specifications of the XD-1600MT tube furnace.

Name	Unit	Parameter
Working power	KW	9 KW
Voltage	V	AC 380V, 50 Hz, 3 phase
Max. Temperature	°C	1600 °C
Continuous working temperature	°C	1500 °C
Heating rate	°C	< 10 °C
Temperature accuracy	°C	± 1
Heating element		MoSi <sub>2</sub> heater
Connection of heating element		Series connection
Thermal couples heat capacity inside chamber		B type
Dimension of inside chamber	mm	Dia60x200x200x200 mm
Net weight	Kg	165 kg

---

### **2.2.3.2 Temperature calibration of the system**

During TCVD growth of Si-nanostructures, temperature is a crucial parameter since it can directly affect the rate at which the source powder is vaporized. Furthermore, mapping of the temperature variations inside the tube furnace is necessary in order to improve the accuracy of the study since thermocouples obtain the temperature outside the tube and not directly on the source or substrate. The aim of this mini-investigation was to establish the temperature distribution pattern inside the tube furnace, along the heating chamber. This exercise would assist in identifying the ideal positions for the placement of the source material and the substrates.

In this work, a Brother XD-1600MT, 3 zone furnace was calibrated using a Lascar DTM995B NiCr-NiK thermocouple. All the distances that are recorded were measured with reference to the beginning of the first zone being zero. To calibrate the system, two series A and series B of measurements were conducted. During series A, the furnace zone 1 was ramped to a set temperature, SV of  $1400\text{ }^{\circ}\text{C}$  at a steady rate of  $10\text{ }^{\circ}\text{C}/\text{min}$  and allowed to stabilise at  $1400\text{ }^{\circ}\text{C}$  for an hour before data acquisition commenced. Similarly for series B, a similar procedure was observed with set temperature being  $1200\text{ }^{\circ}\text{C}$ . During data acquisition, the temperature measurements were taken from the colder zones towards the hottest zone at 5 cm intervals in order to maintain the accuracy and sensitivity of the thermocouple. At every data point, the thermocouple was allowed to settle for 3 minutes to stabilise.

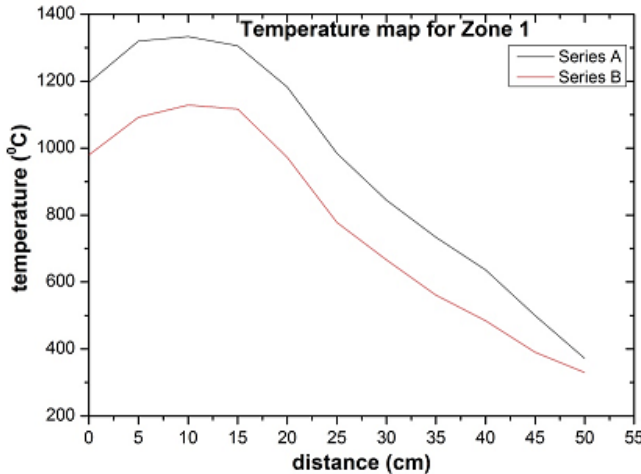


**Figure 2.4:** A temperature map for zone 1 with SV= 1400 °C for series A and 1200 °C for series B

Figure 2.4 shows graphs which represent the temperature distribution inside the tube furnace with only zone 1 illuminated. The 0 and 20 cm distances represent the beginning and the end of zone 1 as per the dimensions of the chamber. As the increases beyond 20 cm, it then represents points outside of zone 1, downstream away from the heated zone.

From the presented results, the maximum obtained temperature for series A was 1333 °C at  $\approx$  10 cm into zone 1 while a similar trend was observed for series B, with a maximum temperature of 1129 °C at  $\approx$  10 cm into zone 1. These results indicate a slight variation of about  $5 \pm 1\%$  between the set and actual temperature inside the tube furnace. This variation or slight drop in temperature can be attributed to the heat conductivity of the alumina tube and the % error of the thermocouple used. In both series, a similar trend is observed where by, a high temperature is observed at the centre of the chamber and gradually drops as you move towards the edges of the heating chamber.

Observations made from this study, indicate that the ideal position to aid in efficient thermal evaporation of the Si source powder is mid-way into the heating chamber. In

---

this case of one zone being heated, the peak temperature at the centre of the zone can be attributed to the close proximity of colder regions as you move away from the centre in either direction. In a scenario conducted by our research group whereby two adjacent zones are heated to the same temperature, the peak temperature is maintained over a broader region spreading over to the area in between the two zones. This observation can also be explained using the same analogy as it was done for the single zone. The use of two heated zones at same temperature was found to be ideal since it maintained stable temperatures over reasonable distances to allow the variation of source-to-substrate distance,  $d_{s-s}$ .

### **2.2.3.3 *The growth of Si-nanostructures in the TCVD system***

The XD-1600MT TCVD furnace used during the growth of Si-nanostructures was powered using a dedicated, AC 380 V, 50 Hz, 3 phase power supply in the laboratory. One end of the tube furnace is then connected to an argon (Ar) gas supply through an Ar gas-flow meter and connecting flanges, while the other end is connected to an exhaust pipe to eject the Ar used as a carrier gas.

As discussed in section 2.1.2, the Ni or Au coated samples (substrates) are placed on a flat horizontal sample holder and then loaded into the alumina tube furnace by opening the flange on the intake side and pushing them into the tube using a calibrated metal rod such that they are 52 cm into the tube. The depth of the metal rod into the tube indicates the position of the samples along the tube relative to the zone dimensions which can be linked to the temperature calibration study of the furnace. A schematic representation of the TCVD set up is shown in figure 2.5.

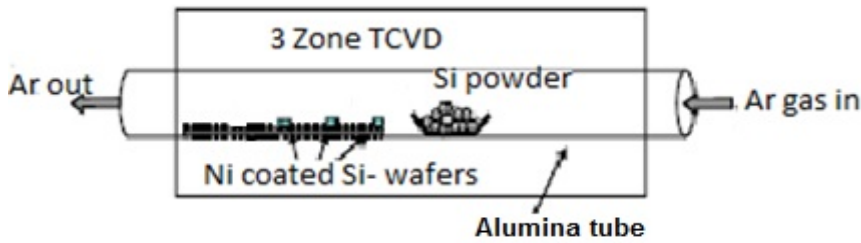


**Figure 2.5:** Schematic representation of the set up in a typical TCVD

A small amount of ~ 20 g of Sigma Aldrich, 325 mesh, 99.99% Si powder (source) was placed in a ceramic boat and placed at a specific position where it was heated to its fixed, vaporization temperature (39 cm into the tube). Based on their geometry, the effective distance between the substrate holder and the source ceramic boat was found to be 11 cm. After loading the samples, the connecting flange is restored and the system is purged with a high flowing Ar gas ( $150 \text{ cm}^3/\text{min}$ ) before heating up the system.

After loading the samples, the system is then switched on from the mains and a temperature profile is created through the 708P temperature control interface shown in figure 2.3 (b). This segmented temperature profile is created within the manufacturer's guidelines in order to protect the system from being damaged. A typical programmed segmented temperature profile is illustrated in figure 2.6.

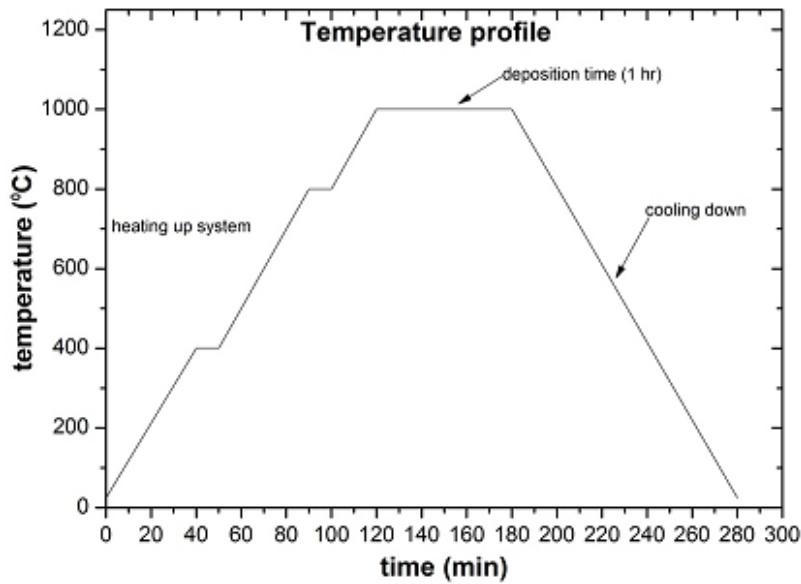


**Figure 4.6:** a segmented temperature profile for growing Si nanostructures at 1000 °C for an hour.

During segmented heating up, the system is heated at a steady rate of 10 °C from room temperature to 400 °C in 40 minutes. At this temperature, the system is allowed to stabilise for 10 minutes after which it ramps up to 800 °C followed by the 1000 °C deposition temperature. At 1000 °C, the system is programmed to remain at this temperature for the entire deposition time (1 hr) after which it automatically starts cooling down until room temperature hence stopping the deposition. During this automatic heating up and cooling, the Ar gas flow in the system is maintained at the 150 cm<sup>3</sup>/min. After cooling down to room temperature, the samples are removed from the system and prepared for characterization.

---

## 2.3 CHARACTERIZATION TECHNIQUES

### 2.3.1 Scanning Electron Microscopy (SEM)

#### 2.3.1.1 Introduction

A modern scanning electron microscope can be utilized in various diverse fields of study which can range from biomedical sciences to the semiconductor industry. The SEM can be utilized to characterize silicon nanostructures in order to obtain information about the morphology, structural properties, topography and the elemental composition of synthesized silicon nanostructures.

Inside the SEM, electrons are thermionically emitted from a cathode or a field-emission gun (FEG), situated at the top of its electron-optical column. These emitted electrons form an electron cloud and this beam of electrons is accelerated by high voltages towards a specimen containing anode. As the beam of electrons is accelerated down the SEM column, a series of electromagnetic lenses coils and apertures are used to focus the electron beam (e-beam) into a fine probe that systematically scans over the specimen surface, to produce an image.

From the SEM schematic shown in figure 2.7, the two condenser lenses, situated below the electron gun are used to focus the emerging beam into a smaller diameter size, which is then further aligned and focused by apertures and coils within the column until it reaches the objective lens (final lens aperture) near the specimen chamber. The objective lens then further demagnifies the beam into a small spot of about 0.1-1  $\mu\text{m}$  in diameter and moves it up and down in space until it reaches the specimen surface. Furthermore, the objective lens also determines the intensity of the incident e-beam on the specimen and hence controls the image brightness.

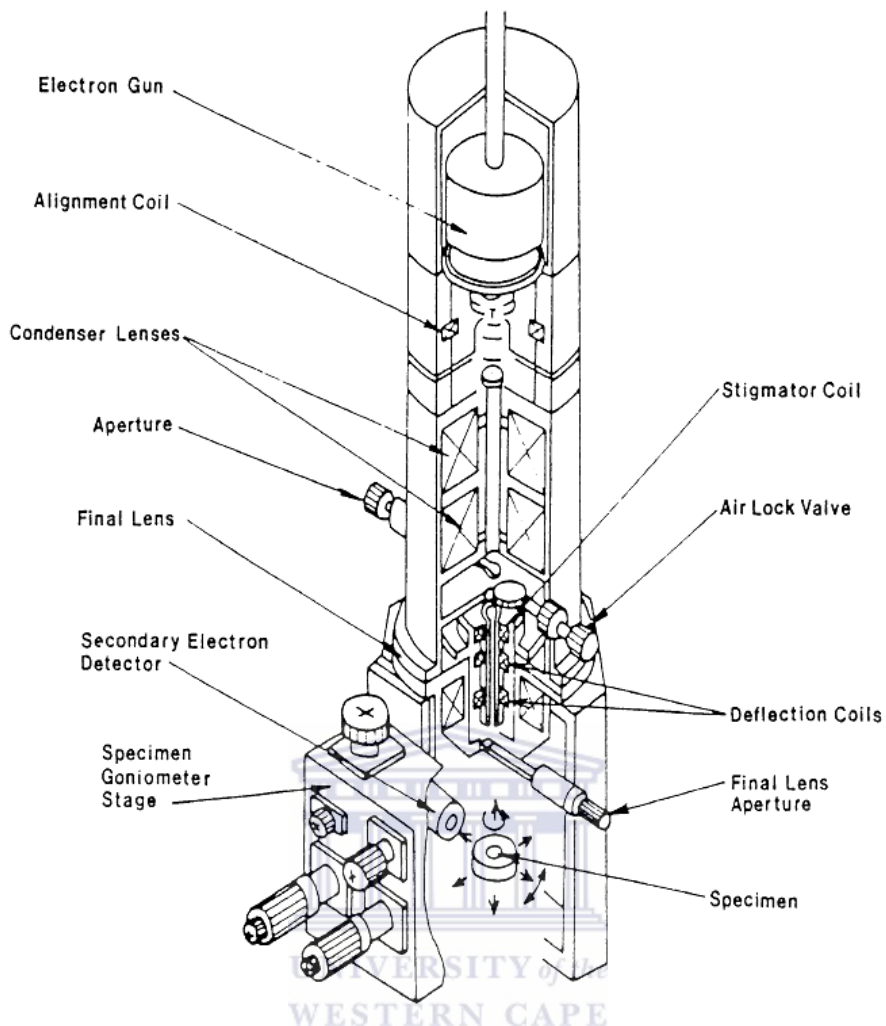


**Figure 2.7:** Schematic representation of a SEM. [2.1]

### 2.3.1.2 Resolution

The resolution of an SEM can be understood as the smallest distance at which two objects can be viewed or resolved as separate entities [2.2]. During the microscopy of nanostructures, the resolution of the apparatus can be regarded as the most crucial factor and even beyond magnification. In SEM, achieving huge magnifications at the expense of resolution is undesirable, since critical information and features cannot be revealed by the image obtained. Theoretically, the smallest separation distance  $d$ , at which two objects can be resolved and referred to as the limit of

resolution can be defined using Abbe's equation (2.1). This equation shows that there are several factors which can affect the resolution of the SEM

$$d = \frac{0.612\lambda}{nsin\alpha} \quad (2.1)$$

Where by  $d$  = limit of resolution

$\lambda$  = wavelength of the energy source

$n$  = refractive index of the medium of propagation for the light

$\alpha$  = aperture angle.

### 2.3.1.3 Working distance, depth of field and resolution

The depth of field (DOF) can be referred to as the range of positions at which an image appears in focus. The DOF can be altered by adjusting the working distance (WD), which can be defined as the distance between the final condenser lens and the surface of the specimen as shown in figure 2.8.

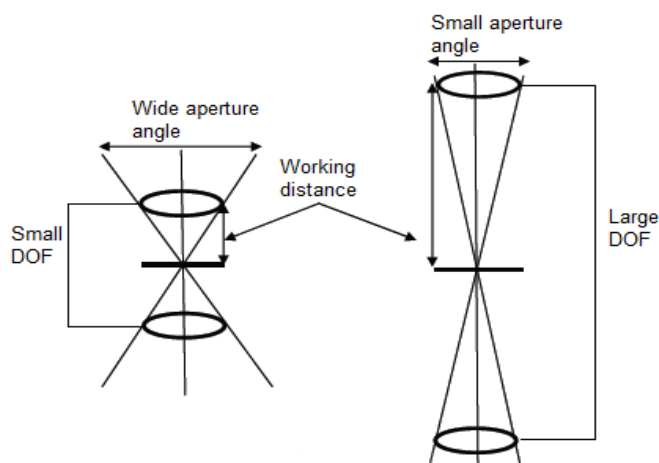


**Figure 5.8:** Schematic presentation of the WD influence on DOF and resolution [2.1].

As the WD is increased, the aperture size is decreased further resulting in an increased DOF with lower resolution. Similarly, when the WD is decreased, the

aperture size is increased resulting in a shallow DOF as it is schematically illustrated in figure 2.8.

Altering the WD of a SEM also has a direct impact on the spherical aberration of the imaging system and that consequently affects the resolution of the final image. Spherical aberration is a result of the geometrical effects of the electromagnetic lenses. This phenomenon is observed when electrons closer to the beam axis are refracted less than the electrons passing along the periphery of the electron beam, hence resulting in multiple focal points which in-turn result in an enlarged, non-focused spot as illustrated in figure 2.9 [2.1]. When the WD decreases, the spherical aberration effects are reduced, resulting in a smaller focused beam spot which consequently yields a higher resolved image.

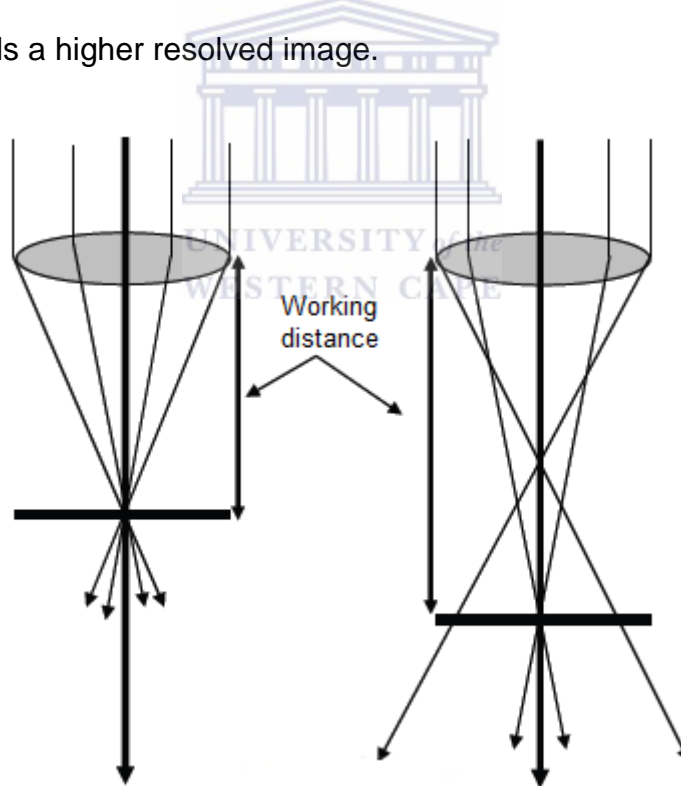


**Figure 2.9:** Effects of working distance on spherical aberration and resolution of image [2.1].

### **2.3.1.4 Electron beam – specimen interaction signals**

When an incident primary beam of electrons interacts with a specimen sample, several signals are generated within the sample and get detected within the SEM. These generated signals contain valuable information about the morphology and composition of the sample being investigated. A schematic diagram shown in figure 2.10 presents the types of signals generated during electron beam – sample interaction [2.3]. Signals such as the secondary, backscattered and transmitted electrons provide information about the surface morphology of the sample while characteristic x-rays, cathodoluminescence and Auger electron signals contain information about the chemical composition of the sample.

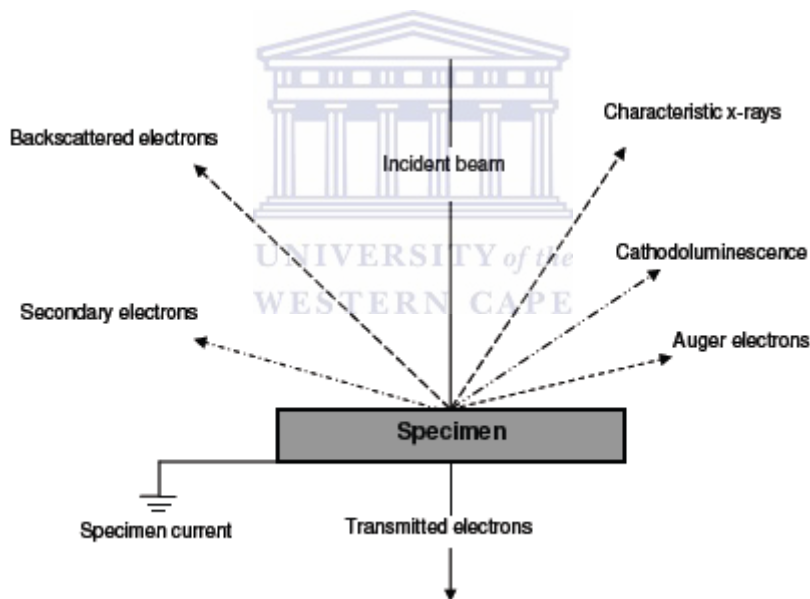


**Figure 2.10:** Schematic illustration of the signals generated during electron beam – sample interaction [2.3].

#### **2.3.1.4.1 Secondary electrons and image formation in the SEM**

During electron beam – specimen interaction, an interaction volume is created in which the electrons get scattered as it is shown in figure 2.11. As a consequence of these scattering events, secondary products like secondary electrons, backscattered electrons, x-rays, heat and light are produced. The low – energy secondary electrons

are responsible for the image formation since they are generated very close to the sample surface ( $\approx 10$  nm). Those secondary electrons generated deep in the interaction volume get re-absorbed by the sample and are not detected hence the secondary electrons provide the surface profile of the sample.

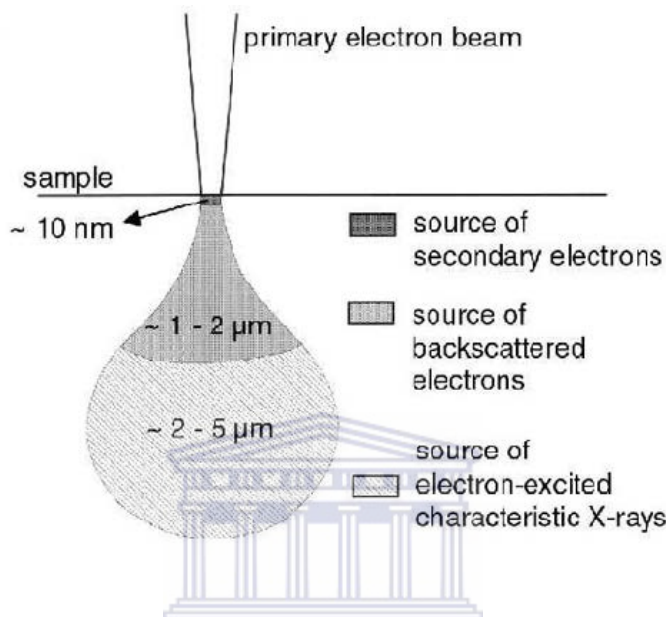


**Figure 2.11:** Schematic illustration showing the relative origin of secondary and backscattered electrons and characteristic x-rays within the interaction volume [2.3].

#### 2.3.1.4.2 Characteristic x-rays and Energy dispersive spectroscopy (EDS)

Based on the schematic illustration of an atom shown in figure 2.12, it can be observed that the nucleus of an atom is surrounded by circular energy levels that can be referred to as ‘shells’. These shells are denoted by K, L, M,... which corresponds to the principle quantum number,  $n = 1, 2, 3$ . During electron beam – sample interaction, an inner electron from the K- shell may be dislodged leaving the atom in an excited state. For the atom to return to its normal ground state, the vacancy created in the K shell needs to be filled by an electron from the outer shells (L or M). When this recombination occurs, the outer electron undergoes a discrete energy transition and the energy difference between the two energy states is

discrete and characteristic of that particular atom. This surplus energy is then emitted as x-rays.

When the vacancy created in the K shell is filled by an electron from the neighbouring L shell, the emitted x-ray is referred to as the  $K_{\alpha}$  x-ray, while if the vacancy is filled by an M shell electron,  $K_{\beta}$  x-rays are emitted. A similar nomenclature is adopted when an L shell electron is knocked off and the vacancy is filled by a M shell electron. The  $\alpha$  and  $\beta$  subscripts represent first and second nearest neighbour shell respectively.

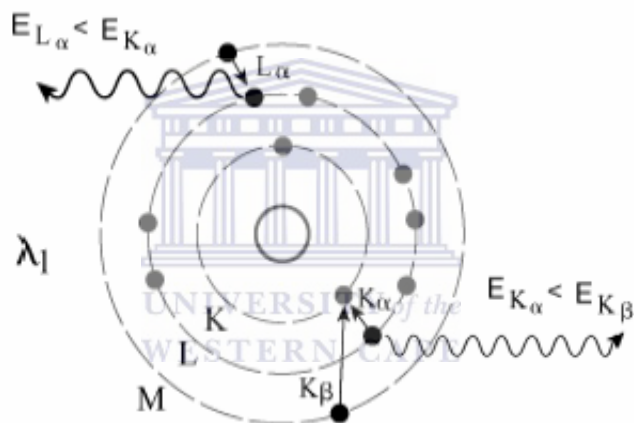


**Figure 2.12:** characteristic x-rays emitted by an atom [2.4].

Figure 2.12 clearly illustrates the basic origin of energy dispersive spectroscopy (EDS). The EDS technique involves the separation of the different characteristic according to their energies using a semiconductor detector. Inside the detector, the electrons of the semiconductor crystal are excited by absorbing energy from an incident x-ray. The amount of excited electrons is directly proportional to the energy of the incident x-ray and the absorbed energy is then transformed into an electronic signal which is emitted and amplified. The electronic signal is further converted into a digital form and transferred to a multi-channel analyser (MCA). In the MCA, the

---

energy signals are then sorted into different channels and the information is then presented as an energy spectrum.

### **2.3.1.5 Sample preparation for SEM characterization**

When imaging a non-conductive specimen with the SEM, it is necessary to coat the specimen with an electrically conductive coating. The main aim of this coating is to increase the sample's electrical conductivity, reduce the thermal damage caused by the beam to the sample, increase secondary and backscattered electron emission and further improve the sample's mechanical stability.

During electron beam and non-conductive specimen interaction, unwanted charge build up occurs since the sample cannot conduct the charge away from it during bombardment. This charge build up may result in the deflection of the incident electron beam and some secondary electrons hence degrading the quality of the final image of the sample. It is therefore necessary to sputter coat the specimen with a conductive material (carbon, gold or silver) to ensure that charge can be dissipated away from the sample. Furthermore, this conductive coating of the sample also helps in preventing excessive heat build - up which can damage the sample.

A high resolution Auriga FESEM, operating at about 5.0 kV and equipped with an electron dispersion spectroscope, was used to obtain SEM micrographs and also conduct EDS analysis of the grown samples.

---

## **2.3.2 X-Ray Diffraction (XRD)**

### **2.3.2.1 Introduction**

X-ray diffraction (XRD) is a technique commonly used for the characterization of the crystal structure of a material. The crystal of an element can be identified by determining the peak position in a XRD pattern, while the orientation plane corresponding to the peak can be assigned. XRD provides a qualitative determination of the crystallinity of a material by analysing the intensity of the diffraction peak. The crystallite size of the material can also be quantitatively calculated from the width of the diffraction peak using several methods [2.5].

During XRD, the analysed x-rays are electromagnetic radiation of smaller wavelength than light and are produced when a fast moving electron is rapidly slowed down. Diffraction is a phenomenon that occurs when waves interfere with a structure whose repeat distance is about the same as that of the incident wavelength. During these interactions, constructive and destructive interference patterns are formed as a result of the scattering of the incoming wave fronts by the structure of the material. The wavelength range of x-rays is about the same as that of the interatomic spacing found in three-dimensional crystalline structures, meaning that x-rays can be diffracted by these crystalline structures with each atom in the crystalline structure serving as scattering centres for the incoming wave fronts. Since XRD is only sensitive to crystalline structures, it can therefore be applied for both homogeneous and inhomogeneous samples, which is suitable for the structural characterization of nanomaterials such as SiNWs.

### 2.3.2.2 Theory of x-ray diffraction

The arrangement of atoms in materials can be either random, making the material amorphous or be arranged in a three dimensional periodic pattern resulting in a crystalline material. The atomic arrangement in a crystal can be visualised in a way that the atoms are a set of imaginary points with a fixed relation in space as illustrated in figure 2.14 [2.2] whereby the above concept is referred to as a point lattice and is defined as an array of points in space, so arranged that each point have identical surroundings.

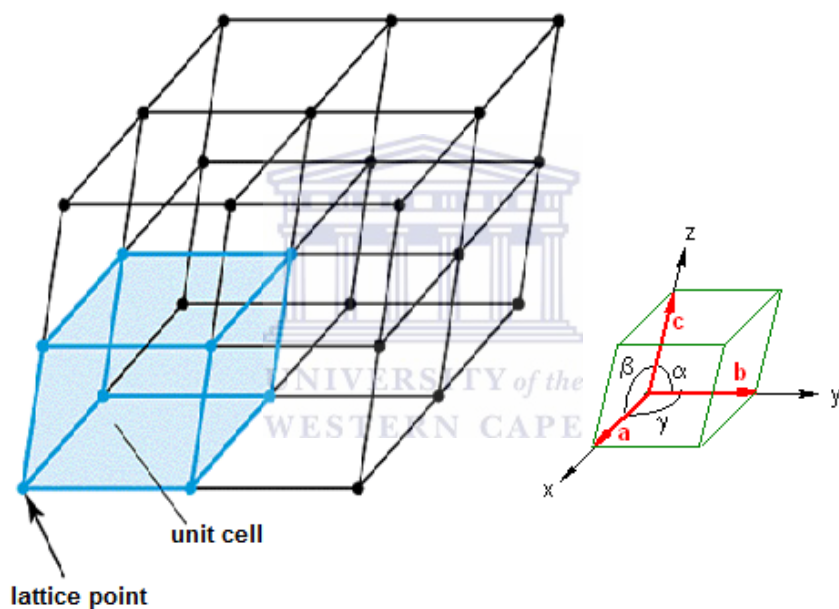


**Figure 2.14:** a schematic of a point lattice and its unit cell [2.2]

When three vectors  $\vec{a}$ ,  $\vec{b}$ ,  $\vec{c}$  are drawn from the corner of any lattice point, a point lattice unit cell is formed. These vectors are known as the crystallographic axes of the unit cell and can also be described in terms of the lattice parameters such as the lengths ( $a$ ,  $b$  and  $c$ ) and the angles between them ( $\alpha$ ,  $\beta$  and  $\gamma$ ) as shown in figure 2.14. Furthermore, these crystallographic axes define the whole point lattice which can be generated by the repeated action of these vectors. Based on the relationship

between the lattice parameters ( $a$ ,  $b$ ,  $c$ ,  $\alpha$ ,  $\beta$  and  $\gamma$ ), there are fourteen different types of point or Bravais lattices as shown in table 2.2 [2.6].

In a Bravais lattice, the direction of any vector can be defined used a linear combination of the three crystallographic axes as:

$$\vec{x} = u\vec{a} + v\vec{b} + w\vec{c} \quad (2.1)$$

Where by  $\vec{a}, \vec{b}, \vec{c}$  = any vector in the Bravais lattice

$u, v, w$  = coordinates of any point on the vector.

In short form, equation (2.1) can also be written as [  $u, v, w$  ].

**Table 2.2:** A table describing the fourteen different Bravais lattices [2.6].

System	Axis lengths and angles	Bravais lattice	Lattice symbol
Cubic	Three equal axis at right angles $a = b = c, \alpha = \beta = \gamma = 90^\circ$	Simple	P
		Body-centred	I
		Face-centred	F
Tetragonal	Three axis at right angles, two equal $a = b \neq c, \alpha = \beta = \gamma = 90^\circ$	Simple	P
		Body-centred	I
Orthorhombic	Three unequal axis at right angles $a \neq b \neq c, \alpha = \beta = \gamma = 90^\circ$	Simple	P
		Body-centred	I
		Base centred	C
		Face-centred	F
Rhombohedral	Three equal axes, equally inclined $a = b = c, \alpha = \beta = \gamma \neq 90^\circ$	Simple	R
Hexagonal	Two equal co-planar axes at $120^\circ$ , third axes at $90^\circ$ $a = b \neq c, \alpha = \beta = 120^\circ, \gamma = 90^\circ$	Simple	P
Monoclinic	Three unequal axes, one pair not at $90^\circ$	Simple	P

	$a \neq b \neq c$ , $\alpha = \gamma = 90^\circ \neq \beta$	Base centred	C
Triclinic	Three unequal axes, unequally inclined and none at $90^\circ$ $a \neq b \neq c$ , $\alpha \neq \beta \neq \gamma \neq 90^\circ$	Simple	P

### 2.3.2.3 Bragg's law for diffraction

In order to understand the phenomenon of x-ray diffraction in crystals, known as Bragg's diffraction, consider two sets of parallel lattice planes that specularly reflect incident x-rays elastically (i.e. angle of incidence is equal to angle of reflection). When two in-phase x-ray waves are incident at an angle  $\theta$  onto two parallel lattice planes separated by a distance  $d$ , as illustrated in figure 2.15 [2.6], the difference on the distance travelled (path difference) by the two waves reflected from neighbouring planes can be given by;  $CB + BD = 2ds\sin\theta$ . A major requirement for constructive interference to occur from adjacent planes is that, this path difference must be equal to an integral number  $n$  of the wavelength  $\lambda$ . This requirement can be summarised mathematically in equation (2.2) and is known as Bragg's law [2.6].

$$n\lambda = 2ds\sin\theta \quad (2.2)$$

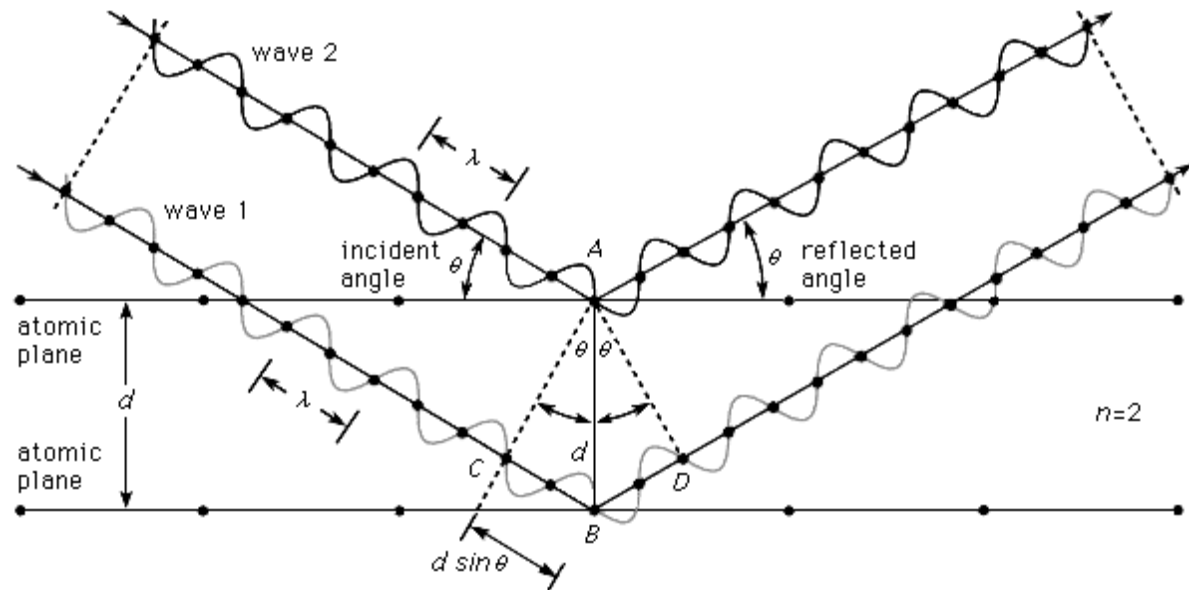
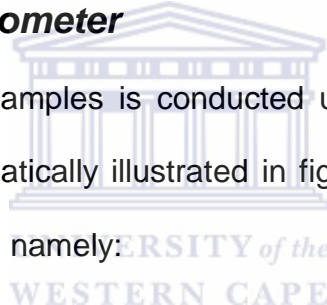


**Figure 2.15:** A schematic illustration of Bragg's law [2.6].

#### 2.3.2.4 The x-ray diffractometer

X-ray diffraction analysis of samples is conducted using a device called an x-ray diffractometer which is schematically illustrated in figure 2.16. This device is made up of three major components, namely:



- The x-ray source (denoted S and T)
- The diffractometer circle and
- The detector system (G and E)

During XRD analysis, the detector (G) is mounted at the circumference of the diffractometer circle which is centred at C, the specimen stage. The specimen is then supported on a horizontal table H, which can rotate about its axis at point O. upon reaching the sample at C, the x-rays generated from the source S, get diffracted by the sample at C resulting in a diffracted convergent beam which focuses at the slit F, before entering the detector at G which is supported by carriage E. This carriage E, is also designed to rotate freely about the axis O and has an angular position  $2\theta$

while the H and E supports are mechanically locked in a  $\theta$ - $2\theta$  relationship. The special slits at A and B are used to define and collimate the incident and diffracted beams respectively. To reduce the amount of background and  $K_\beta$  radiation entering a detector, a filter is placed on the diffracted beam-path.

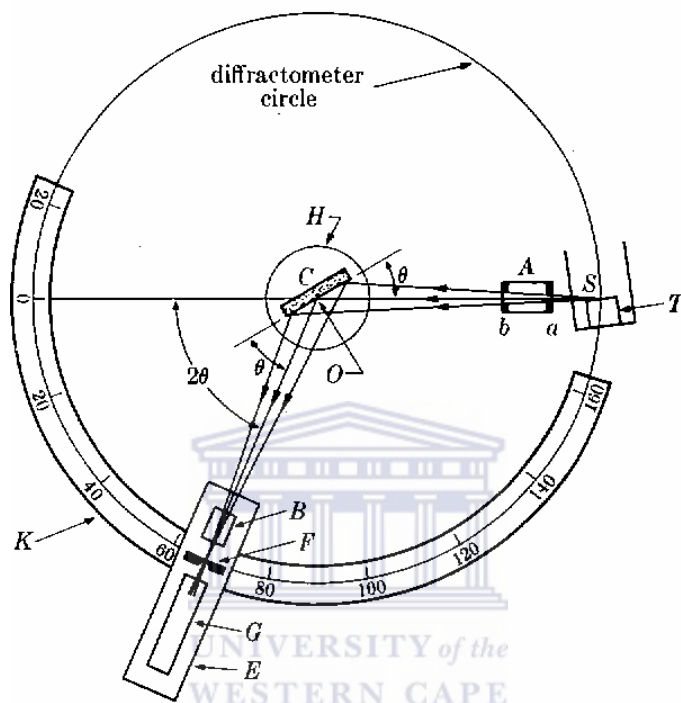


**Figure 2.16:** Schematic illustration of an x-ray diffractometer [2.6].

### 2.3.2.5 XRD characterization

The x-ray diffraction technique can be used to analyse the crystallinity of SiNWs. A typical XRD spectrum of Si is shown in figure 2.17 and the crystalline planes which correspond to the shown diffraction peaks are indexed according to the face-centered cubic Si (JCP2:00-026-1481). In the presented spectrum, the dominant diffraction peak is the (111) orientation and can be deconvoluted for further analysis of the sample.

Qualitative analysis of the crystallinity of SiNWs can be conducted by using the intensity and full width at half maximum (FWHM) of the Si diffraction peak and

compare with that of a bulk Si crystal. The crystallite size,  $D_x$  can also be linked to the FWHM through the Debye-Scherrer's equation [2.7]:

$$D_x = \frac{c\lambda}{\varphi \cos \theta} \quad (2.3)$$

Where  $\lambda$  is the wavelength of the CuK (1.5418 Å),  $\varphi$  is the FWHM of the peak and  $\theta$  is the angle of the diffraction peak and C is the Scherrer constant (0.89).

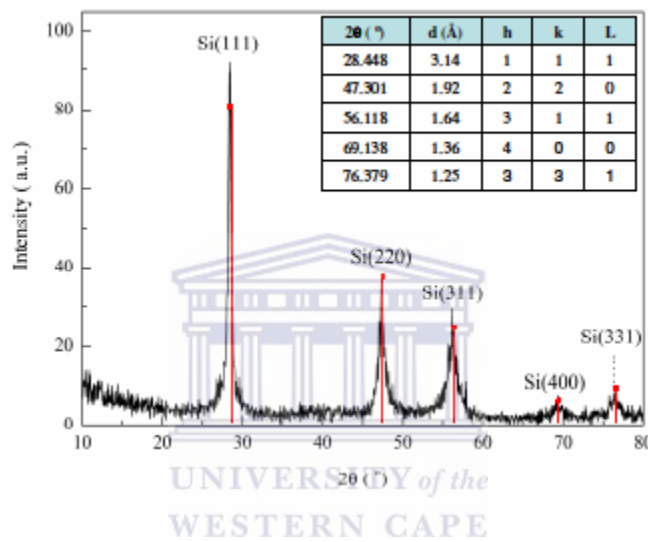


**Figure 2.17:** Typical XRD spectrum of crystalline SiNWs [2.8].

In this thesis, Panalytical X`pert PRO PW3040/60 X-ray diffractometer, was used for X-ray diffraction (XRD) analysis, ranging from 0 – 90° ( $2\theta$ ) in order to ascertain crystallinity and phase identification in the grown SiNWs.

### 2.3.3 Fourier Transform Infrared Spectroscopy

#### 2.3.3.1 Introduction

Fourier transform infrared spectroscopy (FTIR) is a quick, non-destructive and effective characterization technique used to study the different vibrational modes in samples. In FTIR spectroscopy, the various types of bonds present in a sample are identified using the different vibrational frequencies, since each functional group absorbs a specific characteristic frequency.

An infrared absorption spectrum therefore can provide qualitative information about the amount of oxygen or hydrogen content and the bonding configuration in a semiconducting material such as silicon. Furthermore the intensity of the absorption bands in FTIR spectrum can be linked to the prevalence of that particular bonding configuration (species) in that material being analysed. In oxidised-SiNWs, it is necessary to employ infrared red spectroscopy and identify the various Si-O vibrational modes present in the sample [2.9].

### 2.3.3.2 The theory of FTIR

The basis of the infrared (IR) spectroscopy involves the determination of the amount of absorption of the different IR frequencies when an IR beam is incident on a sample. The resultant spectrum from a sample represents the absorption and transmission characteristics forming a spectral fingerprint, since every structure has a unique infrared spectrum. The core of fourier transform infrared spectrometry is based on a Michelson interferometer which is schematically illustrated in figure 2.18.

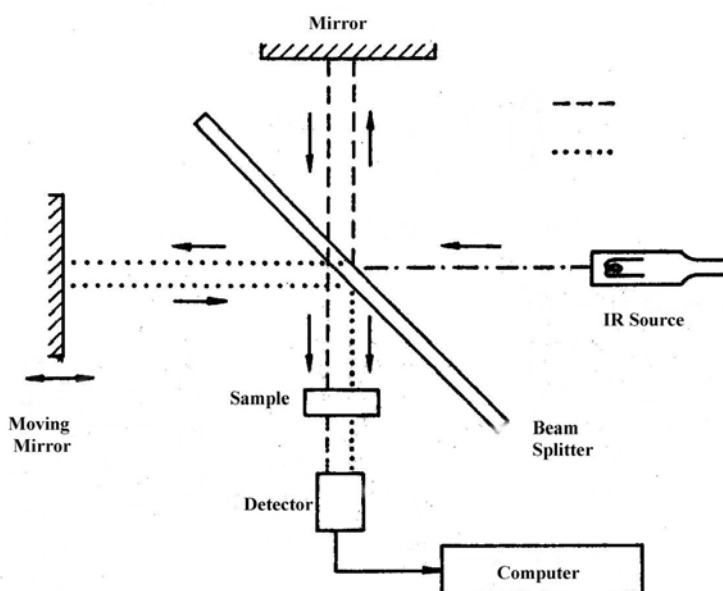
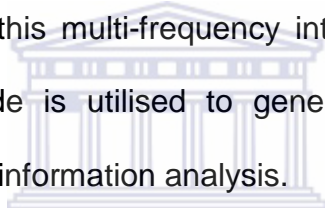


**Figure 2.19:** A Michelson interferometer in a FTIR spectrometer [2.10].

---

The Michelson interferometer shown in figure 2.19 is made up of a beam-splitter, a fixed mirror and a moving mirror. The main function of the beam splitter is to split the incoming IR beam from the source into two identical optical beams. One of these beams is then reflected off from a fixed flat mirror while the other beam also reflects off from a moving mirror which is designed back and forth near the beam splitter. As these two beams reflect off their respective mirror, they again recombine at the beam splitter. As a consequence of the moving mirror, the two beams have a path length difference when they recombine at the beam splitter forming an interference signal. This resultant signal is referred to as an interferogram and is such that, every point making up the signal, contains information about the infrared frequencies coming from the source. To decode this multi-frequency interferogram signal, the Fourier Transformation computer code is utilised to generate a spectrum of individual frequencies that are useful for information analysis.



### ***2.3.3.3 The vibrational modes***

Due to the Feglet advantage (quick), FTIR spectroscopy is one of the most commonly used and effective technique for analysing the Si–O vibrational modes in oxidised SiNWs grown on Si substrates. In oxidised SiNWs, several Si–O bonding configurations and vibrational modes exist, hence the need to identify, quantify and interpret each existing Si–O vibrational mode.

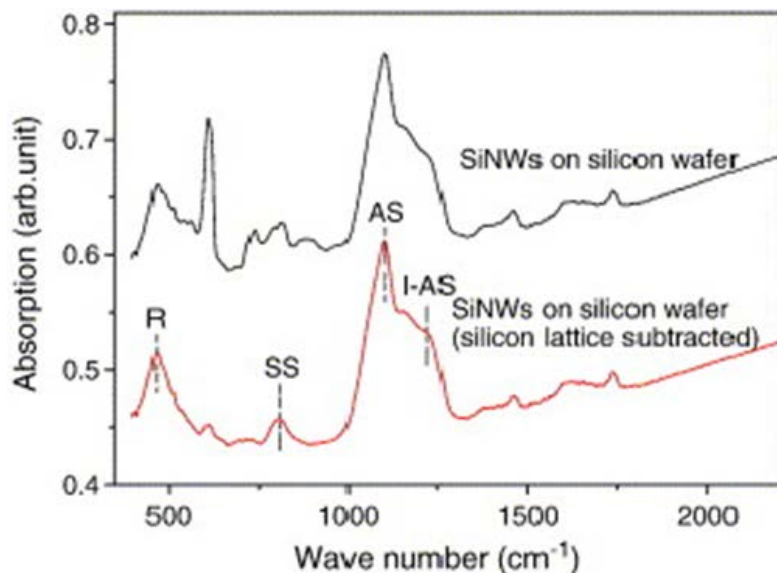


**Figure 2.20:** Typical TO absorption bands of SiNWs [2.11].

A Typical FTIR spectrum of oxidised SiNWs is presented in figure 2.20. This spectrum shows the three major transverse optical (TO) absorption bands of SiNWs within the  $400 - 1500\text{ cm}^{-1}$  range which can be classified according to the specific vibrational modes of the oxygen (O) atoms and silicon (Si) atoms which they bridge. The lowest frequency TO band centred at around  $460\text{ cm}^{-1}$  is characterized by the Si-O-Si rocking vibrational mode while the middle frequency TO band centred around  $808\text{ cm}^{-1}$  is due to the O-Si-O symmetric stretching (SS) mode [2.12]. The high frequency TO band ranging from about  $1000-1300\text{ cm}^{-1}$  and centred around  $1085\text{ cm}^{-1}$  can be attributed to the Si-O-Si asymmetric stretching (AS) mode and forms the strongest and widest absorption peak. This wider absorption band is composed of two modes; (i) the asymmetric stretching mode where by adjacent O atoms asymmetrically stretch in-phase ( $\text{AS}_1$ ), (ii) the adjacent O atoms asymmetrically stretch  $180^\circ$  out of phase ( $\text{AS}_2$ ) with each other [2.13].

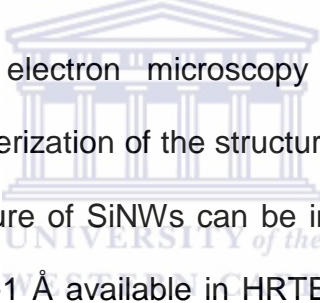
---

### **2.3.3.4 Experimental setup**

Fourier transform infra-red (FTIR) analysis of the samples, was conducted using a Perkin Elmer Spectrum 100, ranging from  $400 - 4000\text{ cm}^{-1}$  in order to establish the chemical composition and bonding configuration of the grown SiNWs. To conduct the experiment, the spectrometer was operated in transmission mode at a resolution of  $4\text{ cm}^{-1}$  and 120 scans. A baseline measurement was conducted using a bare Si (100) wafer to account for the absorption of the crystalline silicon substrate, hence all measurements were corrected.

## **2.3.4 Transmission Electron Microscopy**

### **2.3.4.1 Introduction**



High-resolution transmission electron microscopy (HRTEM) is a fundamental technique used for the characterization of the structural properties and crystallinity of the SiNWs. The atomic structure of SiNWs can be investigated using HRTEM at a high theoretical resolution of  $\sim 1\text{ \AA}$  available in HRTEM due to the shortening in de Broglie wavelength of the high energetic electron beam. The high resolution ability enables the determination of crystalline or amorphous structures and other structural defects such as twinning and lattice dislocations observed in SiNWs. HRTEM can also be used to determine the atomic lattice spacing, crystalline plane and growth orientation of SiNWs.

### **2.3.4.2 Image formation in the TEM**

The main components of a TEM consist of an electron gun, a series of electromagnetic lenses, the viewing screen and a camera. These components are all incorporated inside the vertical column of the microscope.

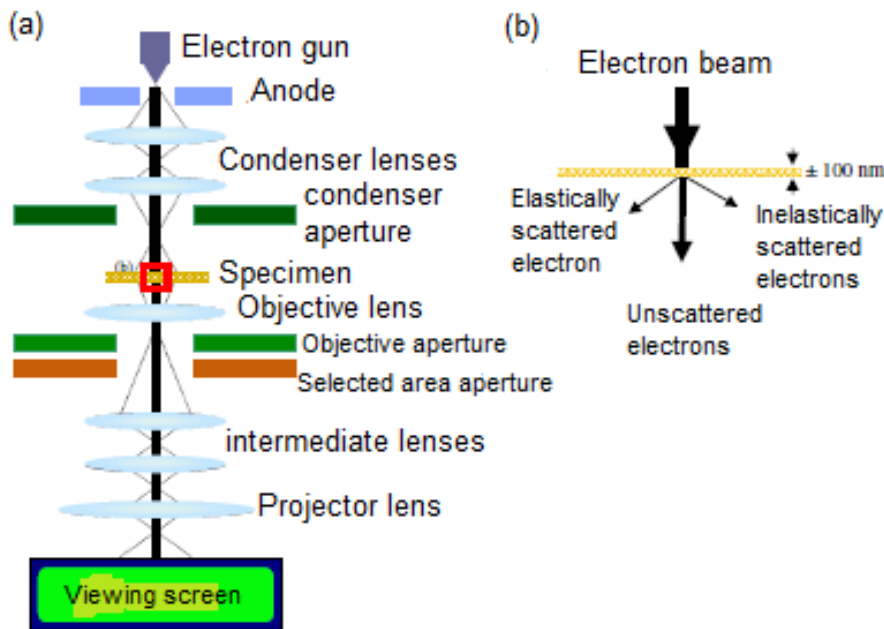


**Figure 2.21:** A schematic diagram showing; (a) the main components of a HRTEM, (b) the generated signals during electron beam – sample interaction [2.8].

A schematic diagram showing the main components of a TEM is presented in figure 2.21. Similar to the SEM discussed previously, the TEM is constructed with a field emission electron gun, which enables the high resolution of the instrument. The high tension (HT) voltage applied to accelerate the electrons is in the range of 100 to 300 kV in order for the transmission of electrons through the specimen to occur.

These produced electrons are then accelerated towards an anode such that a beam of electrons with regulated energy is produced. The gun deflector coils ensure that the electron beam is deflected in such a way that it aligns parallel to the optical axis. The main function of the condenser system in a TEM is to control the amount of illuminated area on the sample and consists of the first and second condenser lenses. The first condenser lens focuses the beam into a relatively small spot therefore effectively controlling the optical spot size to less than  $1\mu\text{m}$ . The second condenser lens is then used to control the angle of convergence, of the electron beam, and the area of the specimen which is illuminated [2.14].

The most crucial part of the microscope is the specimen chamber. This chamber contains the objective lens, objective aperture and the objective stigmator coils. The first intermediate image and diffraction pattern of the specimen are produced by the first objector lens. The objective aperture is found in the back focal plane of the objective lens and is used to enable the operator to control the electrons that will contribute to the formation of the final image of the specimen. The ‘selected area’ aperture is found in the plane of the first intermediate image and allows a certain region of the image to be selected for analysis. The magnification of the image is then controlled by the use of the 1st and 2nd intermediate lenses. The projector lens then assists in magnifying the central part of the image and projects it onto the fluorescence screen which displays the image. A charge coupled device (CCD) camera records the image [2.14].

A TEM can also be used as a scanning transmission electron microscope (STEM) and also conduct electron energy-loss spectroscopy (EELS) through utilising a variety of detectors incorporated in it.

### **2.3.4.3 Scanning transmission electron microscopy (STEM)**

#### **2.3.4.3.1 Introduction**

The scanning transmission electron microscope (STEM) is an invaluable tool for the characterization of nanostructures (e.g. SiNWs), using various imaging modes which the ability to provide information on elemental composition and electronic structure with high precision and resolution to almost that of a single atom. The STEM operation is based on the same principles of the normal scanning electron microscope (SEM) where by, a focused beam of electrons is scanned over the sample and a desired signal is collected from several signals to form an image [2.15].

### 2.3.4.3.2 Imaging in the STEM

A schematic representation of the main components of a TEM with STEM and EELS capability is presented in figure 2.22. In STEM mode, the electron beam production is similar to that during TEM mode until the beam reaches the sample. Upon reaching the sample, a set of scan coils scan the incident probe over the sample and the output signals are collected by a variety of detectors and are used to form an image. In STEM, these multiple detectors are used simultaneously to give different, yet complementary information about the sample.

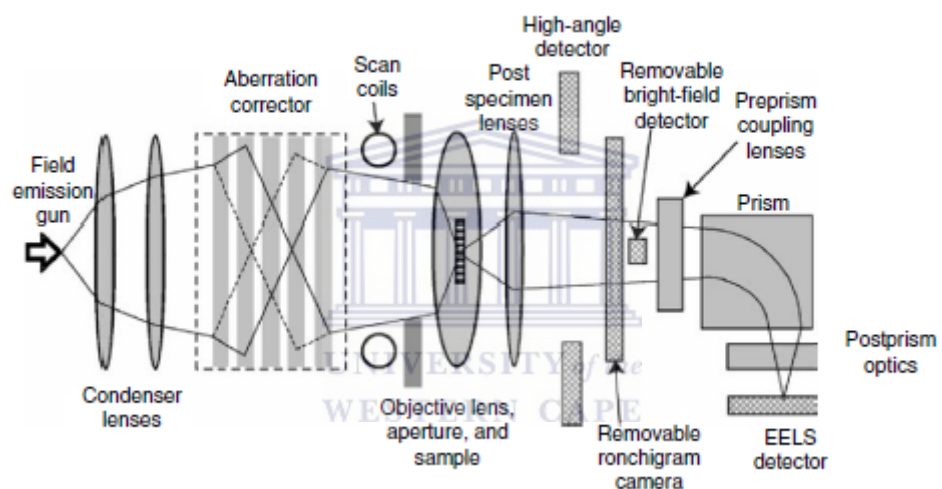


**Figure 2.22:** Schematic diagram of a HRTEM with STEM and EELS capability [2.15].

The common detectors include a bright field (BF) detector which intercepts the transmitted beam and an annular dark field (ADF) detector which collects the scattered electrons signal. The inner angle of this detector can be adjusted to wider angles using specimen lenses from outside the incident beam cone, resulting in maximum collection efficiency of scattered electrons, which then enhances the atomic number ( $Z$ ) dependence of the image contrast. This latter configuration is often referred to as a Z-contrast or high-angle ADF (HAADF) image.

## 2.3.4.4 Electron energy-loss spectroscopy

### 2.3.4.4.1 Introduction

Transmission electron microscopy (TEM) is one of the most superior elemental analysis techniques, with a spatial energy resolution due to thin TEM samples having a shallow interaction volume. For elemental analysis in TEM, electron energy-loss spectroscopy is the most superior technique when compared with TEM-EDS, which is an x-ray based technique with very low signal collection efficiency. During electron beam – sample interactions, the inelastically (energy-loss) scattered electrons containing elemental fingerprints are easily collected using spectrometer positioned below the specimen chamber, along the path of beam as shown in figure 2.23. This enhances the signal-collection efficiency of EELS.

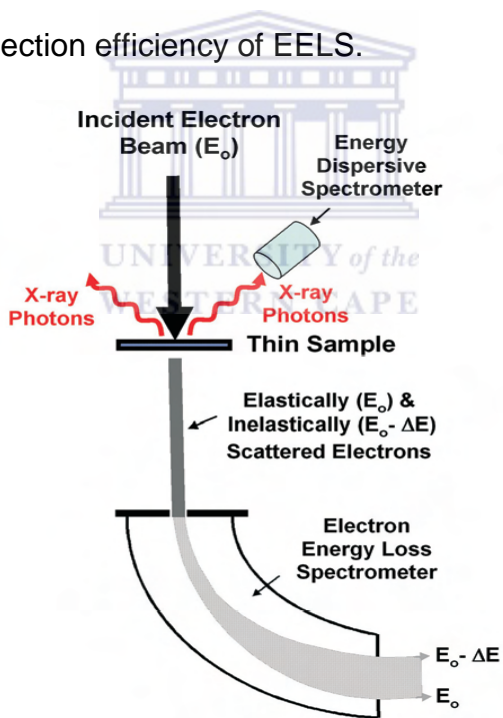
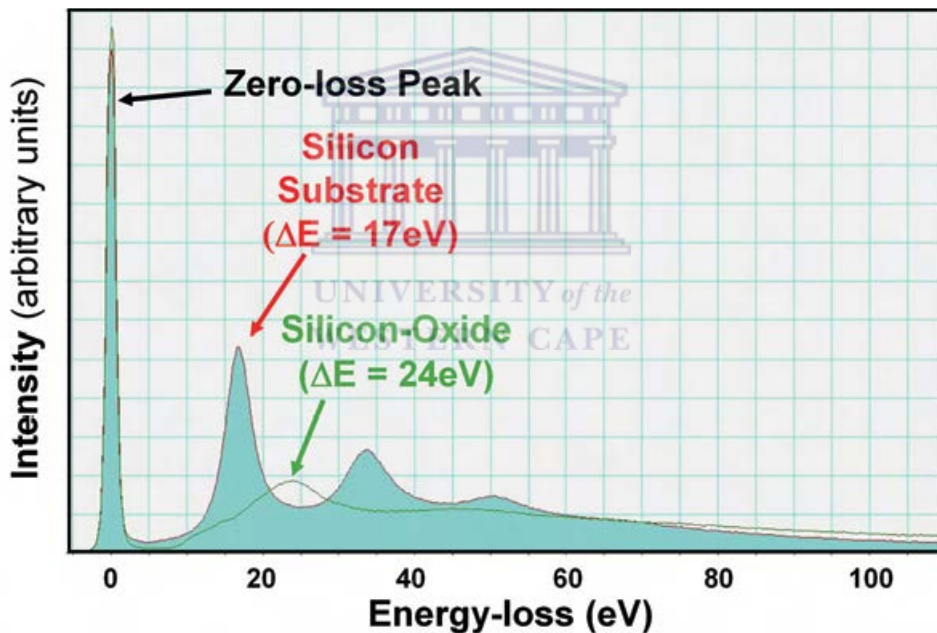


Figure 2.26: Schematic showing EDS and EELS inside a TEM column [2.16].

#### 2.3.4.4.2 Electron energy-loss spectrum

In EELS, the electron beam and sample interactions result in a transmitted beam that is composed of inelastically scattered electrons with characteristic energy losses. This beam of electrons is then directed into a high-resolution electron spectrometer which then separates the electrons according to their kinetic energies and creating an electron energy-loss spectrum plotting the scattered intensity as a function of the decrease in kinetic energy. A typical EEL spectrum showing the low energy-loss range of a silicon-oxide dielectric overlaid on a Si substrate spectrum is presented in figure 2.24.



**Figure 2.27:** Typical EEL spectrum of Si substrate (red) and SiO (green) [2.16].

In a typical EEL spectrum, the x-axis of the plot represents energy loss ( $\Delta E$ ) of the electrons due to inelastic scattering from the sample when the incident beam with energy  $E_0$  is transmitted through the sample. The first zero-loss or elastic peak ( $\Delta E=0$ ) is representative of the electrons transmitted through the sample without any detectable energy loss such as unscattered transmitted electrons. Furthermore, this zero-loss peak also represents the elastically scattered electrons in the forward

---

direction and those that have excited phonon modes with energy losses that cannot be resolved by the system.

Inelastic scattering from the sample outer shell electrons is represented as a peak or multiple peaks for thicker samples, within the 5 – 50 eV region of the spectrum and this region is known as the plasmon region (< 50 eV). In figure 2.24, the low energy-loss peaks for silicon and silicon oxide at 17 and 24 eV respectively, can be attributed to the inelastic scattering from weakly bound electrons [2.16].

#### **2.3.4.5 Sample characterization**

HRTEM, STEM and EELS analysis of the samples was conducted using a Tecnai F20 microscope operated at 200 kV. Sample preparation was done by scrapping off grown SiNWs from the substrate onto the lacey carbon copper grids.

### **2.3.5 Optical Characterization Techniques**

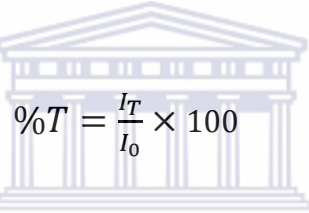
#### **2.3.5.1 Ultraviolet-visible spectroscopy (UV-VIS)**

UV-VIS spectroscopy is a technique that utilizes visible, near infrared and near ultraviolet light to analyse the transmission, absorption and reflective properties of materials (thin films) using an instrument called a spectrophotometer. This technique involves the electronic transitions that occur in samples when they are probed. During an absorption measurement, the UV-VIS measures the electronic transitions from the ground to the excited state and this property is crucial in photovoltaic device applications since it determines the optical band gap of the material. The electronic transitions from the excited state to the ground state are useful in emission spectroscopy.

### 2.3.5.1.1 Theory of UV-VIS

In UV-VIS spectroscopy, when a beam of light is incident on a thin film sample, the electrons of the sample can undergo electronic transitions which may result in transmission, absorption or reflectance of the incident beam of light.

During a UV-VIS transmittance measurement, the intensity of the light passing through ( $I_T$ ) the thin film is measured and compared to the intensity of the light transmitted ( $I_0$ ) by a known reference sample such that the ratio of  $I_T / I_0$  is called the transmittance and denoted as (%T) as shown in (2.4). In thin film measurements, the reference sample is usually a bare standard substrate similar to the one used for growing the thin film.



$$\%T = \frac{I_T}{I_0} \times 100 \quad (2.4)$$

For convenience purposes, the transmittance is given as the %T due to the calibration of most spectrophotometers with a scale of 0 to 100. For non-transparent samples such as Si substrates, the measurement of the amount of light absorbed by the sample is of great importance. This property is called the absorbance (A) and is given by equation (2.5) as:

$$A = \ln\left(\frac{I_0}{I_T}\right) = \ln\left(\frac{1}{T}\right) \quad (2.5)$$

During the incident beam and sample interaction, several electronic transitions can occur. This is due to the fact different materials can absorb different wavelengths of the UV-VIS spectrum. This absorption occurs on the outer electrons and depends on the electron bond strength in that specific material. In terms of strength, electrons can be in different bond states such as strong  $\sigma$  bond, weaker  $\pi$  bond and non-

bonding n states. During the absorption of radiation and excitation, these electrons undergo transitions into anti-bonding states (\*) as shown in figure 2.25.

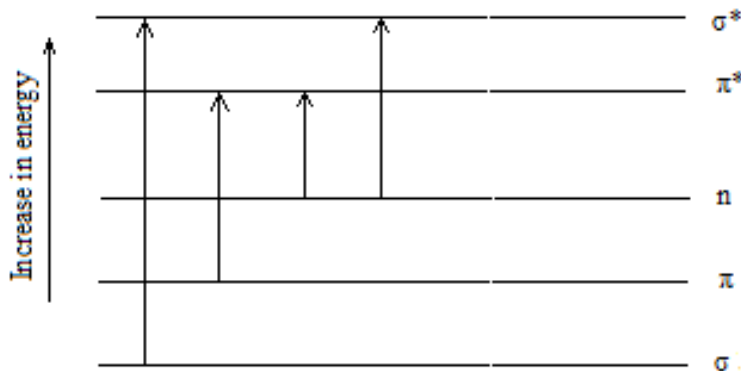


**Figure 2.28:** The bonding and anti-bonding energy transitions [2.17]

Most  $\sigma \rightarrow \sigma^*$  absorptions for individual bonds occur below 200 nm in the vacuum/ultraviolet region and compounds containing just the  $\sigma$  bonds are transparent in the near ultraviolet/visible regions. The  $\pi \rightarrow \pi^*$  and  $n \rightarrow \pi^*$  absorptions occur in the near ultraviolet/visible region.

Similarly, during reflectance measurements of thin films, the reflectance (%R) is given as the ratio of the reflected light over the incident light on the sample. During the measurement of this property, a thin film sample is irradiated with a UV-VIS beam and the light is reflected. The intensity of the reflected beam  $I_R$  is recorded using a spectrophotometer and the reflectance (%R) is then given as the ratio of the  $I_R$  and  $I_0$ , the intensity of light reflected by a known reference substrate as shown in equation (2.6):

$$\%R = \left( \frac{I_R}{I_0} \right) \times 100\% \quad (2.6)$$

This property is also key in the development of photovoltaic devices where materials with enhanced anti-reflective properties are desirable.

### **2.3.5.1.2 Experimental set-up**

To investigate the reflective properties of the Si nanostructures, a Semicon Soft M probe thin film measuring spectrophotometer was used. Halogen and deuterium lamps were used as the visible and ultraviolet light sources respectively. A schematic representation of the experimental set up is show in figure 2.26.

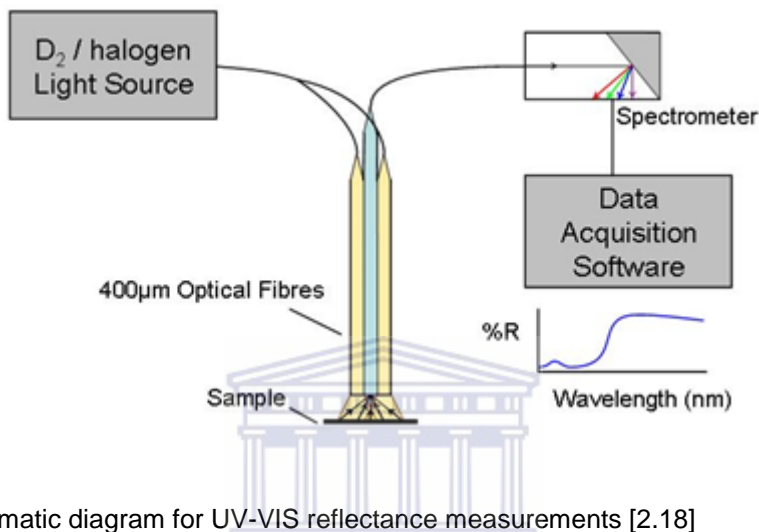


**Figure 2.29:** Schematic diagram for UV-VIS reflectance measurements [2.18]

UNIVERSITY of the  
WESTERN CAPE

### **2.3.5.2 Photoluminescence (PL) spectroscopy**

PL spectroscopy is a non-destructive technique that is utilized to investigate the optical or light emission properties of nanostructures for photovoltaic and other opto-electronic applications. This technique can be used to study the electronic structures of different materials and also determine the quantum confinement effects in structures such as nanowires. In simpler terms, PL spectroscopy involves the excitation of electrons using a laser beam of known wavelength whereby the electrons absorb the laser photons and get excited into higher energy states in the conduction band. At the conduction band these electrons de-excite through photon emission and move back into the valence band.

### 2.3.5.2.1 Theory of photoluminescence

In photoluminescence, a laser source is used to generate a laser beam of known wavelength with energy ( $h\nu$ ) higher than optical band gap energy ( $E_g$ ) of the material. This laser beam is then used to excite the electrons in the sample through absorption of the incident laser photons. During absorption, the electrons get excited from their ground states into higher excited states in the conduction band leaving a hole in the valence band hence electron-hole pairs (exciton) are created.

In the conduction band, the electrons experience energy and momentum relaxation from higher states to the minimum of the conduction band through non-radiative or phonon relaxation. From the conduction band minimum, several radiative recombination processes are possible as illustrated in figure 2.27 [2.19].

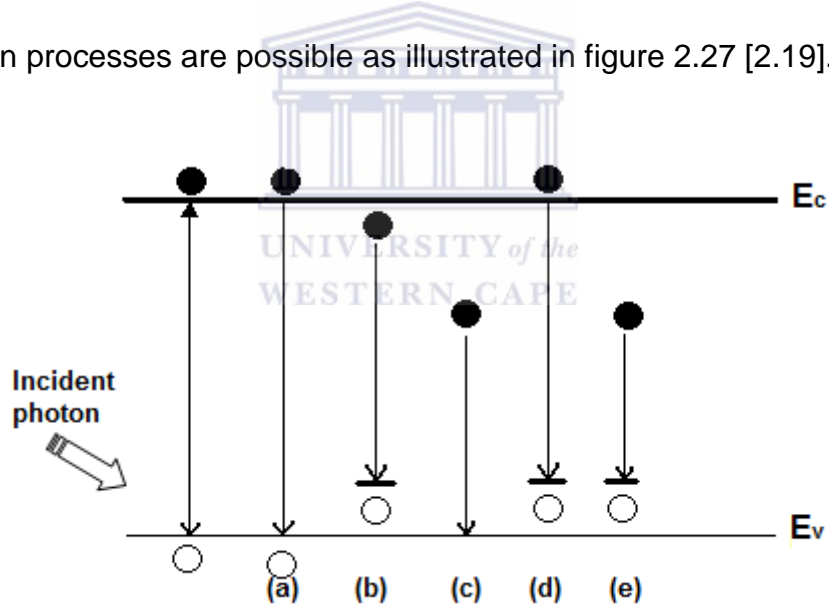


**Figure 2.27:** Radiative recombination processes in photoluminescence [2.19]

Figure 2.27 (a) demonstrates a band-to-band recombination process which mostly occurs at room temperature and has a low probability of occurring at low temperatures due to the large orbital radii and thermal quenching effects in materials with small effective masses. In (b), an exciton recombination process is demonstrated between a bound electron-hole pair in a hydrogen-like state. This free

exciton possesses energy less than that the required band gap energy necessary for the formation of an unbound electron-hole pair. In direct band gap semiconductors, exciton recombination results in the emission of a photon and the energy E, of the emitted photon is given by:

$$E = E_g - E_x \quad (2.7)$$

where by  $E_x$  is the exciton binding energy. In the case of indirect band gap semiconductors, a phonon is also emitted as a requirement for momentum conservation and the energy of the photon E, is given in equation (2.8) as:

$$E = E_g - E_x - E_p \quad (2.8)$$

where by  $E_p$  is the phonon energy. In impure materials, the bound exciton recombination is the most dominant process compared to the free exciton recombination. In figure 2.27 (d), an electron and a hole in a neutral acceptor recombination is shown while an electron on a neutral donor combining with a hole on a neutral acceptor is shown in figure 2.7 (e). This process is known as the donor – acceptor recombination process.

During donor and acceptor recombination, the energy of the emission line due to the coulombic interactions between donors and acceptors is given by equation (2.9):

$$E = E_g - (E_A - E_D) + \frac{e^2}{\epsilon \epsilon_0 r} \quad (2.9)$$

Where  $E_A$  and  $E_D$  are the acceptor and donor energy levels, respectively,  $r$  is the distance between donor and acceptor,  $\epsilon$  is the dielectric constant of the material,  $e$ , the charge of an electron and  $\epsilon_0$  is the permittivity of free space.

### **2.3.5.2.2 The experimental set-up**

The main components of a PL system are an optical laser source, an optical system (lenses and mirrors) and a spectrophotometer as shown in the schematic diagram, figure 2.28. During PL measurement, a laser is generated at the source and is directed to the sample surface by the optical system. Upon reaching the sample, excitation and e-excitation occurs resulting in the emission of a beam of luminescence photons and the optical system filters any reflected laser such that only the luminescence signal reaches the spectrometer and is processed into an electronic signal and displayed on the computer screen.

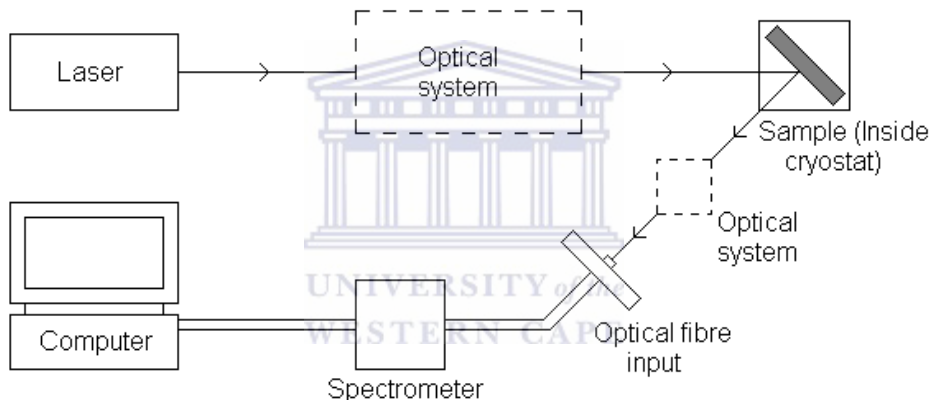


**Figure 2.28:** Photo of a NanoLog® Horiba spectrofluorometer

In this work, a NanoLog® Horiba spectrofluorometer was used to study the photoluminescence properties of the grown samples using a 325 nm Xe laser in the range 325 to 620 nm.

---

## 2.4 REFERENCES

- 2.1. F. R. Cummings, Msc Thesis, University of Western Cape, South Africa (2006)
- 2.2. C. J. Oliphant, MSc Thesis, University of Western Cape, South Africa (2008)
- 2.3. K. Howard, A. Johnson, K. McMichael and M. T. Postek, in 'Scanning Electron Microscopy - A Students Handbook', Ladd Research Industries, Inc., Burlington (1980)
- 2.4. P. J. Goodhew and F. J. Humphreys, in 'Electron Microscopy and Analysis', 2nd Edition, Taylor & Francis, London (1988)
- 2.5. L. Langford, D. Louer, E. Sonneveld, J. Visser, Powd Diffrr. 1(3), (1986) 211-221
- 2.6. B. D. Cullity, in 'Elements of X-ray diffraction', Addison-Wesley Publishing Company, Reading, Massachusetts (1978)
- 2.7. A. Patterson, Phys. Rev. 56(10), (1939) 978
- 2.8. C. S. Kong, MSc Thesis, University of Malaya, Kuala Lumpur (2012)
- 2.9. J. Niu, D. Yang, J. Sha, J. N. Wang, M. Li, Mat. Lett. 61, (2007) 894-896
- 2.10. W. S. Lau, in 'Infrared Characterization for Microelectronics', World Scientific, Singapore (1999)
- 2.11. L. Cui, W. W. Xia, F. Wang, L. J. Yang, Y. J. Hu. Phys. Rev. B. 409(2013) 47-50
- 2.12. Q. Hu, H. Suzuki, H. Gao, H. Araki, W. Yang, T. Noda, Chem. Phys. Lett. 378, (2003) 299-304
- 2.13. C. T. Kirk, Phys. Rev. B 38, (1998) 1255
- 2.14. D. Chescoe, P. Goodhew, in 'The operation of the transmission electron microscope', New York: Oxford University Press, (1984)

- 
- 2.15. S. J. Pennycook, in 'Advances in Imaging and Electron Physics', Elsevier Science, New York, 123 (2002) 173-206
- 2.16. S. Subramanian, G. Clark, K. Ly, T. Chrastecky, EDFAOO, 13 (1) (2011) 20-28.
- 2.17 B. A. Van Heerden, MSc Thesis, University of Western Cape, South Africa (2009)
- 2.18 B. S. Swain, B. P. Swain, S. S. Lee, N. M. Hwang, J. Phys. Chem. C, 116, (2012) 22036-22042
- 2.19 D. K. Schroder, in 'Semiconductor Material and Device Characterization', Wiley Interscience, New York, (1990)



---

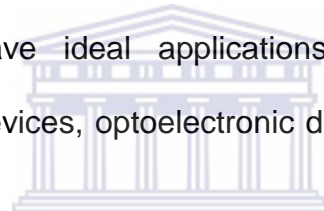
# CHAPTER 3

## 3 RESULTS AND DISCUSSION

---

### 3.1 INTRODUCTION

In the semiconductor industry, silicon (Si) has always been the core material and technological advancements in microelectronics have always depended on its research developments [3.1]. In recent years, one-dimensional (1D) nano-scale materials have attracted a lot of interest from researchers, due to their unique physical, mechanical, optical and other novel properties. Si and silica ( $\text{SiO}_x$ ) nanostructured materials have ideal applications in several fields; such as mesoscopic research, nanodevices, optoelectronic devices, nanoscale logic and 1D quantum transistors [3.2, 3.3].



UNIVERSITY of the

Si nanowires (SiNWs) are one-dimensional, thin hair-like structures that have diameters below 100 nm and a length of up to hundreds of nanometres [3.4]. The geometry of these nano-scale 1D SiNWs is consequently responsible for the high surface area to volume ratio, the nanoscale radius of curvature and the phenomenal mechanical flexibility [3.4]. In SiNWs, the increased surface to volume ratio means that the surface and interfaces are much more effective than in bulk Si. At the nano-scale, the fundamental electronic band structure of Si is altered as a result of quantum confinement effects; hence improving the optoelectronic properties of Si for photovoltaic applications [3.1].

The fabrication of such novel structures can be achieved using both ‘top down’ approaches; such as lithographic patterning, and ‘bottom up’ approaches; like

chemical synthesis [3.1]. During ‘top down’ synthesis of Si NWs, an existing Si layer or Si substrate can be etched to produce NWs using both dry and chemical etching; such as plasma etching and hydrofluoric acid etching. However, the huge costs and complexity of equipment associated with dry etching, makes it a less favourable technique for Si NW growth. With the ‘bottom up’ synthesis method, growth of Si NWs involves an atom-by-atom growth process from various Si precursors. The various techniques that exploit the ‘bottom up’ approach include laser ablation, magnetron sputtering, solution based growth, thermal evaporation and chemical vapour deposition (CVD); with the latter being the most common technique [3.5].

Some of the most common Si NW growth mechanisms involved during ‘bottom up’ synthesis of NWs include vapour-liquid-solid (VLS) [3.6], vapour-solid-solid (VSS) [3.7], solid-liquid-solid (SLS) [3.8] and oxide assisted growth (OAG) [3.9] with VLS being the most widely adopted growth mechanism. During VLS growth mechanism, a metal catalyst is used to initiate and direct the growth of SiNWs where-by the size of the metal catalyst particle determines the diameter while the length is dependent on the growth duration [3.1]. In VLS mechanism, SiNW growth undergoes three critical stages namely, (1) alloying, (2) nucleation and (3) growth [3.5]. In this process, growth temperatures higher than the eutectic temperature of the metal catalyst-Si alloy are crucial to allow alloying and formation of nucleation sites for SiNWs [3.6].

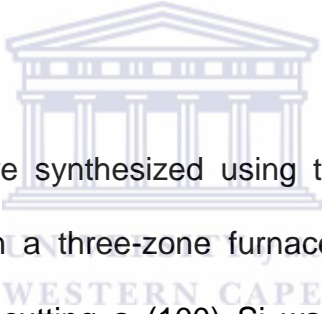
The use of ‘bottom-up’ synthesis techniques, like CVD, enables control of deposition parameters which can lead to production of high quality crystalline SiNWs with fewer structural defects [3.10, 3.11]. There are several variants of the CVD technique that can be used for SiNW synthesis; depending on parameters like operating pressure and precursor treatment such as thermal CVD (TCVD) where by a powder source is

---

heated to produce the precursor vapour. Controlling the base pressure of a CVD reactor to even ultra-high vacuum, if possible, is crucial in controlling contamination of SiNWs and promoting growth at lower temperatures [3.11].

In this chapter, we report on the compositional, structural and optical properties of SiNWs grown by thermal CVD. Initially, the role of the metal catalyst during nanowire growth shall be investigated followed by the effect of growth temperature on the grown structures. During TCVD, the reaction zone length is a crucial parameter; hence the need to understand the influence of the substrate position with reference to the source. Finally, we will interrogate the relationship between the structural and optical properties of the SiNWs.

## 3.2 EXPERIMENTAL

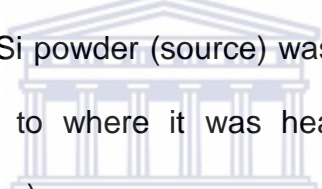


Si nanostructures (fibres) were synthesized using the thermal CVD method in a horizontal alumina tube within a three-zone furnace. During sample preparation, substrates were prepared by cutting a (100) Si wafer into several 1 cm × 1 cm samples, which were then carefully marked on the backside in order for them to be distinguishable from each other. To clean these samples, a simple procedure was followed which involved ultrasonic cleaning of the samples in acetone for 5 minutes followed by 5 minutes of ultrasonic cleaning in ethanol. Furthermore, these samples were dipped in isopropanol for another 5 minutes after which they were allowed to air dry before the final cleaning step. The final cleaning step involved dipping the samples in 5% hydrofluoric acid (HF) solution for 1 minute and then allowed to air dry; hence ready for metal catalyst deposition.

Au and Ni thin films of varying thicknesses were deposited on the cleaned Si substrates using a Quorum 150TES sputter coater. During sputter deposition, the

Film Thickness Monitoring (FTM) profile was used such that whenever the desired film thickness was reached, the sputtering stops automatically. For the Au sputtering, a 99% pure Au target was sputtered with a current of about 20 mA at a pressure of about  $10^{-2}$  mbar for different durations to achieve the various thicknesses. The Ni thin films were also sputtered from a 99% Ni target with current of about 100 mA at a pressure of about  $10^{-2}$  mbar. After the metal thin film depositions, the samples were now ready for Si nanostructure growth.

To synthesize Si nanostructures, a Brothers X1600MT, 3 zone thermal CVD furnace with a horizontal Alumina tube at atmospheric pressure, was used for the thermal evaporation of Si powder for the growth of Si nanostructures. A small amount of ~ 20g of Sigma Aldrich 99.99% Si powder (source) was placed in a ceramic boat and placed at a specific position to where it was heated to its fixed, vaporization temperature (39 cm into the tube).



Before heating, the system was purged with a high flowing argon (Ar) gas for 30 minutes to provide an inert growth environment. This flow rate was maintained during the gradual ramping up of the zones from room temperature to the desired values at a steady rate of 10 °C/minute. Upon reaching the desired temperature, deposition was allowed to occur for 1 hr, after which the temperatures would start dropping down to room temperature still under the steady flow of argon gas. In this thesis; the deposition pressure, source vaporisation temperature and Ar gas flow rate were fixed at atmospheric pressure, 1000 °C and 150 cm<sup>3</sup>/min. The parameters that were investigated during the growth of the Si NWs are summarized in table 3.1. The substrate temperature,  $T_{\text{substrate}}$  was increased from 800 – 1200 °C (series B) and the source-to-substrate distance,  $d_{\text{s-s}}$  was changed from 5 – 17 cm (series C).

These conditions were chosen based on previous successful Si NW synthesis by our group using the Ni catalyst, and are to be considered the standard conditions, unless otherwise stated. It should be noted that the effect of the catalyst will also be reported on in the next section (series A).

**Table 3.1:** Deposition parameters used for the deposition of Si NWs.

Series	Catalyst	Substrate temperature (°C)	d <sub>s-s</sub> (cm)
A	None, Au, Ni	1000	11
B	Ni	800 – 1200	11
C	Ni	1000	5 – 7

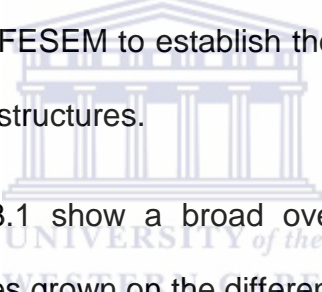
Scanning electron microscopy was used to study the morphological properties of the grown SiNWs. A high resolution Auriga FESEM, operating at about 5.0 kV and equipped with an electron dispersion spectrometer, was used to obtain SEM micrographs and also conduct EDS analysis of the grown samples. Fourier transform infra-red (FTIR) analysis of the samples, was conducted using a Perkin Elmer Spectrum 100, ranging from 400 – 4000 cm<sup>-1</sup> in order to establish the chemical composition and bonding configuration of the grown SiNWs. A Panalytical X`pert PRO PW3040/60 X-ray diffractometer, was used for X-ray diffraction (XRD) analysis, ranging from 0 – 90° (2θ) in order to ascertain crystallinity and phase identification in the grown SiNWs. A Tecnai F20 system was utilised for the TEM, STEM and EELS analysis of the samples while the photoluminescence of the samples was investigated using a Horiba NanoLog®, spectrofluorometer with a 325 nm Xe laser as excitation source. The UV-VIS measurements were done using a Semicon Soft M probe thin film measuring system with a deuterium and halogen as UV and VIS lamps respectively.

---

### 3.3 COMPOSITION AND STRUCTURAL PROPERTIES

#### 3.3.1 *The Effect of Metal Catalyst on Si Nanostructure Growth*

In this sub-section, the influence of a metal catalyst such as gold and nickel on the growth of silicon nanostructures is investigated. From the three samples, one was left as a bare wafer while the other two were sputter coated with a 10 nm thin film of nickel and gold respectively. To grow the Si nanostructures, all three samples were thermally annealed in an argon (Ar) ambient and pure silicon powder as the source material inside a Brothers X1600MT Thermal CVD system at 1000 °C. During this process all parameters were kept constant except the absence of catalyst being the only variable amongst the samples. These grown samples were then characterized using a high resolution Auriga FESEM to establish the morphology and approximate composition of the grown nanostructures.



The SEM images in figure 3.1 show a broad overview of the distribution and morphology of Si nanostructures grown on the different substrates. In (a), the sample without a metal catalyst, we observe a very sparse and stunted growth of nanostructures and these structures have no clear defined dimensions. From the sample in (b), coated with a gold film, clusters of thin wire-like structures are seen to have grown on specific regions of the sample and not homogeneously distributed. Few, long thin wire-like structures stretch from the cluster across the sample while the remainder of the sample is covered by shorter kinked hair-like structures.

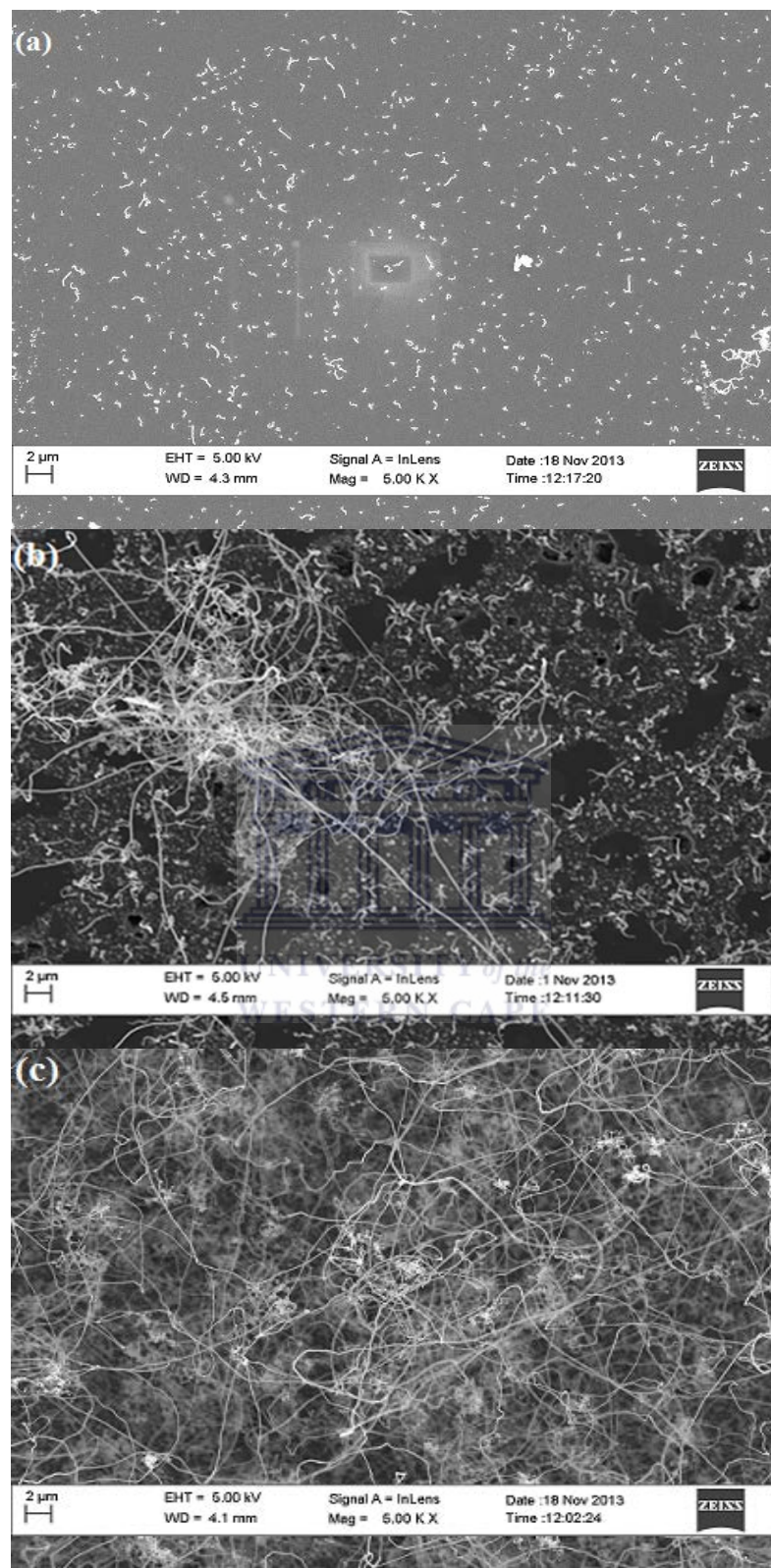


**Figure 3.1:** FESEM images of silicon nanostructures grown on (a) a bare Si wafer, (b) a 10 nm Au thin film, and (c) a 10 nm Ni thin film, at a temperature of about 1000 °C and 150 sccm Ar gas flow rate at atmospheric pressure.

The nickel coated sample, in (c), shows a high yield and dense growth of lengthy, silicon wire-like nanostructures distributed throughout the sample surface.

From the observations made from these samples, it is evident that the metal catalyst layer deposited on the substrate is indeed necessary for the synthesis of long, dense and thin well defined silicon nano-fibre structures.

The high magnification SEM image and EDS spectrum in figure 3.2 reveals more information about the morphology, shape and size of the structures produced during synthesis without a metal catalyst; whereby the dark and bright areas represent the substrate and grown structures, respectively. This image shows an isolated, short, silicon rod-like structure with a sharper tip surrounded by a very small cluster of fewer and shorter similar structures. This observation is analogous to the observation made by Bandaru *et al* [3.1] whereby he synthesized silicon nanowires without a catalyst which had sharper tips instead of spherical ones. This then rules out the possibility of VLS growth mechanism, hence in this case, the sharp tip of the nanowire can be attributed to the lack of the spherical metal catalyst which is responsible for silicon nanowire nucleation during VLS growth.

Due to the presence of oxygen, as indicated by the EDS spectrum, it is evident that the oxide assisted growth (OAG) mechanism is responsible for the growth of these structures [3.12]. The trace amounts of oxygen from the atmosphere remaining in the tube and from the Ar carrier gas impurity can be identified as promoting the OAG mechanism. The low yield obtained with this mechanism, is similar to the observation made by Lee *et al* [3.9], whereby pure Si powder target source yielded very low nanowire yields compared to  $\text{SiO}_2$  containing powder source. This gaseous  $\text{SiO}$  species then decomposes on the surface of the Si wafer substrate to form

nanoparticles which then agglomerate to form Si nanowires [3.1]. These Si nanoparticles act as the nucleation sites for the Si nanowire growth within the oxide layer matrix and their arrangement is responsible for the nonlinear morphology of the Si nanowires obtained.

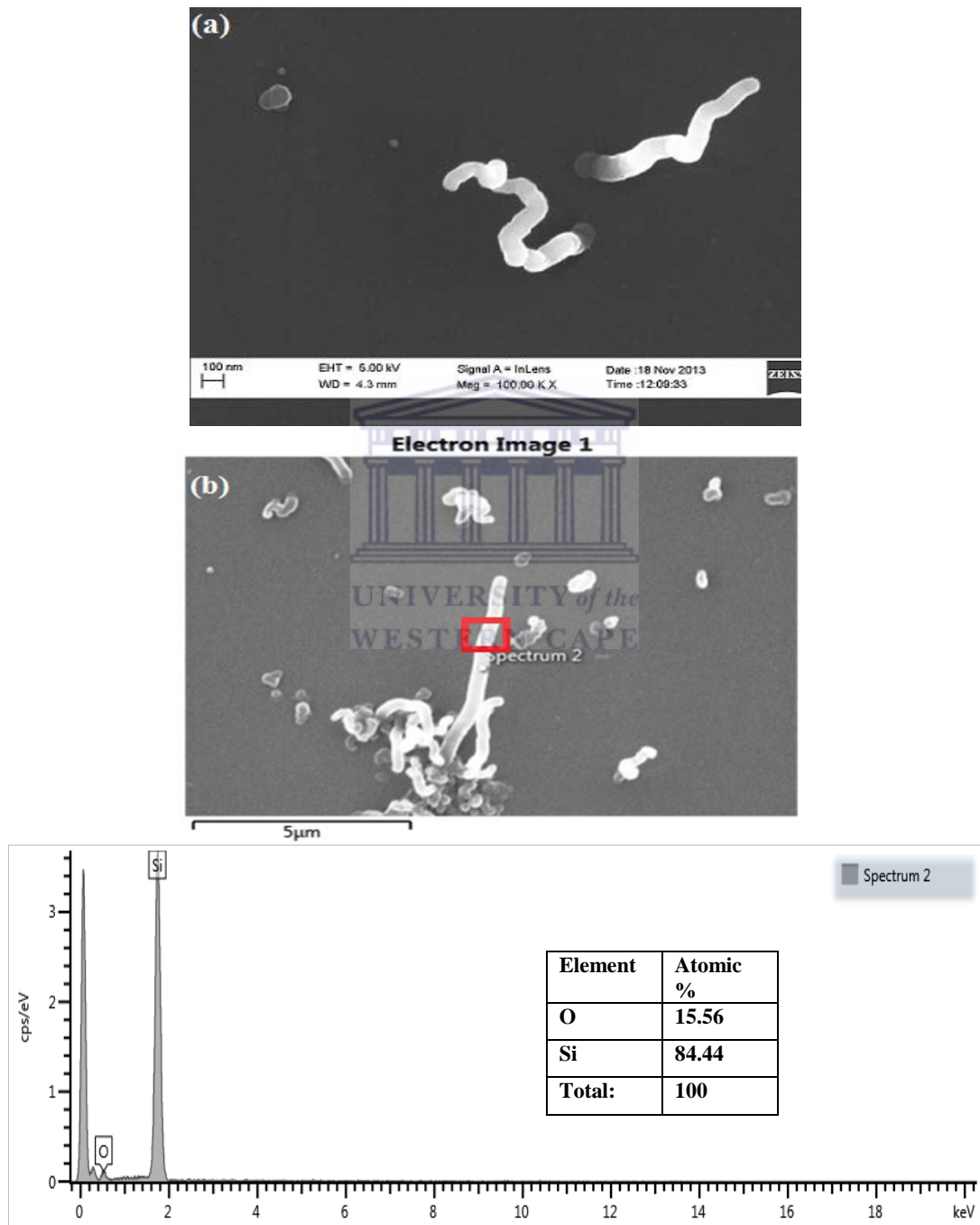


**Figure 3.2:** SEM image of a silicon nanostructure showing; (a) a high magnification of a Si fibre, (b) the area on the sample from which the EDS spectrum 2 was obtained.

The EDS spectrum taken from the length (body) of the wire and marked as spectrum 2, gives an approximation of the composition of the fibre at that point and surrounding areas (marked with a square). This is due to the limitations of the EDS equipment such as, beam diameter and interaction volume, hence incapable of specific spot analysis. The chemical composition does reveal a significant amount of oxidation of the nanofibres which is as a result of the possible oxygen sources mentioned previously.

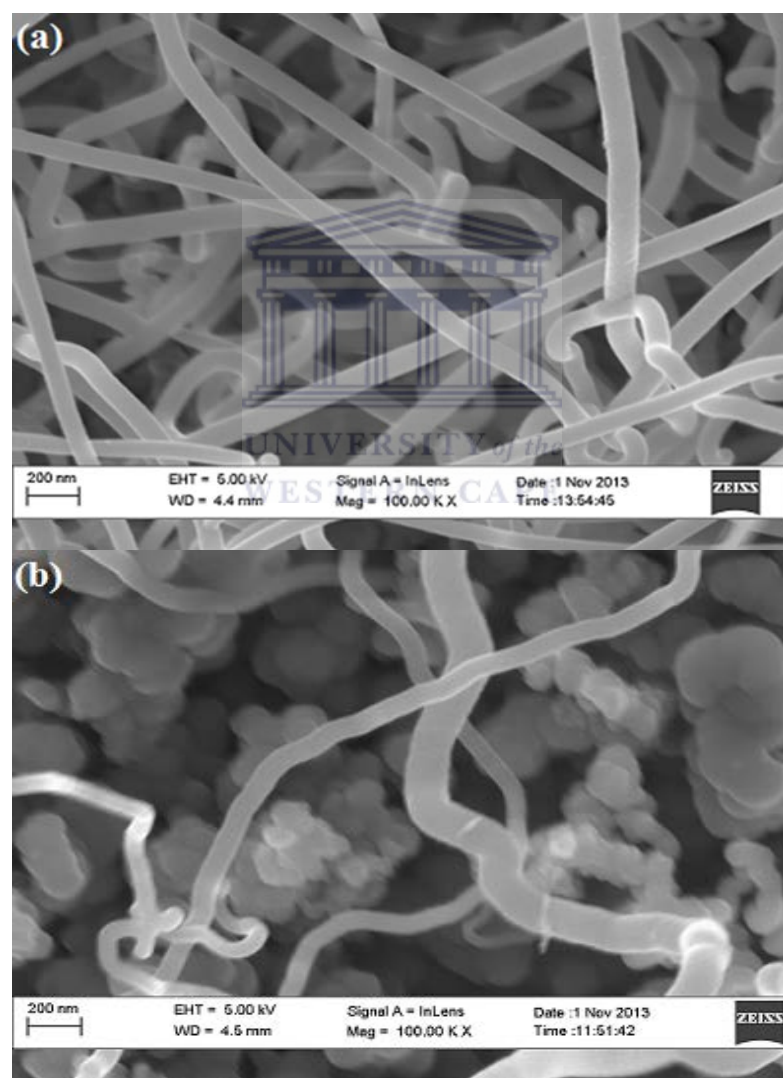


**Figure 3.3:** High magnification SEM micrographs of (a) Ni 10 nm, (b) Au 10 nm metal catalyst coated samples.

---

The SEM micrographs presented in figure 3.3 show images of Si nanofibres grown from a (a) nickel and (b) gold coated Si substrates. In (a) we observe the growth smooth, long and densely packed one-dimensional structures while in (b) there is less growth of Si nanofibres resulting in less dense structures with a wide range of sizes compared to those grown on Ni coated substrate. This trend can be attributed to the evaporation of some of the Au nano-islands and joining of the Au islands at higher annealing temperatures resulting in fewer nucleation sites for the nanowires at higher temperatures. This observation is analogous to that made by Klimovskaya *et al*, where by the annealing of Au/Si structures did not yield Au nano islands but resulted in Au film recrystallization [3.13].

The SEM images in figure 3.4 show Si nanofibres which have spherical tips, marked with a square and catalysed with Ni (a) and Au (b). These areas marked with a square represent the interaction area on the sample during EDS analysis due to limitations of the equipment such as, beam size and lack of spot analysis. The EDS spectra, shown in figure 3.4 (c) and (d) give an approximate chemical composition of the tips of the nanofibres grown from a Ni and Au catalyst respectively. Furthermore, the EDS confirmed the presence of metal catalyst at the tips of the fibres and significant oxidation of structures grown.

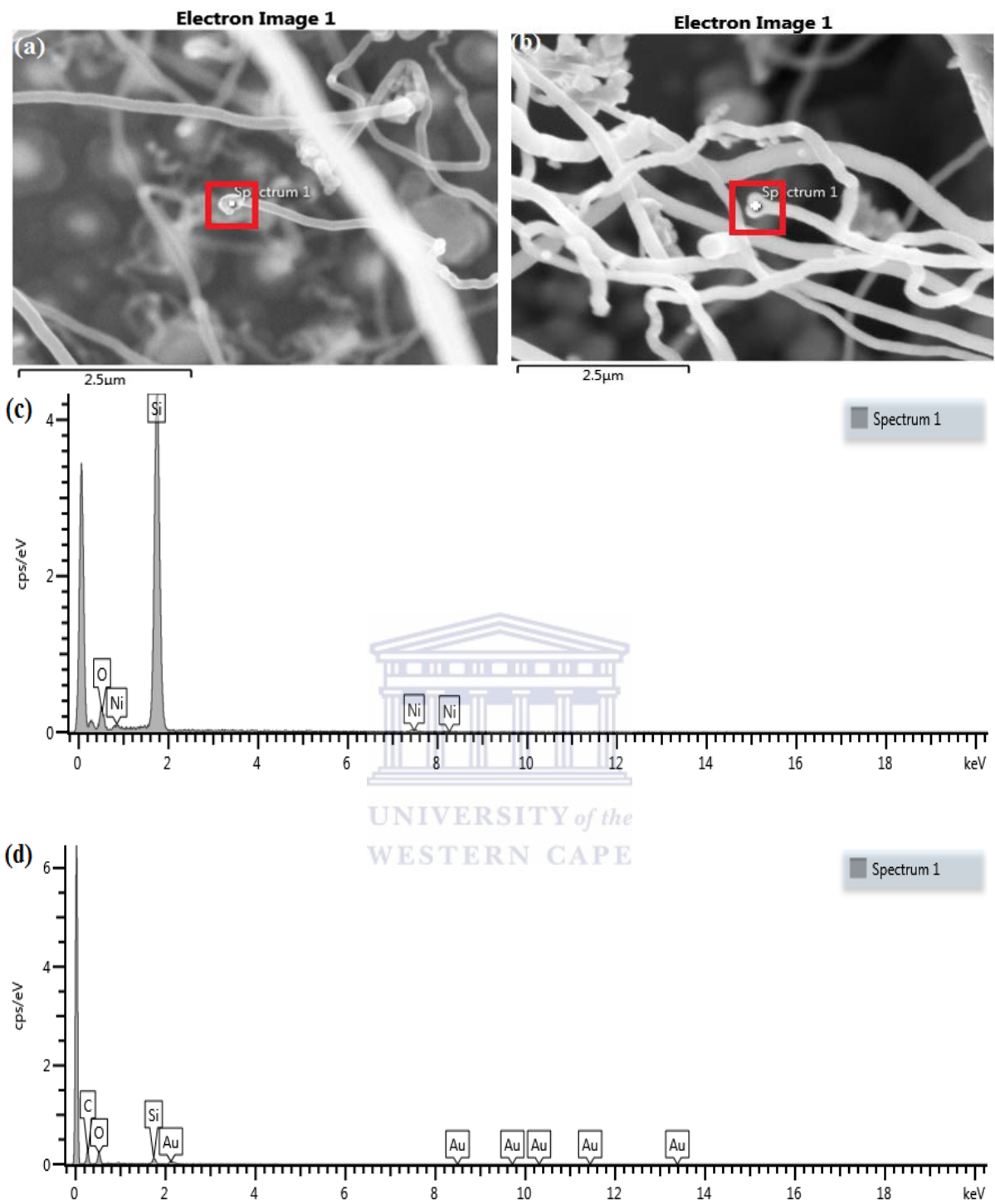


**Figure 3.4:** SEM micrographs of Si nanofibres grown on (a) Ni 10 nm (b) Au 10 nm, with the squared area marking the EDS sampled. The EDS spectra shown were acquired from the tips of nanofibres catalysed with (c) Ni and (d) Au.

The dense growth and spherical tip of these grown structures reveals the dominance of the Metal Catalysed VLS growth mechanism (MC-VLS) [3.14] and is confirmed by the presence of the metal catalyst at the tip. During the nanofibre growth, the liquid

---

alloy remains at the tip of the wire as an adsorption site for more source vapour component resulting in growth of long nanofibres. In this method, the size and position of the nanowire is determined by the diameter and position of the metal catalyst droplet precipitating it [3.11, 3.14]. Therefore, the non-uniform diameters of the nanofibres on these samples can be attributed to the non-uniform size of the liquid alloy droplets formed during dewetting. Furthermore, as a consequence of oxygen detected during EDS acquisition, the dense growth of nanowires on these samples can not only be attributed to the VLS mechanism but a combination of both OAG and VLS [3.15] to produce these densely grown nanowires.

The OAG is more likely to occur on the exposed Si substrate regions after dewetting of the thin film to form liquid alloy droplets. A combination of both using a metal catalyst in combination with the oxide assisted growth is called silicon monoxide vapour-liquid-solid (SiO-VLS) [3.16], and combines the position control by metal catalyst with the simple based growth mechanism based on the SiO powder which is obtained during heating of pure Si powder in the presence of traces oxygen remnant in the tube.

From the work and observations made, it is sufficient to conclude that it is necessary to use a metal catalyst when synthesising Si nanowires with the present experimental setup since it yields more Si nanowires with a more defined shape and size.

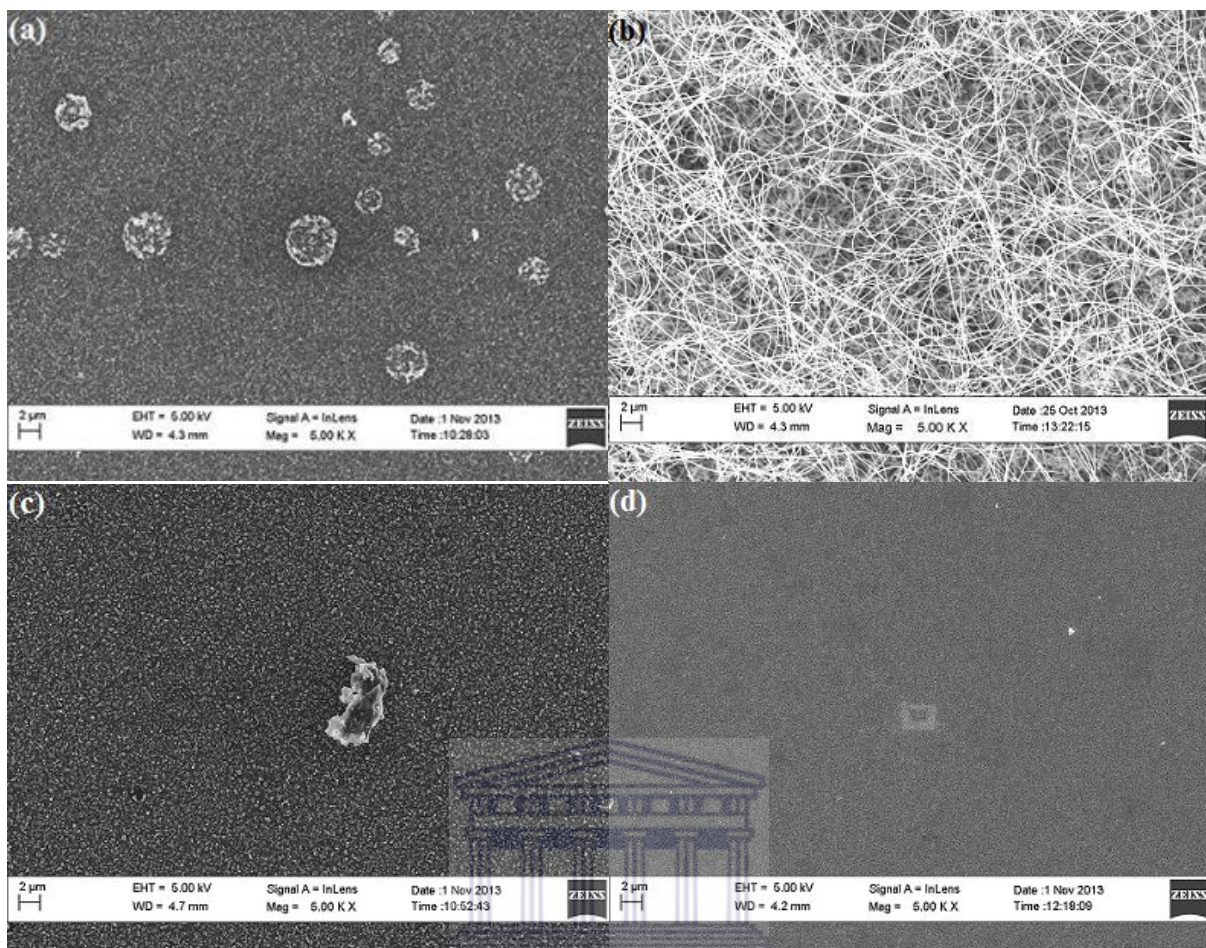
---

### **3.3.2 *The Effect of Temperature on the Growth of Si-Nanostructures***

It is widely accepted that the substrate temperature is the most important deposition parameter to consider during the growth of nanostructures by chemical vapour deposition [3.17]. As an example, it was demonstrated that the onset of crystallinity in nanocrystalline silicon thin films and its resultant optical and electronic properties are strongly affected by the substrate temperature [3.17 - 3.19]. Therefore, in this section we report on the effect of the substrate temperature on the structural properties of the Si nanostructures (series B).

#### **3.3.2.1 *Scanning electron microscopy (SEM)***

As a first line of characterisation, scanning electron microscopy was used to probe the morphological and compositional properties of the Si nanostructures. Figure 3.5 shows the low magnification FE-SEM micrographs of samples deposited at substrate temperatures of 1200, 1000, 900 and 800 °C. The remarkable highlight in these micrographs is that the sample grown at 1000 °C is the only sample with fibre-like nanostructures. The sample surface is densely and homogeneously covered with the spaghetti-fibre-like, intertwined nanostructures with lengths up to several micrometres.



### UNIVERSITY of the WEST INDIES

**Figure 3.5:** FESEM overview images of samples grown on Ni coated Si wafer substrates at temperatures of (a) 1200 °C (b) 1000 °C (c) 900 °C (d) 800 °C.

Closer inspection of the samples is illustrated in the high magnification FE-SEM micrographs of the samples as shown in figure 3.6. In figure 3.6(a), the sample grown at 1200 °C shows agglomerates of irregular-shaped, small particles with individual diameters of up to 50 nm. On this sample, there is no evidence of wire or rod-like structures growth on the sample. The lack of growth of such structures even in the presence of Si vapour can be attributed to the vaporization of the droplets at sufficiently high temperatures above 1100 °C and the dissociation of the  $\text{SiO}_x$ . This observation is consistent with that observed by Song *et al* [3.19].

Figure 3.6(b) shows the sample grown at 1000 °C with densely packed Si wire-like or rod-like structures grown in random orientations. These structures were analysed and found to be long up to microns in length and were of non-uniform diameters.

On the samples grown at 900 and 800 °C (figure 3.6 (c) and (d)), there was only evidence of formation of large irregular shaped structures of different sizes without any traces of wire-like structures. Furthermore, the sample deposited at 900 °C shows evidence of the dewetting process, whereby parts of the substrate were exposed, and is represented by a smooth dark background with no structures grown on it. Since these temperatures are below the Ni-Si eutectic alloy temperature range, the VLS growth mechanism is useful in accounting for the absence of Si nanofibre structure growth at such low temperatures.

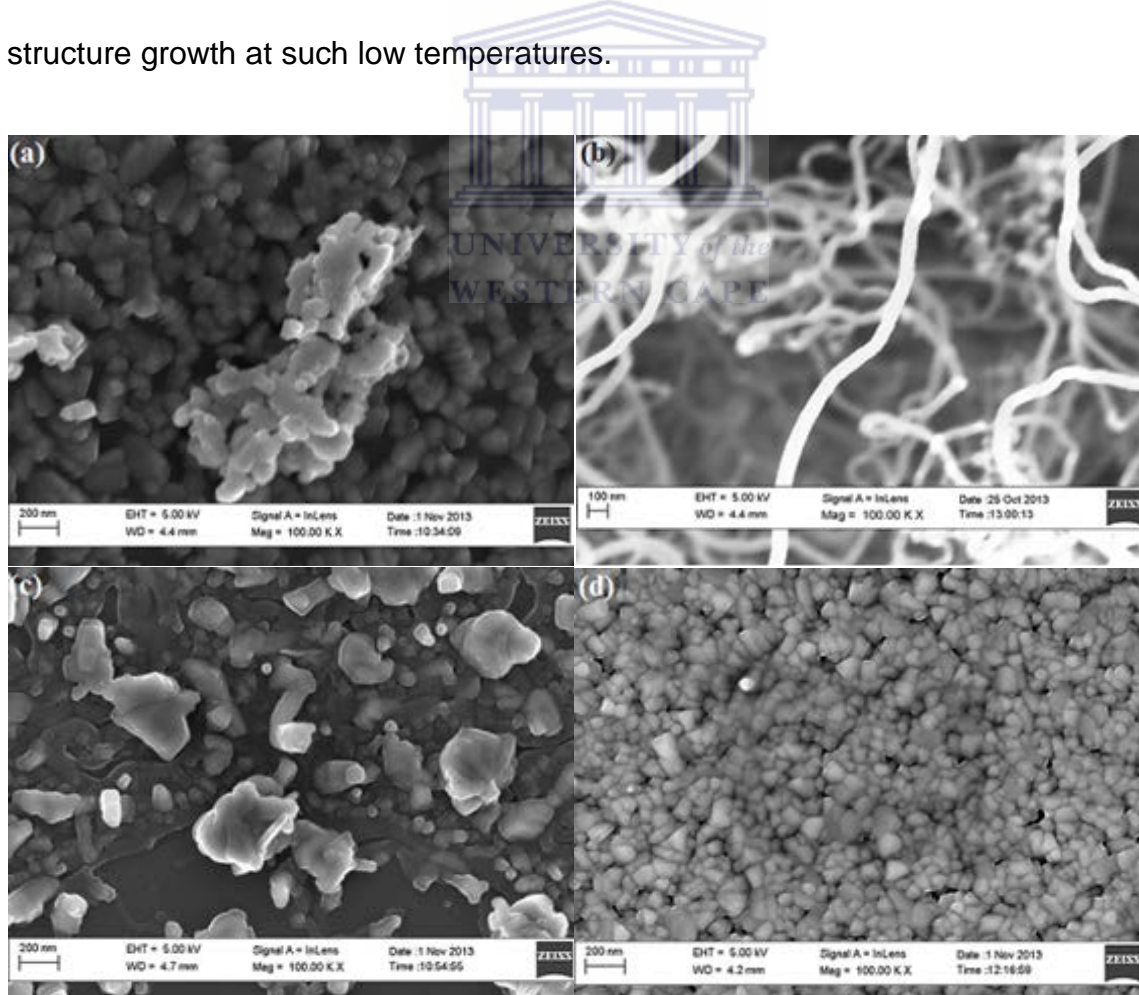


**Figure 3.6:** High magnification SEM micrographs of silicon nanostructures grown on Ni coated Si substrates at different temperatures (a) 1200 °C (b) 1000 °C (c) 900 °C (d) 800 °C

Detailed size-analysis of the Si nanostructures found on the sample grown at 1000 °C, as shown in Figure 3.7 was performed, and it reveals a relatively good diameter distribution with an average size of ~ 57 nm.

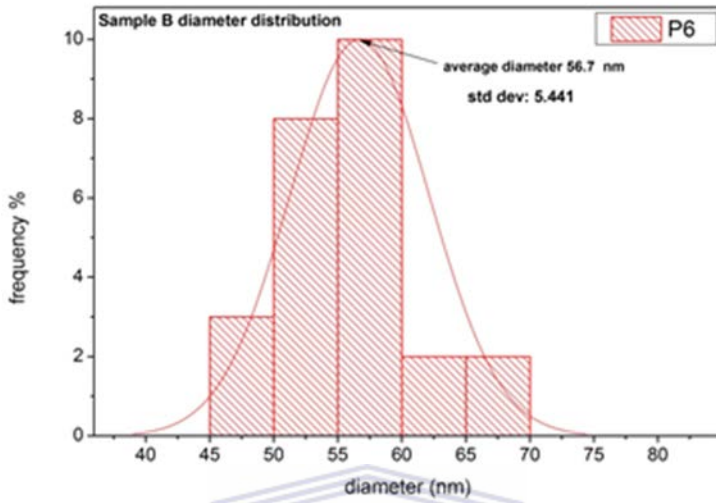


**Figure 3.7:** A histogram showing the diameter distribution of the Si nanofibres grown at 1000 °C.

Some of the grown Si nanofibres were found to have spherical tips which suggested a tip or root growth mechanism even though it was difficult to locate the tip or root of the nano-fibres due their superior length and high density. This observed growth of nanofibres can be attributed to the growth temperature being within the Ni-Si eutectic alloy temperature range [3.18], where the Ni-Si eutectic alloy does not vaporize after supersaturating with Si but grows into  $\text{SiO}_x$  nanofibre structures.

### **3.3.2.2 EDS Analysis of Si nanostructures**

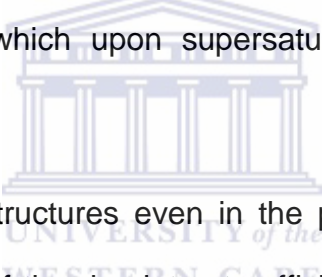
The EDS analysis was conducted on all the produced samples in order to obtain a preliminary view of the chemical composition of the different samples. Figure 3.8 shows the SEM images and corresponding EDS spectra adjacent to the images of the samples grown at different temperatures.

On the SEM images, the area marked with a square represents the interaction area of the beam with the sample, from which the approximate composition displayed on

---

the spectrum was obtained. This is a consequence of the limitations of the equipment such the beam size and lack of spot analysis. The EDS spectra obtained from the sample does indicate a considerable amount of oxygen presence in all the samples which can be attributed to the atmospheric oxygen remnant inside the tube and also as an impurity of the argon carrier gas used.

As observed in figure 3.8 (a), the sample grown at the highest temperature (1200 °C) does not exhibit any growth of fibre-like Si nanostructures. However, the EDS spectrum of the grain-like structures in figure 3.8 (a) does indicate small amounts of Si relative to the higher Ni and O content. The presence of small amounts of Si in the structures shows that there was formation of Ni-Si eutectic alloy droplets at the eutectic temperature [3.18], which upon supersaturating with Si, grow fibre-like structures.



The lack of growth of such structures even in the presence of Si vapour can be attributed to the vaporization of the droplets at sufficiently high temperatures above 1100 °C and the dissociation of the  $\text{SiO}_x$  resulting in no growth of fibre-like nanostructures as it was also observed by Song *et al* [3.19].

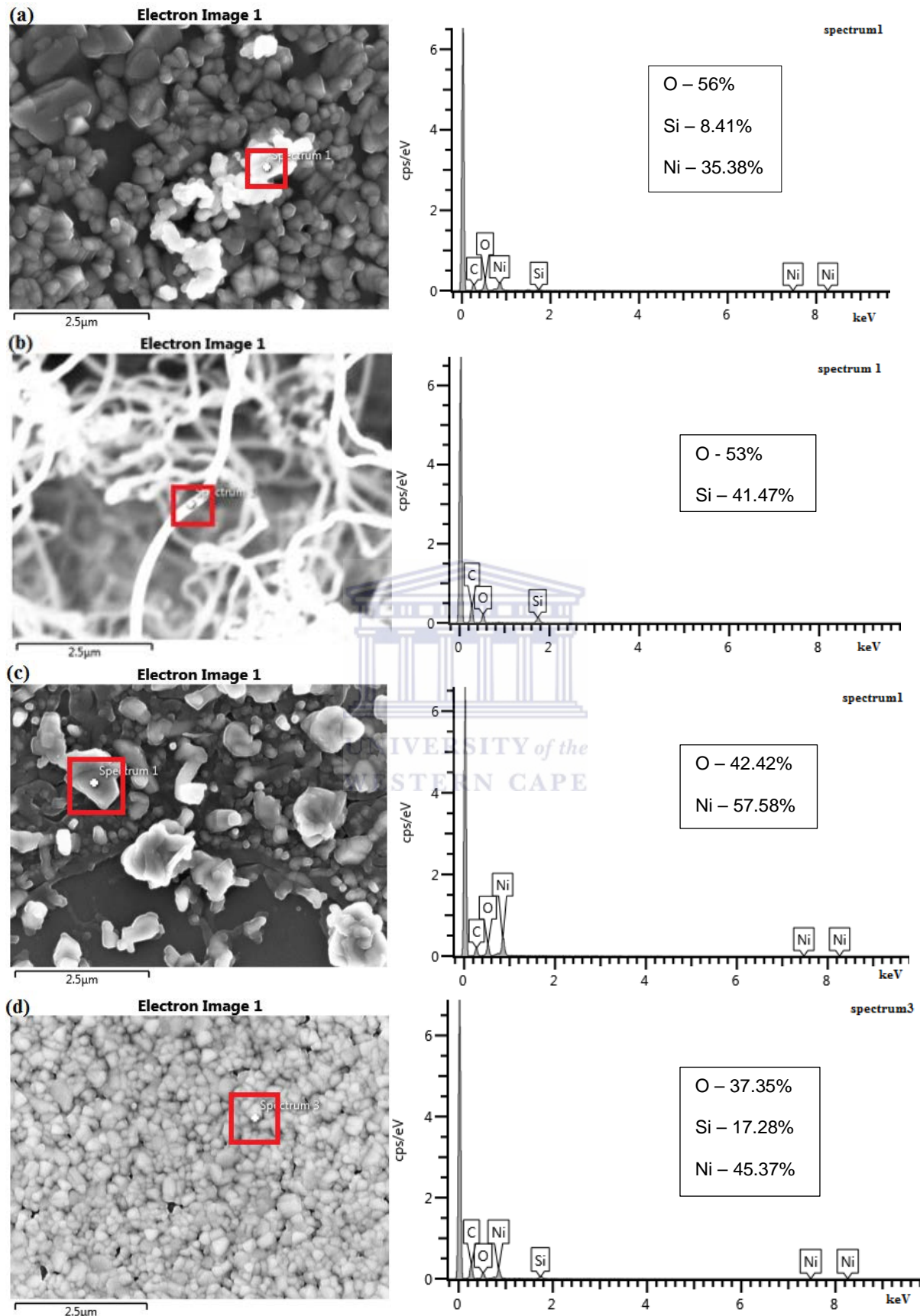


**Figure 3.8:** SEM images and EDS spectra of the various structures grown at (a) 1200 °C (b) 1000 °C (c) 900 °C (d) 800 °C

At 1000 °C, figure 3.6 (b), we observe the growth of densely packed and long SiO<sub>x</sub> nanofibres as indicated by the approximate chemical composition of the structures. The observed growth of nanofibres can be attributed to the growth temperature being within the Ni-Si eutectic alloy temperature range [3.18]. At this temperature, the Ni-Si eutectic alloy does not vaporize after supersaturating with Si but grows into SiO<sub>x</sub> nanofibre structures. In figure 3.6 (d) and (c), we observe that the growth temperatures of 900 °C and 800 °C respectively, are below the Ni-Si eutectic alloy temperature range and this can be used to explain the lack of growth of Si nanofibre structures at such lower temperatures.

### ***3.3.2.3 Fourier transform infrared spectroscopy of Si nanostructures***

In order to understand the effect of the growth temperature on the Infra-Red (IR) absorption properties of the different silicon nanostructures obtained, it is necessary to study the vibrational modes of the Si-O bonds of the silicon nanostructures grown. FTIR spectroscopy is a very quick and effective analytical technique that is used to identify the functional groups present in a molecule and also ascertain the purity of a compound through detecting any impurities based on the absorption bands obtained from the FTIR spectrum, as shown in figure 3.9. [3.20]. Based on the SEM and EDS results presented previously, FTIR analysis of the samples was carried out in order to establish the link between the morphology and the chemical composition of the grown structures.

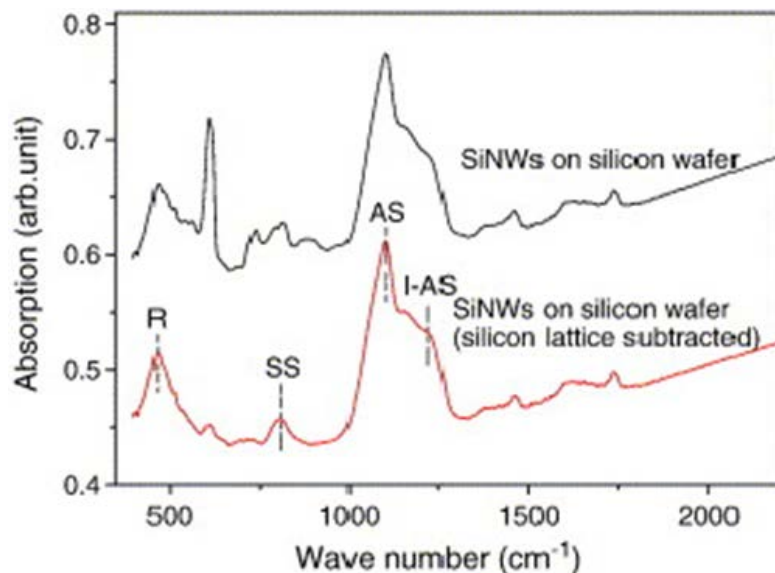


**Figure 3.9:** Typical TO bands of FTIR absorption spectra of SiNWs [3.20].

The FTIR spectra presented in figure 3.9, shows the three major transverse optical (TO) absorption bands of oxidised SiNWs within the  $400 - 1500\text{ cm}^{-1}$  range which can be classified according to the specific vibrational modes of the oxygen (O) atoms and silicon (Si) atoms which they bridge. According to Hu et al. [3.21], the lowest frequency TO band centred at around  $460\text{ cm}^{-1}$  is characterized by the Si-O-Si rocking vibrational mode while the middle frequency TO band centred around  $808\text{ cm}^{-1}$  is due to the O-Si-O symmetric stretching (SS) mode. The high frequency TO band ranging from about  $1000-1300\text{ cm}^{-1}$  and centred around  $1085\text{ cm}^{-1}$  can be attributed to the Si-O-Si asymmetric stretching (AS) mode and forms the strongest and widest absorption peak. This wider absorption band is composed of two modes; (i) the asymmetric stretching mode where by adjacent O atoms asymmetrically stretch in-phase ( $\text{AS}_1$ ), (ii) the adjacent O atoms asymmetrically stretch  $180^\circ$  out of phase ( $\text{AS}_2$ ) with each other [3.22, 3.23].

Furthermore, the relative peak area and intensity of the absorption bands in each sample indicate the relative distribution of each stretching mode and hence the dominant constituent mode in each absorption band can be identified [3.20]. The 1200 °C sample exhibited the highest intensity absorption bands followed by the 1000 °C sample while sample grown at 800 °C yielded the lowest intensity amongst the four samples hence it was not analysed further.

The FTIR absorption spectra of the different Si nanostructures grown at different temperatures ranging from 1200 - 900 °C are shown in figure 3.10 with their characteristic absorption bands. The sample grown at highest temperature (1200 °C) shows, a TO resonance, Si-O-Si rocking vibrational mode centred around  $459\text{ cm}^{-1}$ , O-Si-O symmetric stretching mode centred at  $805\text{ cm}^{-1}$  and the O-Si-O asymmetric stretching mode at  $1085\text{ cm}^{-1}$  with a shoulder peak on the higher frequency side. A similar trend is observed for the 1000 °C sample which has wire-like Si nanofibres whereby, the TO Si-O-Si rocking vibrational mode is centred at  $462\text{ cm}^{-1}$ , the O-Si-O bending mode shifted to  $812\text{ cm}^{-1}$  and the Si-O asymmetric stretching mode at  $1082\text{ cm}^{-1}$ . For the sample grown at 900 °C, there is relatively very weak absorbance displayed by, the red-shifted TO Si-O-Si vibration mode at  $450\text{ cm}^{-1}$  and the O-Si-O asymmetric stretching mode at  $1080\text{ cm}^{-1}$ . Contrastingly, in figure 3.11, the 800 °C sample displayed the least absorption intensity with one absorption band being the O-Si-O asymmetric stretching mode centred around  $1060\text{ cm}^{-1}$  which confirms the absence of nanostructures and no further information could be obtained from the spectrum.

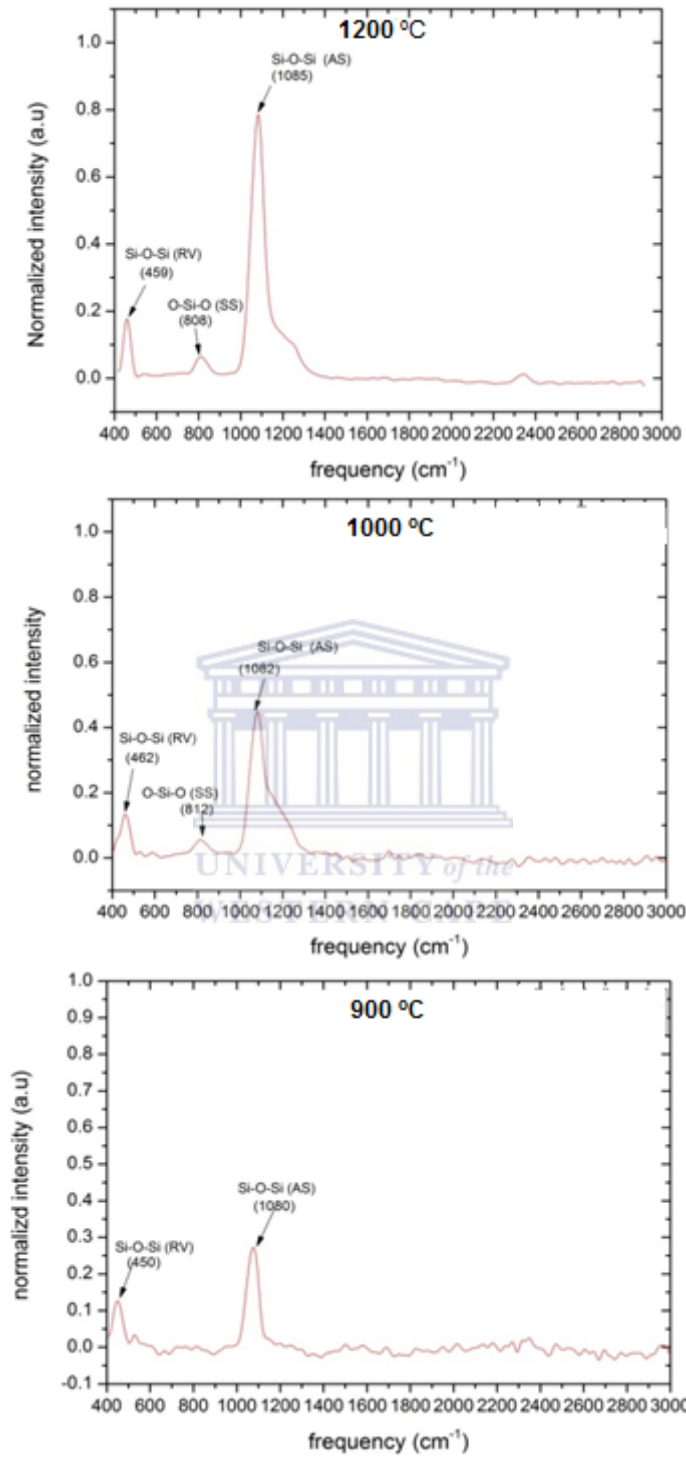


**Figure 3.10:** FTIR absorbance spectrum of Si nanofibres grown at temperatures of; 1200 °C, 1000 °C and 900 °C.

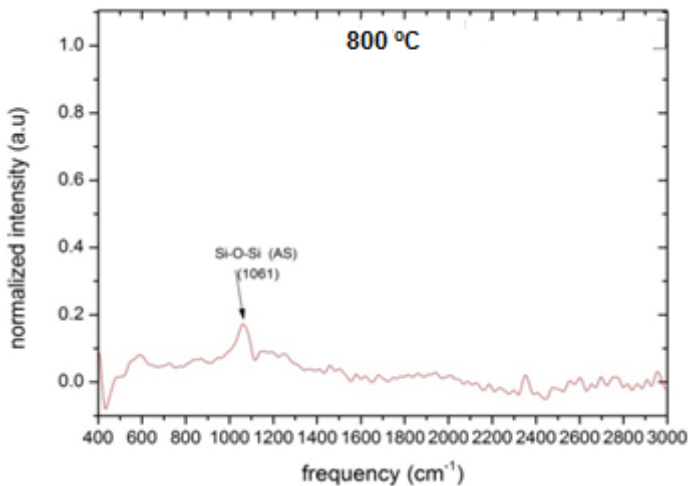


**Figure 3.11:** FTIR absorbance spectrum of Si nanofibres grown at 800 °C.

Meaningful FTIR analysis requires the decomposition of complex absorption bands of interest into individual separate bands that contain structural information about the material, as shown in figure 3.12. During this process, smoothing of the spectrum was carried out using the fast Fourier transform (FFT) and the second derivative procedure to fit the hidden bands [3.24]. The Gaussian function was used for the decomposition with a correlation coefficient of about 0.998 within the range of about 1000 - 1300  $\text{cm}^{-1}$ .

For the 1200 °C sample , the strong absorption band at 1085  $\text{cm}^{-1}$  was decomposed into three bands centred around 1080  $\text{cm}^{-1}$ , 1166  $\text{cm}^{-1}$ , 1225  $\text{cm}^{-1}$ . This strong band at 1080  $\text{cm}^{-1}$  can be attributed to the Si-O-Si TO ( $\text{AS}_1$ ) mode (TO1), while the peak around 1166  $\text{cm}^{-1}$  is due to the longitudinal optical (LO) Si-O-Si ( $\text{AS}_2$ ) mode (LO2) and a TO Si-O-Si ( $\text{AS}_2$ ) mode (TO2) around 1225  $\text{cm}^{-1}$  [3.21, 3.25].

On the 1000 °C sample the strong band was decomposed into four bands; (i) TO Si-O-Si ( $\text{AS}_1$ ) mode (TO1) at 1079  $\text{cm}^{-1}$  (ii) LO Si-O-Si ( $\text{AS}_1$ ) mode (LO1) at 1141  $\text{cm}^{-1}$  (iii) LO Si-O-Si ( $\text{AS}_2$ ) mode (LO2) at 1163  $\text{cm}^{-1}$  and (iv) TO Si-O-Si ( $\text{AS}_2$ ) mode (TO2) at 1204  $\text{cm}^{-1}$  [3.21, 3.25].

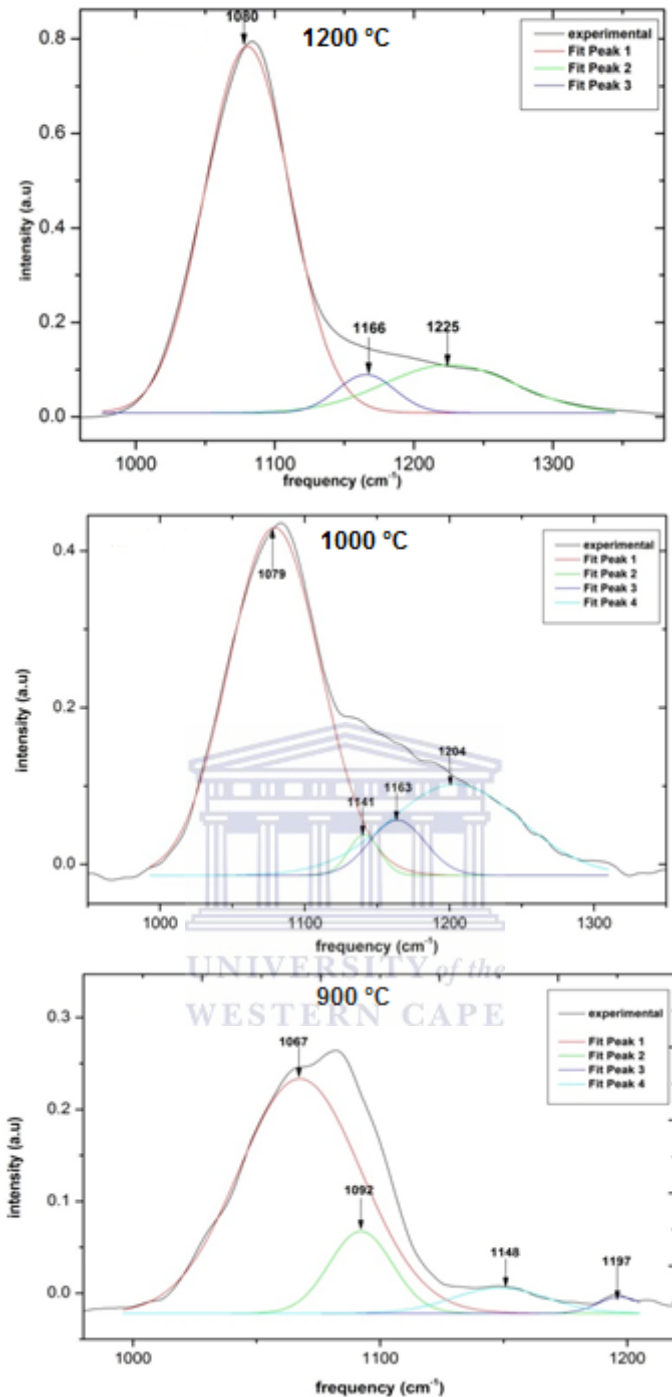


**Figure 3.12:** shows the deconvoluted absorption bands of the samples into four Gaussian peaks centred around  $1070 \text{ cm}^{-1}$ ,  $1130 \text{ cm}^{-1}$ ,  $1160 \text{ cm}^{-1}$ ,  $1200 \text{ cm}^{-1}$ .

On the sample grown at  $900 \text{ }^{\circ}\text{C}$ , the decomposed peaks were relatively of very low intensity. The TO1 mode was red-shifted to about  $1069 \text{ cm}^{-1}$ , while the higher frequency LO1 shoulder peak was also red-shifted to about  $1090 \text{ cm}^{-1}$ .

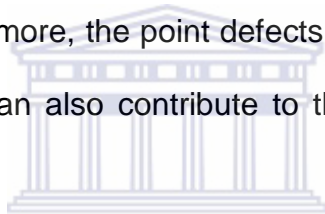
A summary of the deconvolution results is presented in table 3.3 where by the relative peak area of each absorption band is shown and is directly proportional to the prevalence of that stretching mode in the absorption band. These results, further establish the influence of the Si-O bond stretching on the shape and intensity of the absorption bands of these samples.

**Table 3.2:** Shows the relative distribution of each stretching mode within the 1000-1300 cm<sup>-1</sup> range in terms of peak area.

T <sub>substrate</sub> (°C)	1070 (cm <sup>-1</sup> )	1130 (cm <sup>-1</sup> )	1160 (cm <sup>-1</sup> )	1200 (cm <sup>-1</sup> )
1200	59.81	0	4.19	11.90
1000	35.24	1.34	3.40	13.11
900	15.83	2.85	1.31	0.39
800	3.43	0	0	0

As presented in table 3.2, the 1200 °C sample showed the strongest TO1 absorption mode at 1080 cm<sup>-1</sup>, indicating the dominance of the TO1 mode on the grown Si nanostructures. Furthermore, this can be linked to the high oxygen content as a result high thermal oxidation due to the high growth temperature [3.26]. In his work, Bashounti *et al.* indicated that backbond oxidation is the main mechanism responsible for the formation of Si-O-Si bonds in both planar and fibre-like samples. Furthermore, the absence of the LO1 absorption mode at 1130 cm<sup>-1</sup> on this sample is in agreement with observations made by Hu et al. confirming that the morphology of the grown structures is not wire/fibre structures like those on the 1000 °C sample since this mode was only observed for SiNWs and not on bulk or thin film samples [3.21].

On the contrary, sample grown at 1000 °C showed a lower intensity than the 1200 °C sample for the TO1 vibration mode which may be as a result of self-limiting oxidation that occurs on wire-like structures due to the geometry and compressive surface stress associated with Si/SiO<sub>2</sub> interfaces. On wire-like structures, the oxidation begins on the surface at oxidation sites forming a layer which later acts as a barrier preventing further and radially inward oxidation hence the lower intensity [3.26]. Hu *et al* [3.21], observed that the crystalline core of SiO<sub>2</sub>/Si nanowires might have an influence on the Si-O vibration of the interface or outer SiO<sub>2</sub> shell by increasing the energy gap between ground and excited state. This effect would result in the stronger absorption band (1200 cm<sup>-1</sup>) of nanowires being at a higher frequency as shown in table 3.2. Furthermore, the point defects such as vacancies and broken Si-O bonds at the interface can also contribute to the enhanced higher frequency absorption.



A similarity on the higher frequency side of the FTIR spectra is observed, whereby the LO2 and TO2 modes around 1160 cm<sup>-1</sup> and 1200 cm<sup>-1</sup> respectively, are observed as shoulder peaks. This trend is observed on both the 1200 and 1000 °C samples as a result of the nano-scale size effect of the nanostructures grown. This is due to the high surface tension of nanoparticles and nanowires which results in the distortion and shortening of the Si-O bond length. This in agreement with observations made by Gaskell *et al.* [3.27], whereby he observed that a high degree of structural disorder in amorphous SiO<sub>2</sub> led to an enhanced intensity of the high frequency side of the stretching mode.

The deconvolution of the FTIR absorption spectra of sample grown at 900 °C is in agreement with the observations made from the SEM analysis whereby there was no growth of Si nanostructures. On this sample, the TO1 vibrational mode was red-

shifted to about  $1067\text{ cm}^{-1}$  and  $1060\text{ cm}^{-1}$  respectively. Contrary to the observations made on the  $1200$  and  $1000\text{ }^{\circ}\text{C}$  samples, these TO1 absorption bands are relatively of very low integrated peak area (intensity) and this can be attributed to the relatively lower growth temperature which resulted in less oxidation hence hindering the formation of Si-O bonds. Furthermore, the lack of growth of Si nanostructures can be attributed to the metal catalyst nano-droplet failing to attain the required Si solubility levels which will lead to the supersaturation and consequently, the precipitation Si nanostructures [3.28]. As a result of the lack of Si nanostructures, there is no significant higher frequency absorption bands observed on this sample.

### **3.3.2.4 X-ray diffraction (XRD) of Si nanostructures**

To investigate the effect of the different growth temperatures on the internal structure of the grown nanostructures, X-ray diffraction (XRD) was used. This technique was used to determine the structural properties of the grown Si nanostructures such as crystallinity and further establish the different nickel silicide ( $\text{Ni}_x\text{Si}_x$ ) phases present in the grown structures. From a XRD pattern, the intensity of the diffraction peak can be analysed to obtain qualitative information while the crystallite size can be calculated from the width of the diffraction peak. In figure 3.13, a typical XRD pattern of a polycrystalline Si material is shown, with all the observable diffraction peaks in within the range  $10 - 110^{\circ}$  (2theta).

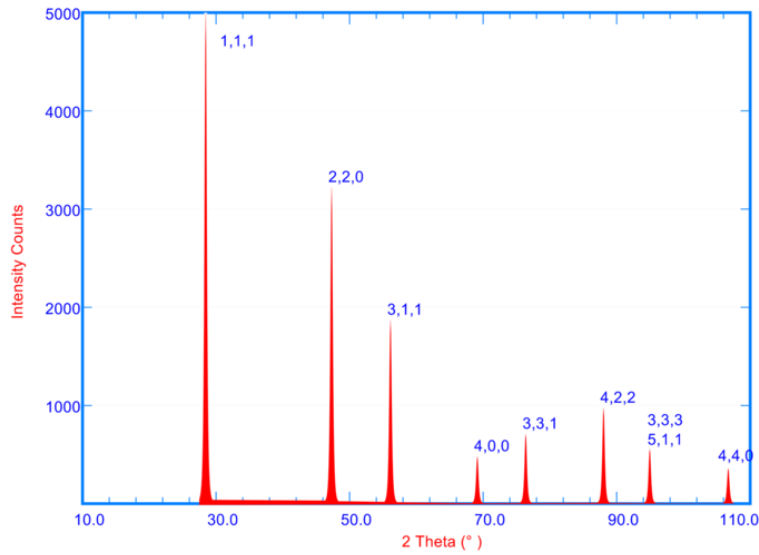


**Figure 3.13:** Typical XRD pattern showing the corresponding crystalline planes for polycrystalline Si [3.29].

The XRD pattern of the bare Si (100) substrate obtained during the analysis is presented in figure 3.14 (a) where it shows the dominant Si (400) peak at about 69° which shows the insignificance of any other orientations present in the substrate. In figure 3.14 (b), a zoom-in onto the XRD pattern shows the typical strong (400) peak at around 69° while the Si (200) and (220) peaks are located around 33° and 47° respectively. By the extinction rule, the Si (200) peak is forbidden hence it appears as a weak peak compared to (400) [3.29]. Furthermore, the (331) and (442) XRD peaks are located at about 76° and 89° respectively.

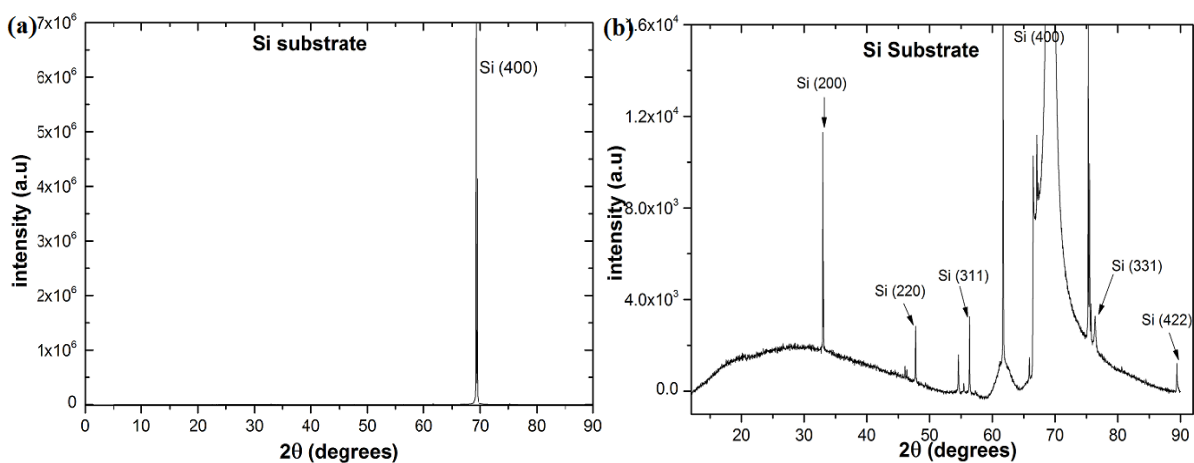


**Figure 3.14:** XRD pattern of a bare (100) Si substrate showing; (a) very high intensity Si (400) peak and in (b) zoomed-in XRD pattern to reveal more hidden peaks.

The presence of diffraction peaks that are not part of the (100) family of planes, is an indication that the (100) Si wafer used as a substrate may have not been purely single crystalline.

Furthermore, investigation of the XRD pattern of this bare wafer reveals peaks that could not be indexed accordingly with known and allowed h,k,l values for Si and this major drawback can be attributed to the limitations of X-Ray Powder Diffractometry (XRPD) such as the relatively low linear range for detection ( $\sim 8 \times 10^4$  cps). This nonlinear response of the detector when measuring high intensity peaks may result in sharp and random spikes (Bragg peaks) on the XRD pattern making the results inaccurate. Furthermore, at high photon flux counts, the photon energy resolution-based electronic monochromization fails. Consequently, the unindexed Bragg peaks observed at  $2\theta \approx 46^\circ, 54^\circ, 61^\circ, 75^\circ$  can be attributed to such limitations since they result from reflections from the (400) crystallographic planes of Si and each peak represents unfiltered unique wavelengths (Kβ, La, etc) from the characteristic spectrum of the X-ray tube used in the measurement [3.30].

The XRD patterns of the as-grown Si nanostructures grown at the different temperatures with a 200 °C variation are also presented in figure 3.15 in the range of 0 to 90° ( $2\theta$ ). The sample grown at 800 °C shows a broad peak stretching from about  $2\theta \approx 15 - 30^\circ$  and this peak can be attributed to the amorphous nature of the oxidised Silicon ( $\text{SiO}_2$ ) structures grown on the samples as observed previously from SEM results. Furthermore, two peaks located at about  $2\theta \approx 37^\circ, 43^\circ$  corresponding to NiSi (111) and NiSi (210) respectively, can be observed on the XRD pattern and are unique to the sample since they are not present on the substrate.

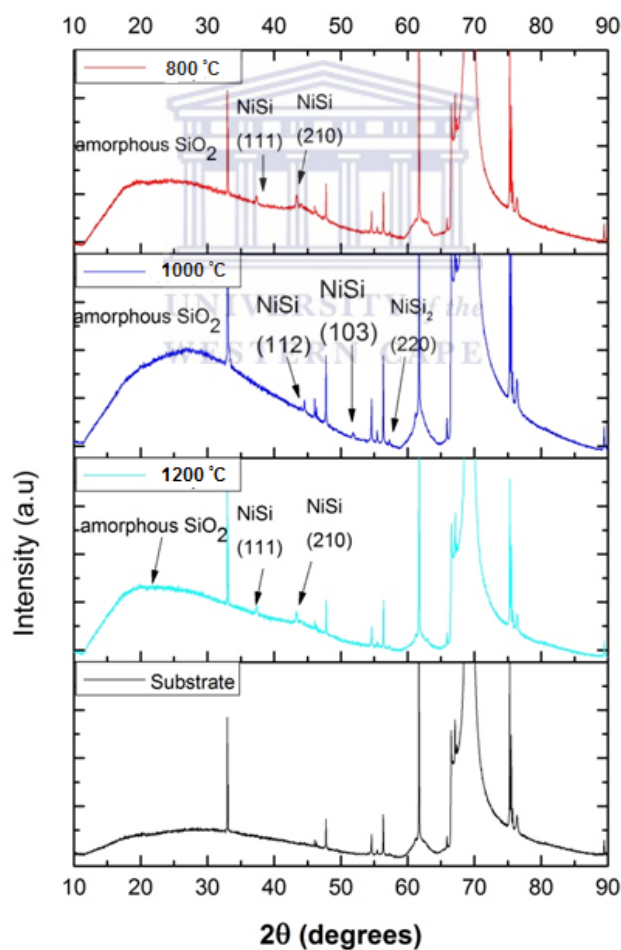


**Figure 3.15:** XRD patterns of a bare Si (100) substrate and Si nanostructures grown at different temperatures; 1200 °C, 1000 °C and 900 °C.

These peaks are due to the different nickel-silicide phases observed as the Ni thin film reacts with the c-Si wafer when subjected to higher temperatures (800 °C). This phenomenon occurs as a result of the Ni/Si not being in thermodynamic equilibrium and in the process of heating, several intermediate silicides form until thermodynamic equilibrium is achieved with silicide/Si at the suitable temperature [3.31]. As a consequence of the 800 °C growth temperature, the only silicide phase observed is the NiSi phase. This is due to the high diffusion coefficient and high thermal mobility of the metal (Ni) compared to Si, the Ni-rich silicide phases form at lower temperatures and the Si-rich phases form at sufficiently high temperatures above 800 °C [3.29, 3.31].

On 1000 °C sample, there are two NiSi phase diffraction peaks observed at  $\approx 45^\circ$  (NiSi (112)) and at  $\approx 52^\circ$  (NiSi (103)). Furthermore, there is a weak peak at  $\approx 57^\circ$  which can be attributed to the Si-rich,  $\text{NiSi}_2$  phase. Even at this high temperature, strained grains of the NiSi phase are still observable and due to their melting point being around 990 °C, morphological degradation through grain boundary grooving and agglomeration of the NiSi film occurs, transforming the NiSi into  $\text{NiSi}_2$ . In the midst of excess Si, the sudden appearance of this thermodynamically stable  $\text{NiSi}_2$  phase at such temperatures can also be explained based on the Ni-Si binary phase diagram [3.32] which indicates transformations of NiSi to  $\text{NiSi}_2$  at temperatures above 800 °C indicating a nucleation controlled formation [3.33, 3.34] whereby NiSi reacts with Si to produce  $\text{NiSi}_2$ .

The XRD pattern of the 1200 °C sample is presented in figure 3.15 and is overlayed on the XRD pattern of a bare Si wafer used as a substrate which then enables us to observe the peaks which are specifically due to the sample only and not the substrate. On this sample, an amorphous  $\text{SiO}_2$  characteristic broad peak stretching

---

from about  $2\theta \approx 15^\circ - 30^\circ$  is observed and is of a lower intensity compared to that of the 1000 °C sample. Furthermore, two NiSi phases are observed as, (111) and (210) at 37° and 43° respectively.

It is interesting to notice the absence/disappearance of the  $\text{NiSi}_2$  phase which was observed previously at 1000 °C which can be attributed to the reactions that occur at the Ni-Si eutectic temperature [3.33]. This behaviour can also be explained from the Ni-Si binary phase diagram which clearly shows that, only the NiSi phases exist at such high temperatures [3.32].

During the XRD analysis of all the samples grown at different temperatures, it was observed that there were no new Si diffraction peaks observed. This indicates that the grown structures were either amorphous or crystalline and having the same orientation as the Si (100) substrate. This observation necessitates the need to employ further characterisation techniques such as transmission electron microscopy to ascertain crystallinity of the grown Si nanowires.

### **3.3.3 Effect of Source-to-Substrate Position on Si Nanofibre Growth**

Generally, it is known that one of the most crucial parameters during thermal chemical vapour deposition (TCVD) is the precursor reaction zone length which is determined by the distance between the substrate and the source material. Hassan et al [3.35], demonstrated the influence of substrate position on the morphology and chemical composition of ZnO nanowires grown at different substrate positions using TCVD [3.35, 3.18]. Therefore, in this section, the effect of the substrate position to source material on the morphology and composition of Si nanofibres shall be investigated. The choice of the other optimal growth parameters such as; Ni catalyst

and growth temperature, were informed by the studies conducted previously (subsection 3.3.1 and 3.3.2).

### **3.3.3.1 Scanning electron microscopy results**

In order to study the morphological effects of the substrate distance from the source, scanning electron microscopy was used and the SEM micrographs of the different morphologies are presented in figure 3.16 for samples deposited at source-to-substrate distances ( $d_{s-s}$ ) of 5, 7 and 11 cm . These overview SEM micrographs presented in figure 3.16 show no growth of nano structures on the sample grown closest the source at 5 cm. Si nanofibre- like structures were observed to have been grown on the two other samples whereby the sample at 11 cm showed a homogeneously dense packing of the fibre-like Si nanostructures.

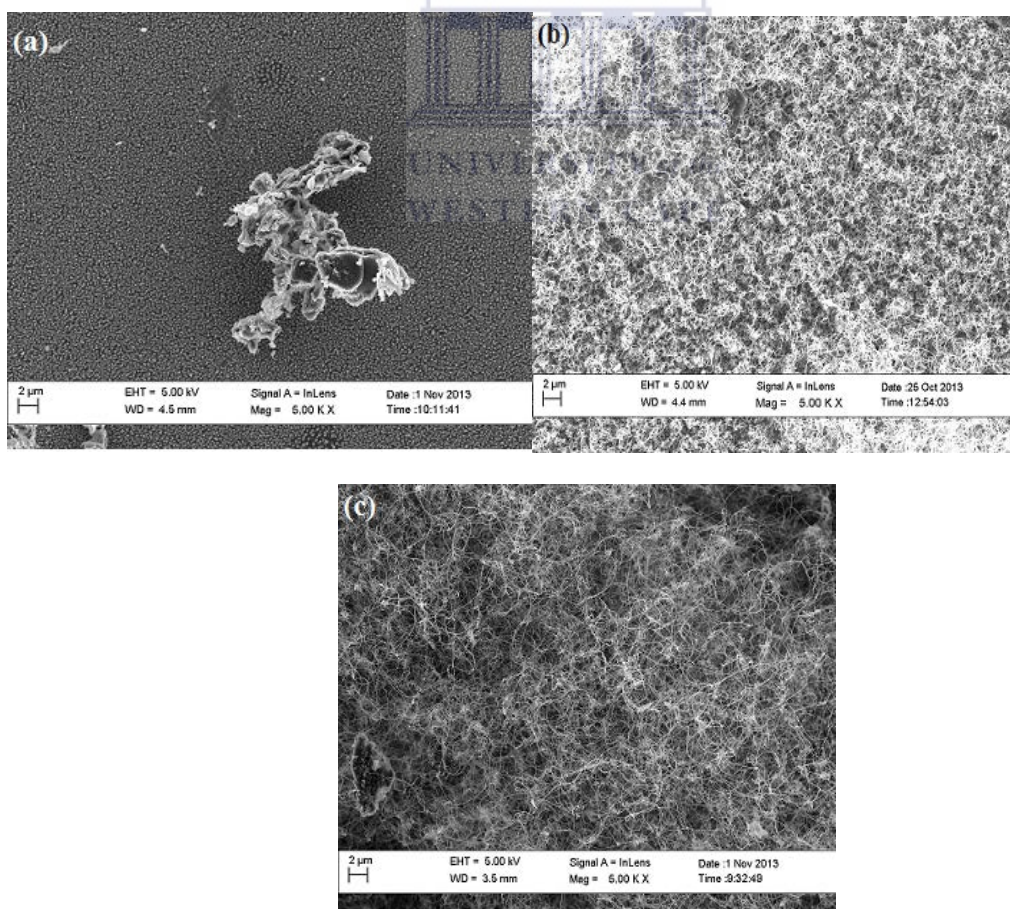


**Figure 3.16:** Overview SEM images corresponding to samples of Si nanostructures grown at different  $d_{s-s}$ ; (a) 5 cm (b) 11 cm (c) 17 cm.

Moreover, it is interesting to observe that the sample furthest from the source at 17 cm showed a less dense packed growth of structures as shown in the figure. For qualitative analysis, the SEM micrographs of the samples taken at higher magnification were used, which reveal more information on the different morphologies of the Si nanostructures obtained at the different substrate positions.

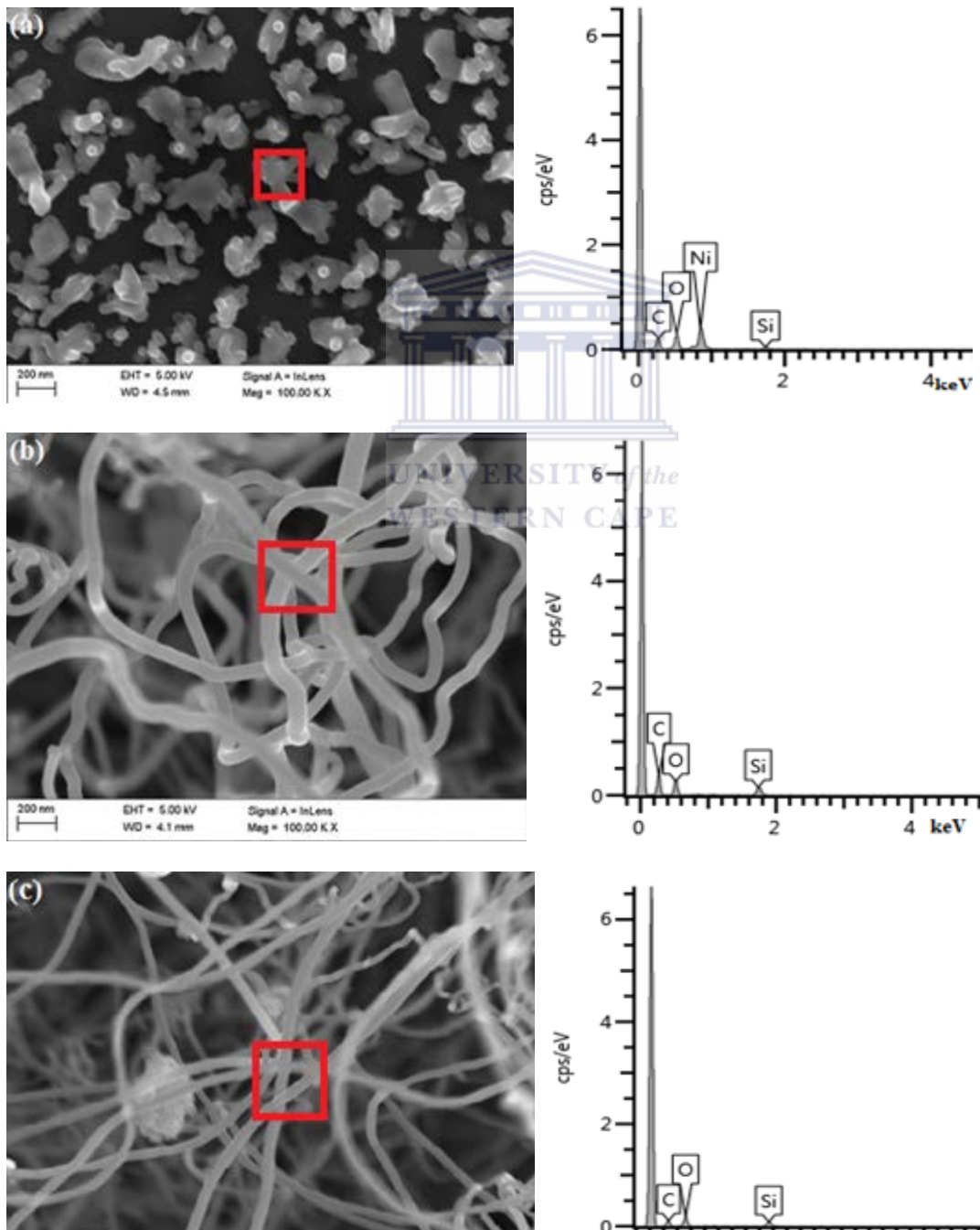


**Figure 3.17:** SEM micrographs and corresponding EDS spectra for (a) sample 1 (b) sample 2 (c) sample 3.

Figure 3.17 presents the higher magnification SEM micrographs of the Si nanostructures and corresponding EDS spectrum for each sample obtained from an approximate area represented by the marked area on the sample. It is evident from the higher magnification micrographs that, at the closest position to the source (5 cm), there was no growth of fibre-like nanostructures except the formation of irregularly shaped structures with thick finger-like projections, nonhomogeneous throughout the sample. The EDS measurements conducted on these grown structures, shows presence of Ni, Si and O. The presence of Ni indicates that the metal catalyst was not used up during the VLS mechanism as a result of the Si vapours not being adsorbed on the surface of the Ni-Si eutectic alloy during the growth. This suggests that the distance between the substrate and source was not adequate [3.35] to promote Si-Si reactions among the evaporated atoms to form the ideal  $\text{Si}_x$  precursor for easy adsorption on the surface of eutectic alloy droplet responsible for the growth of Si wire-like nanostructures.

Moving further away from the source to about 11 cm and 17 cm, yielded good samples with the most growth of Si nanostructures as shown in figure 3.16 (b). For the sample at 11 cm, the SEM micrographs reveal a densely packed growth of oxygen-rich, Si fibre-like nanostructures as it is confirmed by EDS results. However, as much as the sample at 17 cm also had growth, it is interesting to note that those structures were not closely packed as those on 11 cm sample. Furthermore, sample grown at 17 cm had well defined structures that appeared to be generally thinner in diameter and extending over great lengths with less kinks and bends compared to the sample grown at 11 cm. Such variations in morphology of the structures obtained at different locations, is an indication of the source-to-substrate distance influence.

In order to understand the role of the source-to-substrate distance, it is crucial to understand the growth mechanism of the nanostructures and the kinematics involved in precursor transportation from source to substrate position [3.35, 3.36]. During thermal evaporation of Si powder, micron sized Si/SiO<sub>2</sub> particles are ejected or sublimated together with residual gases into the atmosphere and are much heavier than the Ar carrier gas atoms [3.37]. During this migration, from the source to the deposition site, these evaporates undergo several collisions in the order of about 4.8 x 10<sup>4</sup> times which in turn attenuates the momentum hence making the evaporated more susceptible to deposition [3.36]. The lack of growth on the sample at 5 cm from source can be attributed to the high momentum of the evaporated atoms blowing past the Si-rich eutectic alloy droplets responsible for seeding nanofibre growth on this sample. This observation shows that the distance travelled from source to substrate is crucial because it is linked to number of collisions which annihilates the kinetic and momentum of evaporated species as observed on the sample grown at 11 cm. On this sample there is a densely packed growth of thicker diameter nanofibres which indicates an abundant supply of Si/SiO<sub>2</sub> atoms to be absorbed by the Si-rich eutectic alloy droplets. However, further downstream at about 17 cm, growth is still observed which also indicates the reduced momentum of the evaporated atoms. The thinner diameter at this position can be attributed to the reduced influx of evaporated species due to the already reduced kinetic energy from about 11 cm back [3.36].

### **3.3.3.2 Fourier transform infrared spectroscopy**

As observed previously, the precursor reaction zone length is crucial parameter during the TCVD growth of Si nanostructures, it is therefore necessary to investigate its effects on the chemical composition of the grown nanostructures. In a similar way,

FTIR spectroscopy was used to identify the vibrational modes of the Si-O bonds of the different silicon nanostructures grown at the varying substrate positions and also ascertain the purity of a compound through detecting any impurities based on the absorption bands obtained from the FTIR spectrum. Furthermore, the FTIR analysis of these samples was carried out in order to understand the link between the chemical compositions of the grown structures and the distance of the substrate from the source. The FTIR spectra of the different samples are presented in figure 3.18.

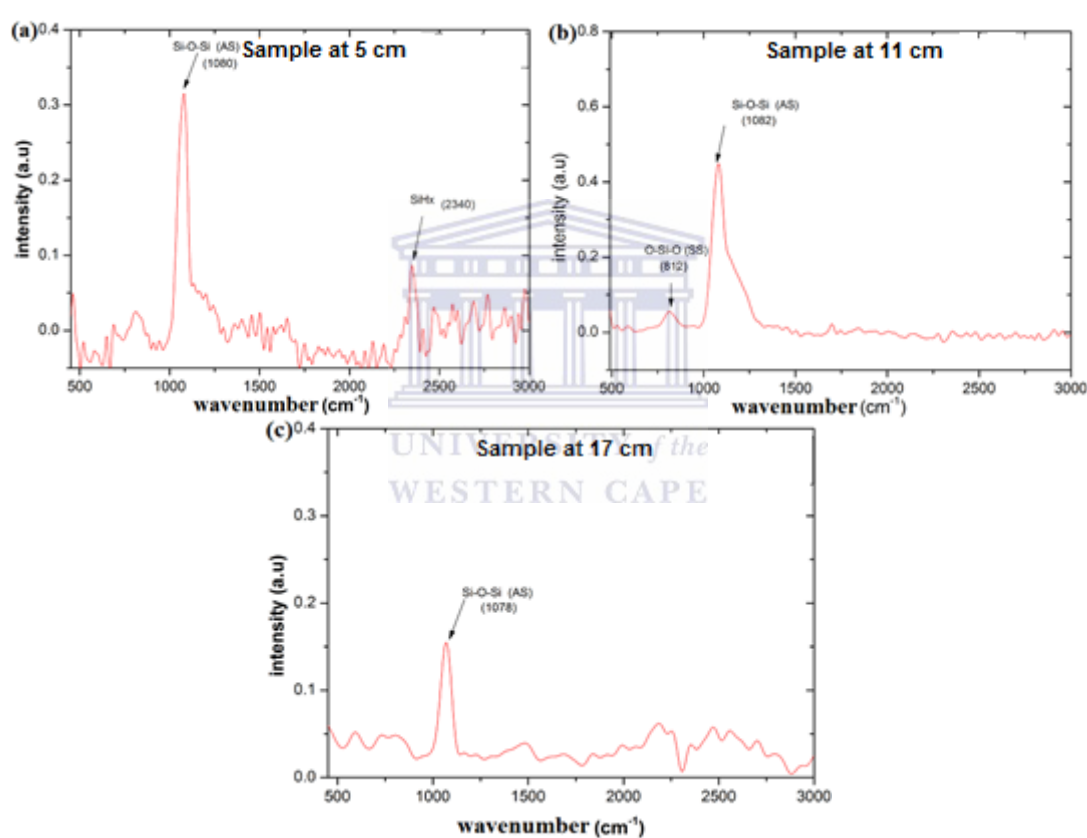
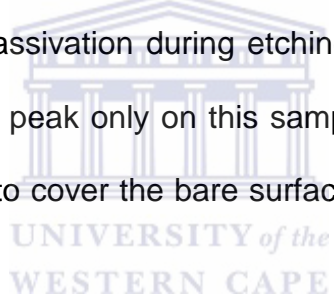


**Figure 3.18:** FTIR spectra of the all the samples grown at different distances from the source, (a) 5 cm (b) 11 cm (c) 17 cm.

The FTIR spectrum for the sample grown at the closest distance from the source (5 cm) shows an asymmetric TO Si-O-Si peak of low intensity centred around 1080 cm<sup>-1</sup> and a very weak SiH<sub>x</sub> peak at about 2340 cm<sup>-1</sup> [3.38]. As a consequence of the grown Si nanostructures, as shown by SEM, the samples grown at 11 and 17 cm displayed different absorption characteristics to those of the sample at 5 cm. For the

sample at 11 cm, the O-Si-O bending mode was shifted to  $812\text{ cm}^{-1}$  and the TO Si-O-Si asymmetric stretching mode at  $1082\text{ cm}^{-1}$  while the sample at 17 cm showed the asymmetric TO Si-O-Si stretching mode at about  $1078\text{ cm}^{-1}$ .

The observed FTIR absorption characteristics for the 5 cm sample are in full agreement with the SEM and EDS results shown in figure 3.16 (a). The TO Si-O-Si (AS) mode centred around  $1080\text{ cm}^{-1}$  can be attributed to adsorbed Si-O atoms by the Ni-Si eutectic alloy during growth. However, due to this sample being too close to the Si source, the Si-O reaction zone length was reduced leading to insufficient amounts of Si-O adsorption to support nanowire growth. Furthermore, the low intensity  $\text{SiH}_x$  peak around  $2340\text{ cm}^{-1}$  can be attributed to the Si-H bonds on the substrate which result from passivation during etching in dilute HF-acid [3.39]. The appearance of this absorption peak only on this sample therefore confirms the lack of oxidised Si nanostructures to cover the bare surface of the substrate as shown in figure 3.16 (a).



The absorption characteristics of the sample at 11 cm are characterised by a weak TO absorption band due to O-Si-O (SS) mode at  $812\text{ cm}^{-1}$  and the strongest high frequency absorption peak due to the Si-O-Si mode centred around  $1080\text{ cm}^{-1}$ . In contrast, the sample at 17 cm only exhibited the TO, Si-O-Si (SS) mode red-shifted to about  $1078\text{ cm}^{-1}$  with a low intensity compared to that of sample at 11 cm. This observation can be directly linked to the prevalence of the Si-O-Si bond configuration on the sample. This phenomenon is discussed in detail in subsection 3.2.2 (c).

### **3.3.3.3 X-Ray diffraction of Si nanostructures (fibres)**

X-ray diffraction analysis was carried out on all three samples in order to observe any influence due to substrate position on the internal structure of the grown Si

nanostructures and further ascertain any traces of crystalline structures obtained. Furthermore, this investigation will reveal any variations among the NiSi phases at each substrate position since we have observed the effect of distance travelled on the reactions and interactions of the evaporated species [3.36].

The XRD pattern of the Si (100) substrate that was used is shown in figure 3.19, whereby it shows the dominant Si (400) peak (a) and the other Si peaks in (b) which are of insignificant intensity when compared to the dominant (400) peak at  $69^0$ . These other peaks have been previously discussed in subsection 3.2.2 (d)

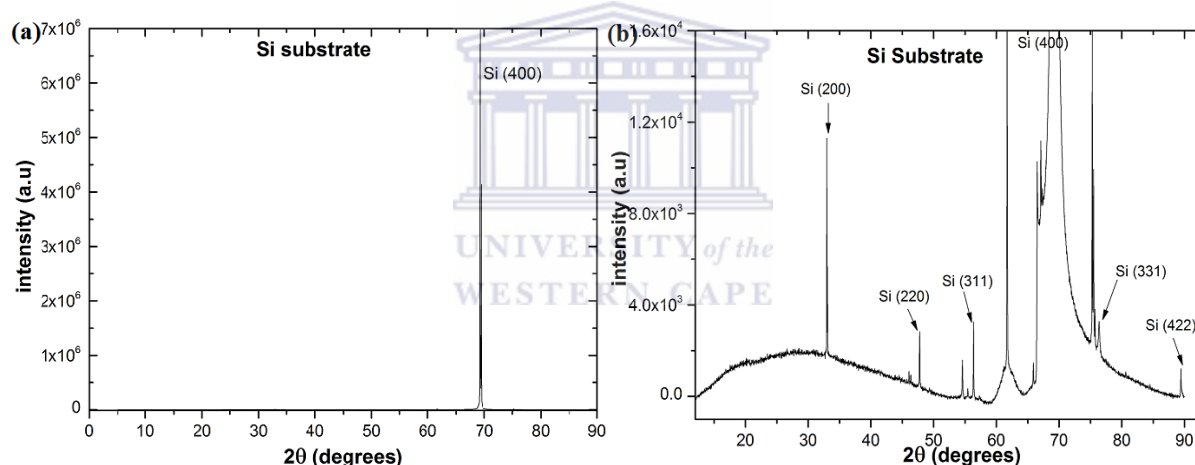


**Figure 3.19:** XRD pattern of a (100) Si substrate showing; (a) very high intensity Si (400) peak, (b) zoomed-in XRD pattern to reveal more hidden peaks.

The XRD spectra of the samples grown at 5, 11 and 17 cm from the source are presented in figure 3.20. On these spectra, only the peaks due to the sample material grown on the substrate have been indexed and discussed.

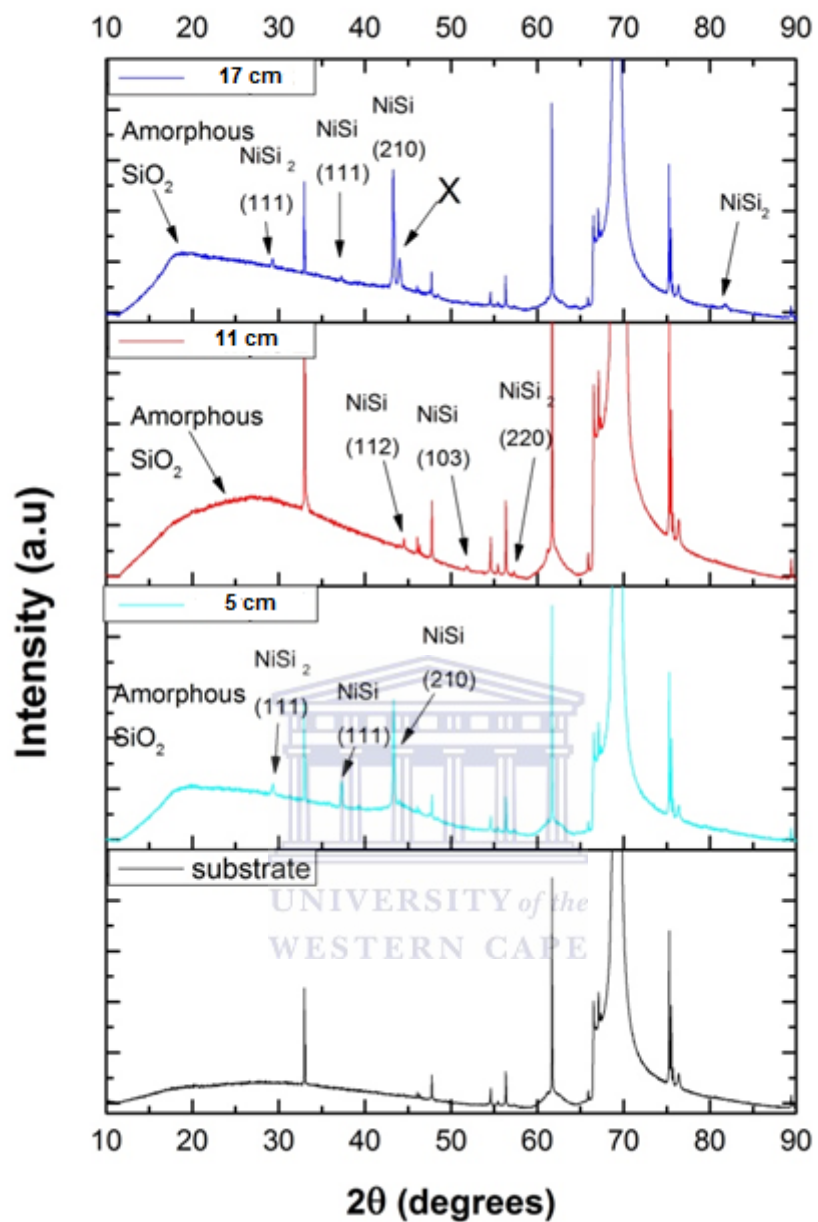


**Figure 3.20:** XRD spectra for samples grown at varying  $d_{ss}$ ; 5 cm, 11 cm and 17 cm.

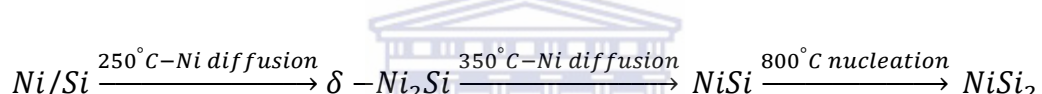
The XRD analysis results presented in figure 3.20 show the variations and structural differences between the samples. The sample at 5 cm, which was closest to the source, is characterized by a broad peak stretching from about  $2\theta \approx 15 - 30^\circ$  which is due to the growth of amorphous  $\text{SiO}_2$  on the sample. The other three peaks at  $2\theta \approx$

$29^\circ$ ,  $37^\circ$ ,  $43^\circ$  are for  $\text{NiSi}_2$  (111),  $\text{NiSi}$  (111) and  $\text{NiSi}$  (210) respectively [3.40, 3.41]. From the SEM results of this sample (figure 3.17(a)), it is evident that there were no Si nanofibres grown on the sample, however there was formation of  $\text{SiO}_2$  through thermal oxidation from remnant and oxygen from the Ar carrier gas. The formation of the different  $\text{Ni}_x\text{Si}_x$  phases has been studied extensively using *in-situ* XRD analysis to study silicidation reactions of Ni alloys [3.36-3.42]. Detarvenier et al, observed several nickel silicide phase transformations whereby, metal-rich ( $\text{Ni}_3\text{Si}$ ) silicide phases start forming at around  $300^\circ\text{C}$  followed by the  $\text{NiSi}$  phase at about  $400^\circ\text{C}$ . As the temperature rises above  $750^\circ\text{C}$ , the  $\text{NiSi}_2$  phase forms through a nucleation controlled reaction which consequently results in the disappearance of the  $\text{NiSi}$  XRD peaks which is a result of the peritectoid reaction between  $\text{NiSi}$  and Si to form the  $\text{NiSi}_2$  [3.31,3.42,3.43].

Moving further away from the source, to about 11 cm and 17 cm, different XRD spectra are observed. A very broad amorphous  $\text{SiO}_2$  peak is observed with the highest integrated intensity (area) on the sample at 11 cm, compared to that of the sample at 17 cm. This observation can be directly linked to the higher growth density of oxidised Si nanofibres on the 11 cm sample as observed in SEM results and the amorphous nature of these grown Si nanofibres-like structures can be attributed to the high oxidation rate and also the rapid metal-catalysed VLS growth mechanism [3.33]. These nanowire-like structures are likely to exhibit some quantum confinement effects which can have an influence on the nickel silicide formation within the structures [3.44]. The XRD analysis of the sample grown at 11 cm further shows two nickel monosilicide ( $\text{NiSi}$ ) phases (112) and (103) observed at  $2\theta \approx 44^\circ$  and  $52^\circ$  respectively while a low intensity  $\text{NiSi}_2$  (220) peak [3.45] is observed at  $57^\circ$ . On the sample grown at 17 cm, the nickel monosilicide phases were identified as

NiSi (111), NiSi (210) at  $2\theta \approx 37^\circ$  and  $43^\circ$  respectively [3.31]. The unidentified peak marked X at  $2\theta \approx 44^\circ$  could not be indexed but could be attributed to an unknown nickel silicide phase or impurity present on this sample. Contrary to the observations made on the sample grown at 11 cm, this sample shows two different nickel disilicide ( $\text{NiSi}_2$ ) phases, at  $2\theta \approx 29^\circ$  and  $81^\circ$  [3.43].

From these presented XRD results, it is evident that the substrate position from the source has a bearing to the internal structure of the Si nanostructures grown as illustrated by the different XRD spectra. Since there is no growth of Si nanostructures on the sample at 5 cm, the growth mechanism and phase formation of nickel silicide's is therefore analogous to that of Ni thin film silicidation [3.31], where by;



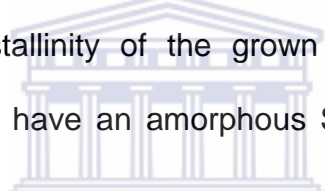
Detavernier *et al.*, in his work using *in situ* XRD analysis, observed that Ni starts reacting with Si substrate to form various metal-rich Ni silicide phases ( $\text{Ni}_2\text{Si}$ ,  $\text{Ni}_{31}\text{Si}_{12}$ ) at about  $300^\circ\text{C}$  through the diffusion of Ni into Si [3.42]. When the temperature increases to about  $400^\circ\text{C}$ , NiSi phase is formed and is followed by the  $\text{NiSi}_2$  phase at about  $800^\circ\text{C}$ . This phase is stable over a range of about  $200^\circ\text{C}$  after which the intensity of the  $\text{NiSi}_2$  peaks decreases drastically as the temperature approaches the Ni-Si eutectic point of about  $966^\circ\text{C}$  [3.45].

On the samples grown at a  $d_{ss}$  of 11 and 17 cm, the silicide phase formation sequence is different to that of thin film silicidation due to the presence of nanoscale features present on the samples. This is in agreement with observations made by Yung-Chen *et al.*, where he showed that at the nanoscale, interfacial energy differences and surface free energy have a very crucial role in silicide phase

---

formation. He demonstrated that phase formation of metal-rich silicide phase is greatly retarded in the presence of the built-in high compressive stress associated with Si/SiO<sub>x</sub> core shell and bare SiNW's [3.44]. These differences observed are an indication of the structural effects imposed by different substrate positions from the source.

The XRD analysis of all the samples grown at different source-to-substrate distances, shows that there were no new Si diffraction peaks observed. This indicates that the grown structures were either amorphous or crystalline and having the same orientation as the Si (100) substrate. This observation necessitates the need to employ further characterisation techniques such as transmission electron microscopy to ascertain crystallinity of the grown Si nanowires and determine whether the grown nanowires have an amorphous SiO<sub>x</sub> shell with a crystalline Si core.



### **3.3.4 TEM Characterization of Si-Nanostructures**

Following the extensive investigations that have been carried out in the previous sections of this chapter, a lot of crucial observations have been made with regards to the optimum growth conditions for Si-nanostructures using the TCVD system. Firstly, the ideal catalyst for seeding Si nanofibres with a high yield was found to be Ni at the expense of the more expensive Au catalyst and also non-catalyzed growth of Si nanofibres. The optimum growth temperature and substrate position were then investigated and found to be 1000°C and 11 cm from source, respectively. This best sample, grown at optimum parameters, was characterised using SEM, EDS, FTIR and XRD, giving an insight onto the morphology, chemical composition and the internal structure. However, the need to acquire more insight about the internal

structure and crystallographic information of this grown Si nanofibre sample was inevitable hence the employment of TEM technique became apparent.

TEM was performed using a Tecnai F20 on Si nanofibres samples in order to intensely examine the crystallography of the Si nanofibres, observe the Ni catalyst particle, and also investigate if the grown nanofibres are hollow or filled structures resembling nanorods or nanowires. This work was undertaken using the high-resolution bright field imaging, scanning tunnelling microscopy (STEM) and also electron energy-loss spectroscopy (EELS). To prepare the TEM samples, a scalpel was used to scrap off the nanowires from the Si substrate and directly deposited them on a copper grid that is covered with a holey carbon film and then analysed.

### **3.3.4.1 High- resolution bright field imaging of silicon nanofibres**

The TEM bright field (BF) images presented in figure 3.21 clearly shows the different morphologies of the grown Si nanofibres at different magnifications.

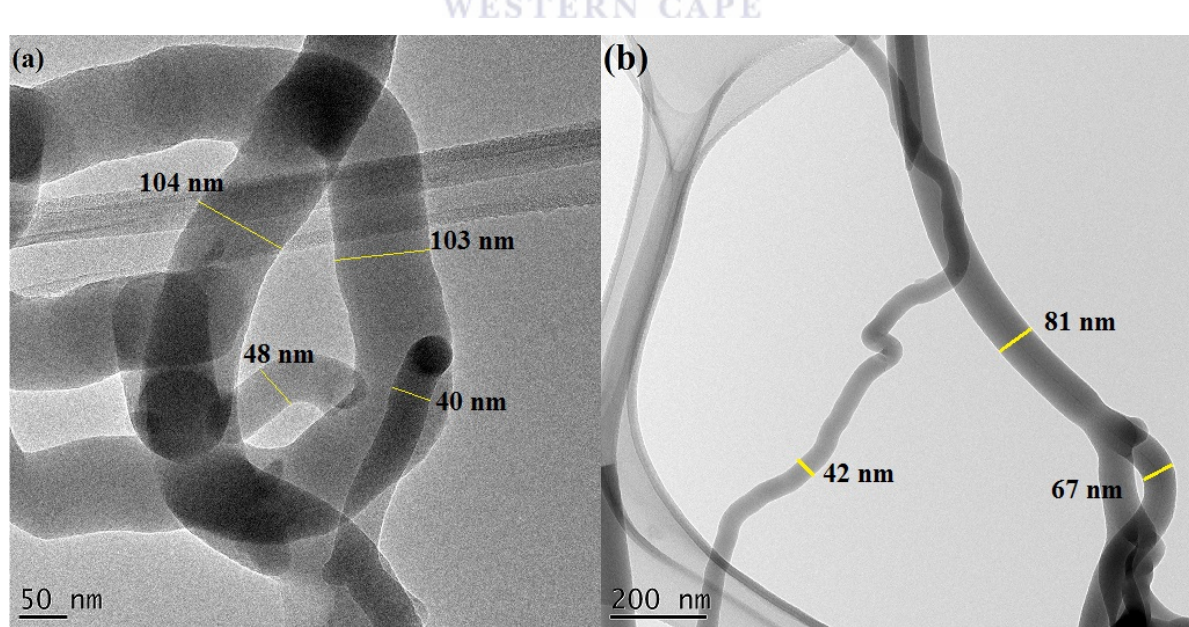


**Figure 3.21:** BF images showing the morphologies of non-uniform diameter Si nanofibres.

The TEM BF images shown in figure 3.21 clearly show the non-uniform diameters of the grown Si nanofibres which complements the SEM observations made previously.

This occurrence can be attributed to the non-uniform catalyst nano islands which act as the nucleation sites for the nanofibres during VLS growth as described in 3.3.1 [3.46, 3.47]. The VLS growth mechanism is one of the most commonly favoured growth processes for Si nanostructures since it is reliable for large area growth and utilizes simple instrumentation such as a room temperature sputter coater and tube furnace. However, as depicted in figure 3.21, one of the challenges faced in using this growth mechanism is the lack of control and precision over the nanoparticle size distribution, spacing and growth position on the substrate leading to non-uniform diameter structures [3.48].

As a result of the high resolution and high magnification TEM investigations carried out on the samples, more morphological and structural evidence which supports the VLS growth mechanism dominance during Si nanostructure growth was revealed. Figure 3.22 (a) shows the overview of an individual Si nanofibre with “smooth” edges. However, a closer inspection of the same nanofibres at higher magnification shown in figure 3.22 (b) reveals the roughness of the walls of the grown nanofibres which can be linked to rapid growth which is also associated with VLS growth mechanism.

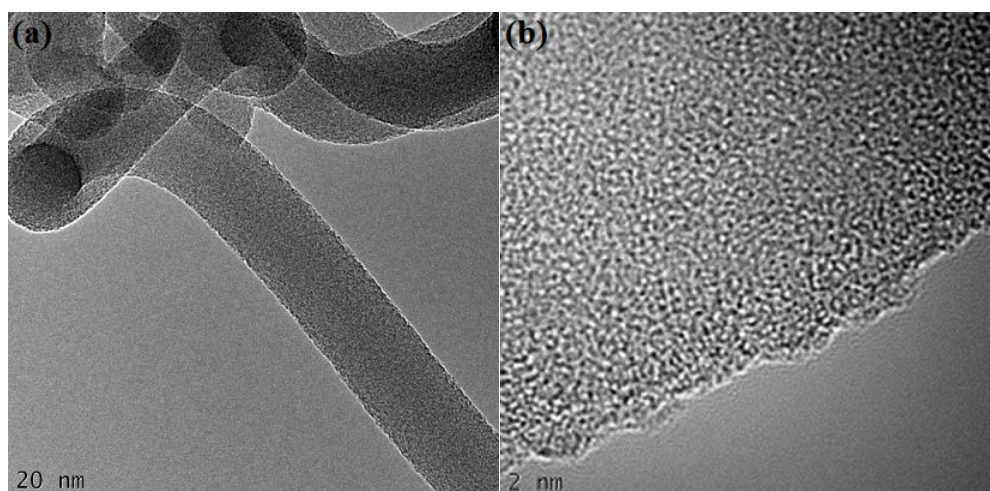
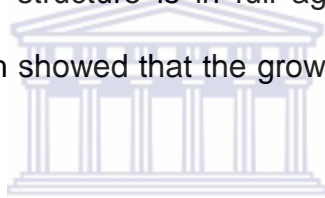


**Figure 3.22:** TEM BF images showing (a) an overview of the Si nanofibres surface, (b) a high magnification image showing the surface of the nanofibres.

Upon closer inspection, the sample in figure 3.22 (b) shows no presence of observable fringes along and across the body of the Si nanofibres. This observation indicates that the grown Si nanofibres are of amorphous nature [3.47]. This further shows that the grown Si nanofibres do not have a crystalline Si core sheathed in an amorphous  $\text{SiO}_x$  shell, forming a core-shell structure.

Pignalosa *et al* in his work succeeded in synthesizing crystalline core-shell Si nanowires which displayed very good antireflection properties even at wide angles of incidence and have huge applications in large area photovoltaics [3.49]. However, the absence of the core-shell structure is in full agreement with the XRD results obtained in section 3.3.2 which showed that the grown Si nanofibres are amorphous in nature.



The information about morphology and internal structure of the grown Si nanofibres is very crucial for understanding the growth process of Si nanofibres which in turn enables the optimization of Si nanofibre growth for specific applications. Figure 3.23 (a) shows some randomly oriented Si nanofibres which are broken structures due to extraction method used. However, this overview clearly shows that some the nanofibres are terminated by spherical tips and a high magnification image of the nanofibre tip is shown in (b).

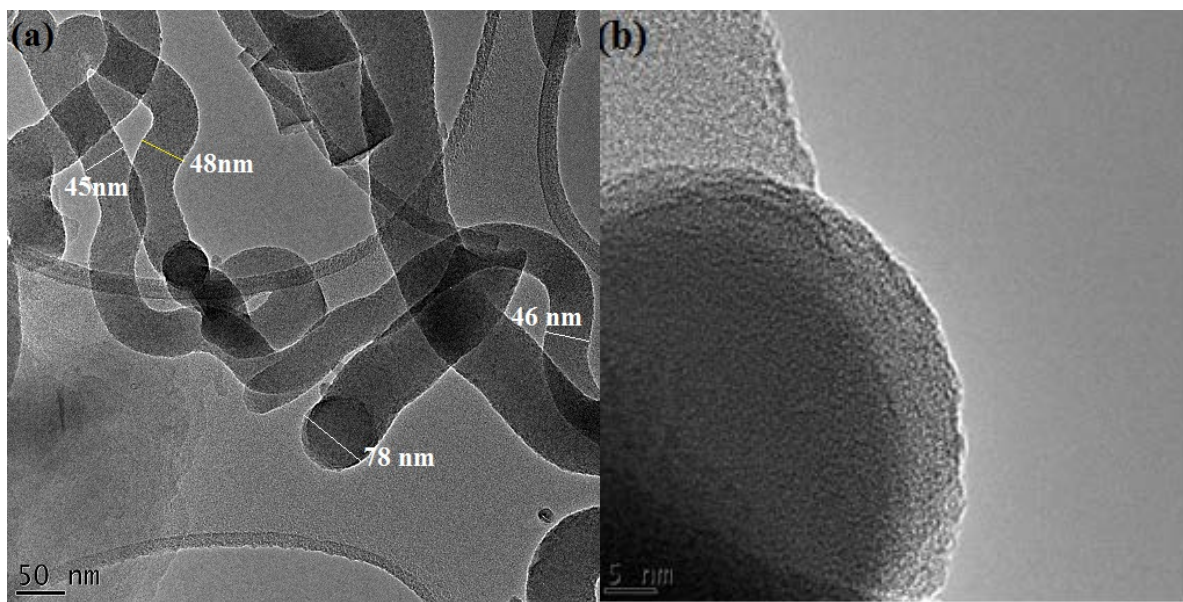


**Figure 3.23:** BF images showing; (a) randomly oriented broken Si nanowires, (b) a spherical tip of one of the wires.

These TEM observations made in figure 3.23 are in full agreement with previous observations made in figure 3.4, where by SEM micrographs revealed Si nanowires with spherical tips, suggesting the dominance of the VLS growth mechanism during the synthesis of Si nanowires. However, these observations do not nullify the possibility of other growth mechanisms such as OAG mechanism, since not all of the grown nanostructures have spherical tips [3.15].

In figure 3.24 (a) and (b), HRTEM BF images of the Si nanowire spherical tip are shown and these image show lattice fringes on the sample which indicate the presence of the Ni metal catalyst, encapsulated in a  $\text{SiO}_x$  amorphous matrix which then forms the whole spherical tip of the nanowire. This amorphous  $\text{SiO}_x$  shielding of the metal catalyst observed on this sample is similar to the observation made by Li *et al* [3.50]. The EDS spectrum shown (figure 3.24 (c)) confirms the presence of the nickel-silicide (Ni-Si) alloy which acts as a catalyst at the tip of the Si nanowire.

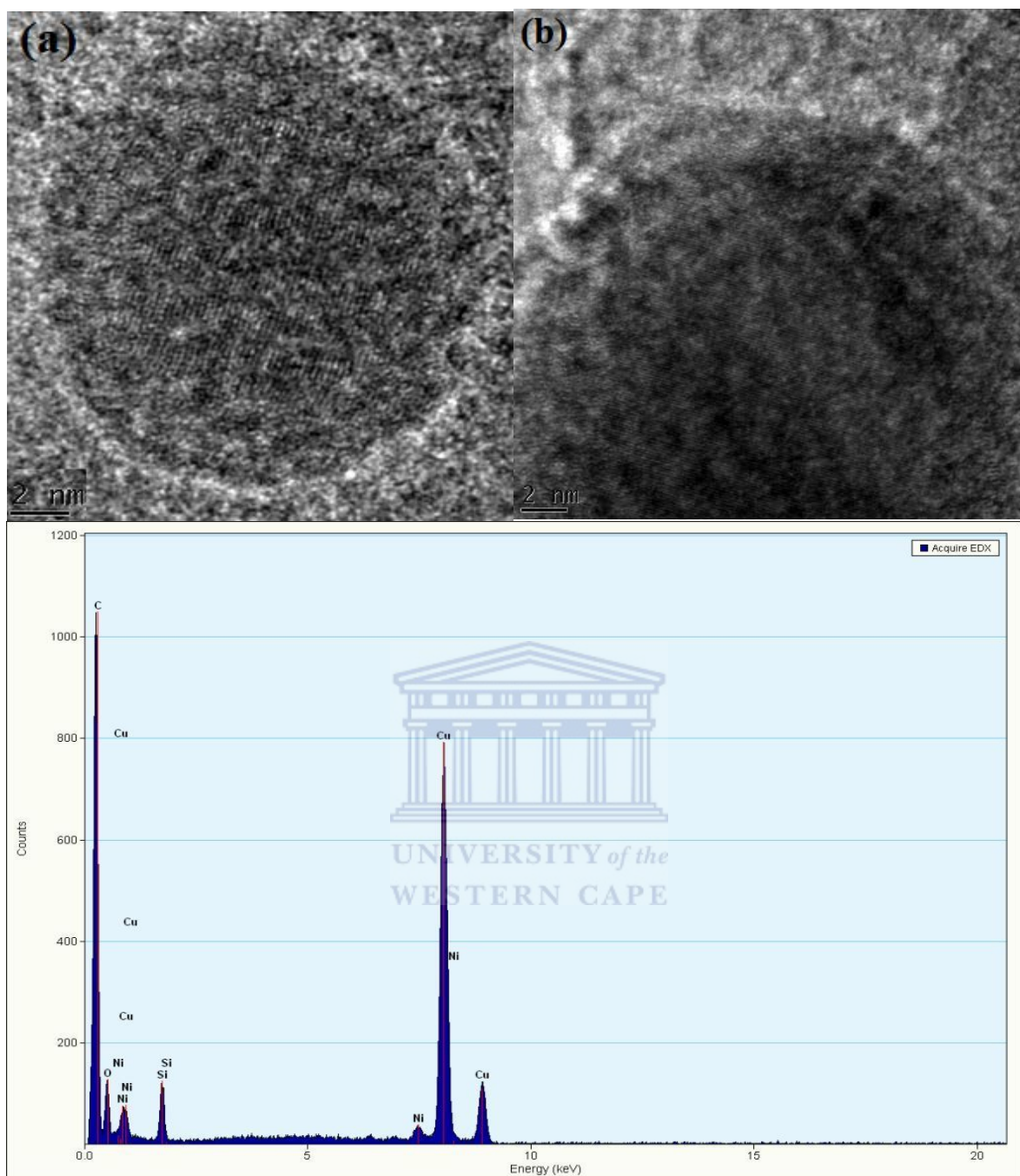


**Figure 3.24:** HRTEM BF images of the (a) encapsulated Ni-Si alloy (b) the Ni-Si lattice fringes, and (c) the EDS spectrum taken around the spherical tip.

The presence of this Ni-Si nanoparticles at the Si nanowire tip show that the Ni catalyst was responsible for the nucleation and growth of Si nanowires on this sample which confirms the VLS growth mechanism. Closer inspection of the shape of the interface between the Ni particle and the nanowire body reveals a round shape which indicates that the catalyst was molten into a liquid at the eutectic

temperature of about  $964^{\circ}$ . This further confirms the VLS growth mechanism being responsible for the observed nanostructures [3.50].

The EDS results obtained during HRTEM analysis depict that the approximate chemical composition of the nanowire tip consists of Si and O due to the  $\text{SiO}_x$  surrounding the Ni catalyst particle responsible for the Ni peak. This confirms the presence of  $\text{SiO}_x$  and  $\text{NiSi}$  phases and is in agreement with the X-Ray analysis results obtained previously. The Cu and C peaks shown in the results are signals from the TEM grid used to support the nanostructures for analysis [3.50].

Furthermore, from these EDS results, it is interesting to observe that the body of the nanowires is composed of oxidised Si ( $\text{SiO}_x$ ) which correlates with the morphological observations made in figure 3.23 (a) since  $\text{SiO}_2$  nanowires are expected to have a helical or bent shape due to their amorphous nature [3.51]. Additionally, we can conclude that these grown structures are indeed Si nanostructures since these obtained results are independent of the Si influence from the substrate and Ni from the deposited Ni thin film. This observation correlates with previous EDS results obtained during SEM analysis which also indicated the presence of Si, Ni and O around and near the tip. It can therefore be concluded that the grown nanostructures can be classified as  $\text{SiO}_2$  nanowires with a Ni metal catalyst at the tip.

### **3.3.4.2 Scanning transmission electron microscopy (STEM)**

In the previous section, the grown Si nanostructures were extensively analysed using HRTEM to observe the internal structure and chemical composition of the grown material. This enhanced the understanding of the growth mechanisms and various growth process involved in the formation of the Si nanowires. However

during internal structure analysis of Si nanowires, it was deemed necessary to ascertain if the grown structures were hollow (tubes) or filled (wire/rod) structures hence the employment of the STEM technique in order to obtain a HAADF-STEM thickness mapping of the grown structures. During STEM, this was achieved by forming a focused beam of electrons that was used to conduct a line scan across (diameter) the body of the Si nanowire [3.52].

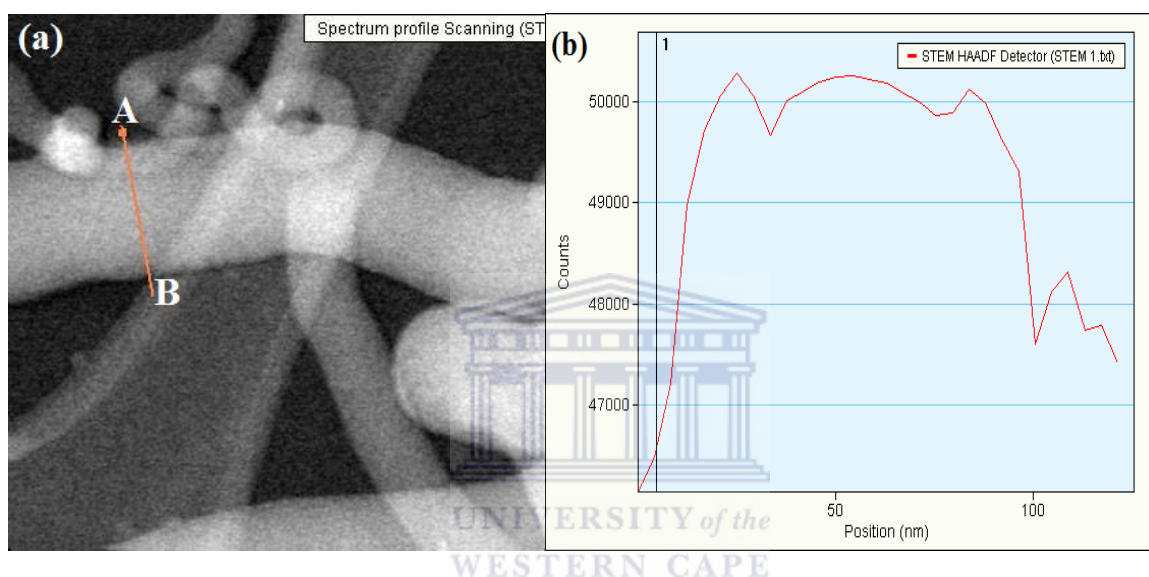


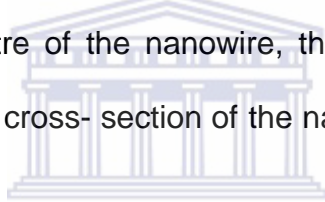
**Figure 3.25:** (a) shows a Dark-Field TEM image of a 100 nm thick SiO<sub>2</sub> nanowire and (b) shows a STEM thickness mapping of the SiO<sub>2</sub> nanowire.

The STEM analysis results presented in figure 3.25 shows a DF-TEM image (a) of a SiO<sub>2</sub> nanowire of about 100 nm, on which a line scan (A-B), along the diameter of the nanowire was conducted. The STEM thickness map shown in (b), represents the thickness variation across the diameter of the nanowire in (a), along the line AB.

On the DF-STEM image in figure 3.25 (a), the SiO<sub>2</sub> nanowires are represented by the individual or stacked, bright and cylindrical structures. The stacked nanowires are a consequence of the TEM sample preparation procedure used which lacks the ability to have a homogeneous distribution of the nanowires over the holey carbon copper grid. According to the work done by Heinrich *et al*, the signal intensity from

the HAADF detector increases with increasing sample thickness and atomic number (Z) [3.53], hence this technique can be used to probe the thickness variation along the cross section of the nanowires. On the thicker part of the sample, the incident electron beam is highly scattered over large angles resulting in a high intensity signal on the HAADF detector while thinner parts result in less scattering of the probing electron beam hence a lower signal intensity [3.54].

On the  $\text{SiO}_2$  nanowire thickness map shown in figure 3.25(b), a narrow sharp peak is observed on the edge nearer to the point A which indicates a higher intensity than at the centre of the nanowire. This high intensity can be attributed to the stacking of nanowires over each other as observed in the image (a). At about half-way through the cross section, at the centre of the nanowire, there is no drop in the intensity signal which indicates that the cross-section of the nanowire is not a hollow or tube-like structure.



This constant intensity signal around the core of the nanowire shows that there is no variation in thickness of the sample cross-section [3.55]. In a hollow structure, the intensity counts would decrease for all the scan positions within that cavity range since there will be less scattering of the probing electron beam as a result of fewer atoms or less material along path of beam through that cross-section, scan position. From these observations, it can therefore be concluded that these grown nanostructures are  $\text{SiO}_2$  nanowires and not nanotubes.

### **3.3.4.3 Electron energy-loss spectroscopy (EELS) of Si nanowires**

Transmission electron microscopy (TEM) is one of the most superior elemental analysis techniques, with a spatial energy resolution due to thin TEM samples having a shallow interaction volume. During TEM-EDS, an x-ray based technique, only a

fraction of resultant x-rays carrying sample information are collected in the detectors hampering the efficiency and accuracy of the technique [3.56].

However, during STEM-EELS, the EEL spectrometer is placed at the bottom of the TEM column and is along the path of the electron beam hence a high percentage of the inelastically scattered (energy-loss) electrons with elemental fingerprints are easily collected in the spectrometer. Therefore, EELS is capable of giving higher signal-collection efficiency within a small volume of material, ensuring that EELS is one of the best chemical analysis techniques for nanostructures. In this work, EELS was done on the grown Si nanowires to confirm the presence of  $\text{SiO}_2$  as predicted by EDS measurements.

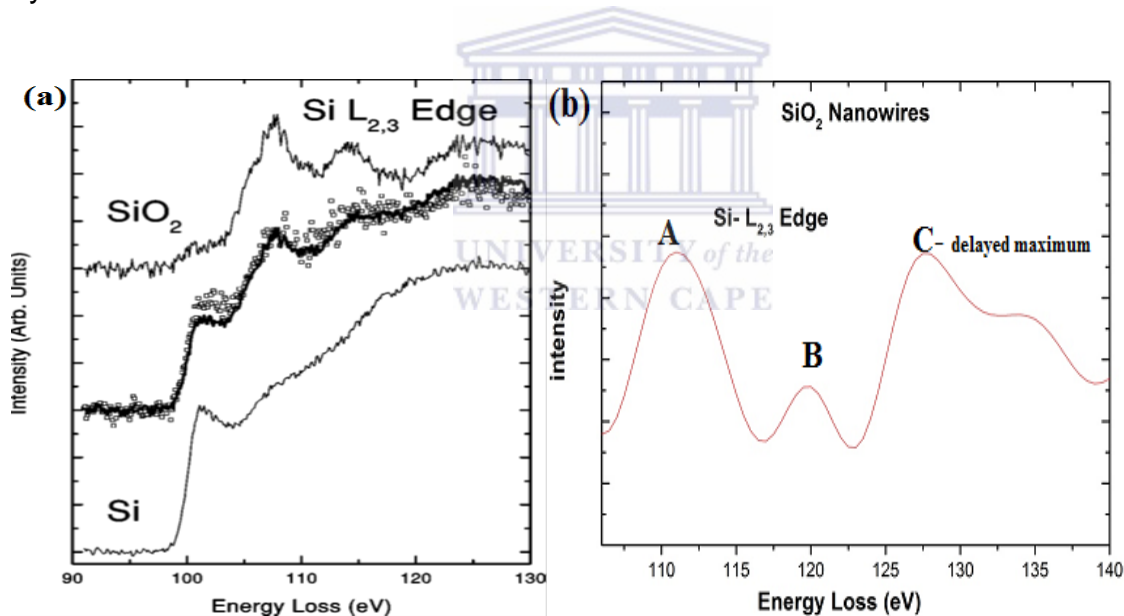


**Figure 3.26:** shows the energy loss  $\text{Si L}_{2,3}$  edge spectra for (a) a typical  $\text{SiO}_2$  and Si eels reference spectra [3.57], (b) the grown  $\text{SiO}_2$  nanowires.

In figure 3.26 (a), a typical reference  $\text{Si L}_{2,3}$  spectrum for  $\text{SiO}_2$  (top), Si (bottom) and experimental data are presented [3.57]. The EELS spectra of the near-edge structure of a thin  $\text{SiO}_2$  layer shown, is characterised by the main peak at 108 eV, middle peak at 115 eV and the delayed maximum peak at 128 eV.

In figure 3.26 (b), the presented eels spectrum shows the characteristic Si L<sub>2,3</sub> edge peaks obtained from the grown SiO<sub>2</sub> nanowires. These experimental results focus on the energy-loss near edge structure (ELNES) which is marked by an edge onset at about 106 eV and terminates with a delayed maximum peak at about 130 eV. This region is composed of the main peak A, at 110 eV followed by another less intense peak B at about 120 eV, which is separated by a deep trough from the delayed maximum peak C at about 130 eV. These characteristic features of the ELNES can be understood using the single electron theory where by, excitation of an electron from an inner-shell to an unoccupied state is ascribed to the well-defined energy and angular momentum of inner-shell states. [3.58].

The results obtained from this work exhibit a correlation with the findings made by Botton *et al*, presented in (a) [3.57] and Garvie *et al* [3.59] for amorphous SiO<sub>2</sub>. However, in comparison, slight peak shifting (blue-shift) is observed on all the major ELNES peaks of the SiO<sub>2</sub> nanowires shown in (b). According to Garvie, the ELNES edge onset represents the conduction band (CB), hence this observed shifts can be attributed to the upshifting of the CB (confinement effects) in the 1-dimensional nanostructured SiO<sub>2</sub> nanowires. According to Botton *et al*, such discrepancies can be a consequence of the differences in the energy dependence of the extrapolated EELS background in addition to plural scattering contributions. Theoretical errors in self energy calculations and negligence of nonspherical potential corrections can also contribute to such discrepancies [3.60].

These onset energies therefore correspond to the electron transitions into lower unoccupied s-like states which consequently result in the formation of the main peak A. The formation of the second peak B, at 120 eV, can be attributed to transitions

---

into states with both s and d-like characteristics while the broad delayed maximum is a consequence of weak structure [3.59].

Based on previous and current observations, it is evident the ELNES of the grown nanowires is in full agreement with the  $\text{SiO}_2$  ELNES data available from literature hence we can qualify the grown structures as amorphous  $\text{SiO}_2$  nanowires. This observation is in accordance with the results obtained from SEM-EDS, FTIR and TEM-EDS which suggested formation of  $\text{SiO}_2$  nanostructures and further highlighted the possible oxygen sources during growth.

### **3.4 OPTICAL PROPERTIES of $\text{SiO}_2$ NANOWIRES**

Silicon (Si) is a material that has a wide range of applications in the electronic and photonic industry. One of the reasons is that, Si can be thermally oxidised cost effectively to form  $\text{SiO}_2$  which is stable and non-toxic. However, the indirect band gap of bulk Si makes it a less desirable material for optical absorption and emission applications since electron recombination requires a phonon interaction. This implies that thick layers of Si are required to efficiently absorb light, while the light emission is inefficient.

One of the several measures have been undertaken to address such limitations include the use of Si nanostructures such as SiNWs, which have a high surface area-to-volume ratio and diameters in the order of tens or hundreds of nanometres. Such low dimension, Si nanostructures, have been found to exhibit highly enhanced antireflective properties and strong absorption in comparison to their bulk c-Si counterparts. Furthermore, small diameter ( $\approx 10$  nm) SiNWs have demonstrated photoluminescence behaviour within the visible range when excited using a laser beam.

To investigate the optical and electronic (optoelectronic) properties of the as-grown  $\text{SiO}_2$  nanowires, ultraviolet-visible (UV-VIS) and photoluminescence (PL) spectroscopy were employed to characterize the samples.

### 3.4.1 Photo-Luminescence (PL) of $\text{SiO}_2$ Nanowires

The photoluminescence (PL) properties of the grown  $\text{SiO}_2$  nanowires are very crucial in understanding their optical properties and potential opto-electronic applications of these novel structures. The PL spectrum from the grown  $\text{SiO}_2$  nanowires is presented in figure 3.27 obtained after using a Xe 325 nm laser beam.

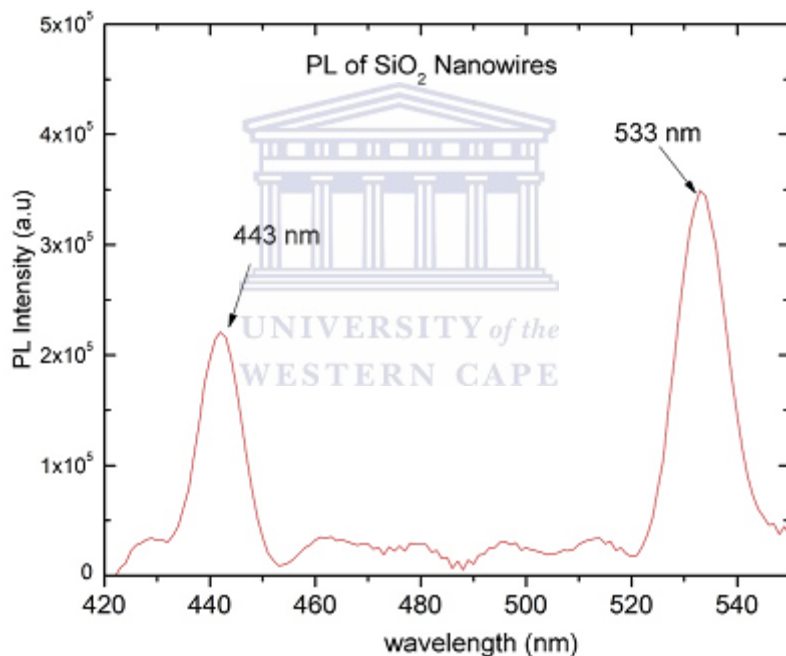


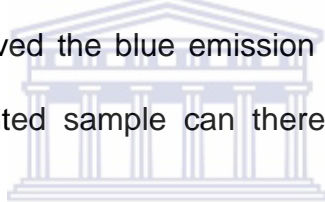
**Figure 3.27:** The PL spectra of  $\text{SiO}_2$  nanowires grown at  $1000\text{ }^\circ\text{C}$  using a TCVD furnace.

The PL spectra shown in figure 3.27, presents the two characteristic PL peaks of amorphous  $\text{SiO}_2$  nanowires. From this PL spectrum two distinguishable , a blue emission peak is observed at a wavelength of about 443 nm (2.8 eV), followed by a strong intensity green emission peak centred at about 533 nm (2.33 eV). In other extensive PL investigations, Wang *et al.* [3.61] found that  $\text{SiO}_2$  nanowires exhibit a

---

single weak peak around 600 nm, whereas Yu *et al.*[3.62] identified two separate broad peaks at about 420 nm and 470 nm which was in partial agreement with the 430 nm and 570 nm peaks observed by Zhu *et al.* [3.63].

The presented PL results obtained from the as-grown SiO<sub>2</sub> nanowires can be seen that they are in full agreement with current literature and the slight variations in peak positions within the 410-470 nm range, can be linked to the different synthesis methods used and the different diameters of the nanowires [3.64]. The blue emission peak observed at about 443 nm (2.8 eV) is a result of the oxygen vacancies (=Si=Si=) in SiO<sub>2</sub> nanowires caused by the insufficient oxygen supply from remnant and traces of impurity oxygen in carrier gas [3.64, 3.65]. In his work of SiO<sub>2</sub> thin films, Nishikawa *et al.* [3.66], observed the blue emission peak at about 2.7 eV and this shift observed on the presented sample can therefore be attributed to quantum confinement effects.

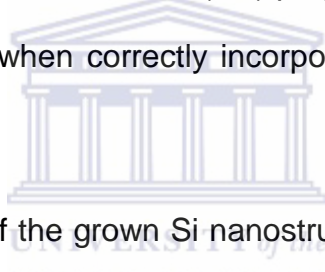


The high intensity, sharp green emission peak observed at 533 nm (2.33 eV) can also be attributed to the oxygen deficiencies during the growth of the SiO<sub>2</sub> nanowires. Furthermore, this peak can be linked to structural defects such as a lone-pair of two fold coordinated Si atoms in SiO<sub>2</sub> which act as radiative recombination centers [3.67]. According to Kim *et al.* [3.64], the photoluminescence of nanowires originates from their surface. This explains the high intensities (order of 10<sup>5</sup>) observed in both the blue and green emission peaks since nanowires have a larger surface area to volume ratio. In his work, he further demonstrated experimentally that, there is a direct relation between the PL intensity and the surface area of the nanowires.

Based on the experimental PL data obtained, it can be concluded that the PL emission peaks observed originate from the defect states (oxygen vacancies) due to oxygen dangling bonds found on the surface of the NWs. As mentioned earlier, such defects are induced by the insufficient oxygen during growth of NWs. This was proven by Kim *et al* whereby he demonstrated a huge reduction of the defect states by post-annealing SiO<sub>2</sub> nanowires in an oxygen-rich environment.

### **3.4.2 UV-VIS-NIR Spectroscopy of SiO<sub>2</sub> Nanowires**

Recently, Si-based nanostructures have been proposed as ideal candidate materials for enhancing light trapping in photo-voltaic solar cells. Nanostructures such as SiO<sub>2</sub> nanowires, exhibit tremendous antireflective (AR) properties, which can enhance the light absorption in solar cells when correctly incorporated within the geometry of a solar cell [3.68].



In this work, the reflectivities of the grown Si nanostructures were investigated using UV-VIS-NIR spectroscopy and compared to those of a bare Si wafer. The UV-VIS reflectance measurement results of different structures grown under different conditions are presented in figure 3.28, within the spectral range of 200 to 800 nm.

Figure 3.28 (a) shows the reflectance spectra of a bare Si wafer which was also used as a substrate for the growth of the other structures. This spectrum exhibits the typical behaviour of a c-Si with a high reflectance of about 70 % at the far ultraviolet (FUV) band (100-200 nm) and drops gradually to about 35% in the VIS-NIR band (400-800 nm). This spectrum can be further characterised by the presence of the characteristic reflection peaks of c-Si at about 272 nm and 365 nm. These observations are analogous to those made by Timoshenko *et al* [3.69] and Hasan *et*

al. [3.70] where by, they observed high reflectance in the UV band followed by a gradual drop in the VIS and NIR regions.

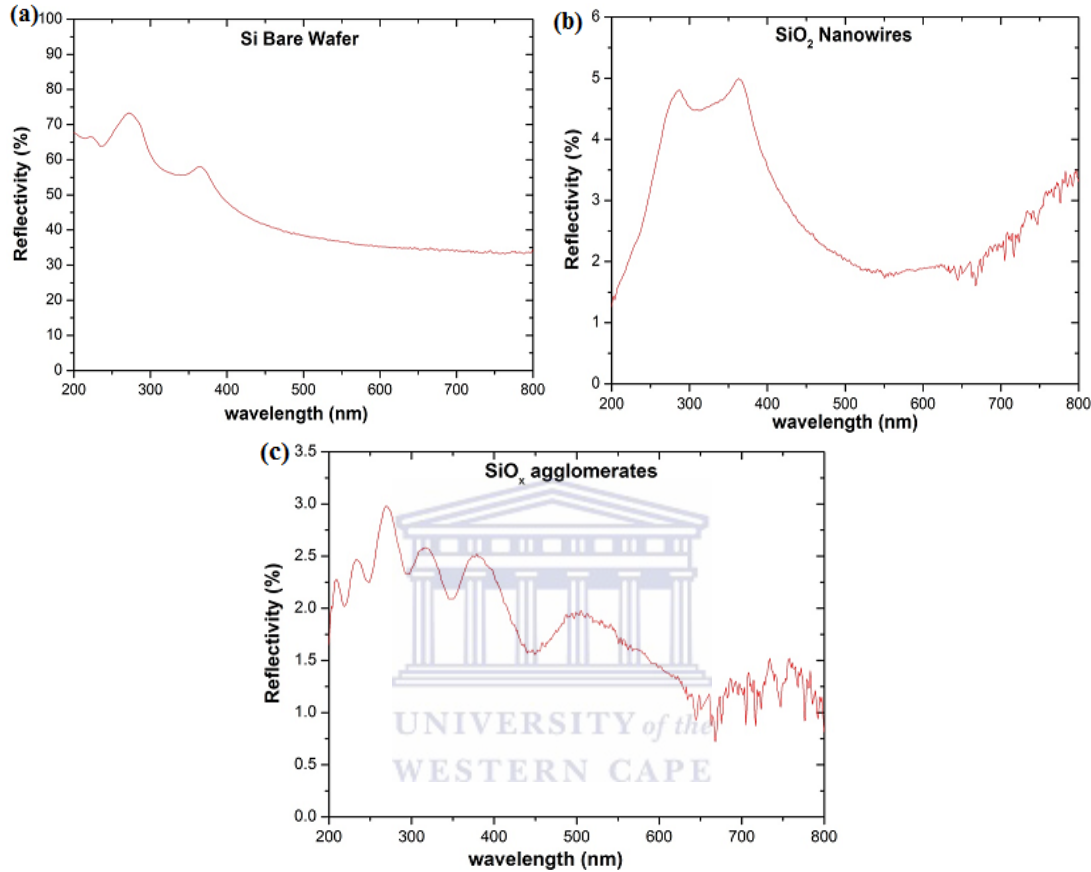


**Figure 3.28:** The reflectance spectra of (a) a bare Si wafer (b) SiO<sub>2</sub> nanowires grown at 1000 °C (c) SiO<sub>x</sub> structures grown at 1200 °C.

In figure 3.28 (b), a reflectance spectrum measured from a sample with a Si substrate coated with SiO<sub>2</sub> nanowires of various diameters below 100 nm (figure 3.8 (b)). This sample exhibits very good antireflective properties, with the reflectivity dropping down to about 1.5% in the FUV region (122-200 nm) and then a sudden rise within the middle ultraviolet (MUV) band (200- 300 nm) to about 4.5%. Maximum reflection of about 5% by the SiO<sub>2</sub> nanowires is observed within the near ultraviolet (NUV) band (300-400 nm). Beyond this region, the reflectance drops down

back to about 1.5% within the visible range until it starts rising again in the NIR band at about 800 nm.

Figure 3.28 (c) shows a UV-VIS reflectance spectrum of a sample grown at 1200 °C on which there was no SiNW growth. This sample consisted of a substrate covered by  $\text{SiO}_x$  structures of random shapes and agglomerates of the Ni metal catalyst nanoparticles (figure 3.8 (a)). Even though this sample had no nanostructures, the reflectance spectra reveals excellent AR properties starting with a very low reflectivity of about 2% in the FUV region. In the MUV band, the maximum reflectance obtained was about 35 which there after continue to drop until it reaches about 1.5 % in the visible and NIR regions. This sample also exhibits numerous reflection peaks in the range 200- 500 nm.

The reflectance spectrum of the Si bare wafer is characterised by high reflectivity and the two characteristic bands in the ultraviolet region. These two bands are common features of a c-Si spectrum and can be attributed to the optical transitions that occur near the direct band gap [3.71]. The sample coated with  $\text{SiO}_2$  nanowires exhibited a drastic reduction in reflectivity to less than 5% compared to the 70% of the c-Si. These results demonstrate the superior AR properties of  $\text{SiO}_2$  nanowires which enhance their light trapping ability making them potent materials for photovoltaic applications. These observations are in agreement with the observations made by Swain *et al.* [3.72], whereby he achieved drastic reduction in the reflectance of SiNWs grown at different oxygen ambients. Such characteristics were attributed to the surface defects on the enhanced surface area of nanowires. At the surface, the defect concentration can be as much as  $10^{12} \text{ cm}^{-2}$  due to dangling bonds and other defects which then act as surface traps, minimising the reflection [3.72].

---

The Sample grown at 1200  $^{\circ}\text{C}$  also demonstrated good AR properties dropping the reflectance to about 5%. On this sample, the combination of  $\text{SiO}_x$  structures combined with the Ni nanoparticles can be linked to the tremendous drop in reflectivity as observed by Spinelli *et al.* [3.73]. Over and above the enhanced AR due to the  $\text{SiO}_x$  defects, the Ni nanoparticles act as plasmonic AR coatings. Such characteristics can be attributed to the plasmon resonances associated with metal nanoparticles, leading to resonant scattering hence reducing the reflectivity drastically over the broad spectral range [3.74].

### 3.5 CONCLUSION

Silicon nanostructures were successfully synthesised using a 3-zone TCVD furnace. These nanostructures were further characterised using several techniques such as SEM, EDS, XRD, FTIR, HRTEM, STEM, EELS, PL and UV-VIS-NIR. During the investigation, Ni was found to be the ideal metal catalyst to be used for the synthesis of the Si nanostructures.

The effect of temperature on the growth of Si nanostructures was investigated and the ideal temperature for the growth was found to be 1000  $^{\circ}\text{C}$ . This temperature was the mid value for the series of temperatures investigated and yielded the ideal Si nanostructures. The position of the substrate relative to the source was also found to be one of the factors affecting the growth of Si nanostructures. The ideal substrate position for optimal growth of the Si nanostructures was found to be 11 cm from the source.

The TEM imaging results revealed that the grown Si nanostructures were amorphous SiNWs, which was in agreement with XRD results observed earlier. Further analysis using STEM confirmed that the grown Si nanostructures were not

---

hollow or tube-like, but nanowires. The EELS technique confirmed that the grown SiNWs were fully oxidised and characteristic of  $\text{SiO}_2$  nanowires, which was in agreement with the FTIR observations made initially.

The optical measurements conducted on the grown  $\text{SiO}_2$  nanowires revealed very good photoluminescence properties that are characteristic of  $\text{SiO}_2$  nanowires. UV-VIS-NIR spectroscopy of the grown structures exhibited very low reflectivity, rendering them as ideal materials for antireflective (AR) coatings for solar cell applications.



---

### **3.6 REFERENCES**

- 3.1. P. R. Bandaru, P. Pichanusakorn, *Semicond. Sci. Technol.* 25 (2010) 024003
- 3.2. H. W. Kim, S. H. Shim, J. W. Lee, *Physica E*. 37 (2007) 163-167
- 3.3. S. Wan, Y. Yu, J. Zhang, *J. Non-Cryst. Sol.* 355 (2009) 518-520
- 3.4. G. C. Yi, in ‘*Semiconductor Nanostructures for Optoelectronic Devices*’, Springer- Verlag publishers, Berlin Heidelberg (2012)
- 3.5. C. S. Kong, MSc Thesis, University of Malaya, Kuala Lumpur (2005)
- 3.6. K. W. Kolansiki, *Curr. Opin. Solid State Mater. Sci.* 10 (2006) 182-191
- 3.7. Y. Wang, V. Schmidt, S. Senz, U. Gosele, *Nat. Nanotechnol.* 1 (2006) 186-189
- 3.8. Y. Y. Wong, M. M. Yahaya, M. Salleh, B. Y. Majlis, *Sci. Technol. Adv. Mater.* 6 (2005) 330-334
- 3.9. S. T. Lee, N. Wang, C. S. Lee, *Mat. Sci. Eng., B* 286 (2000) 16-23
- 3.10. G. Cao, in ‘*Nanostructures & nanomaterials: synthesis, properties & applications*’, Imperial College Press publishers. (2004)
- 3.11. V. Schmidt, J. V. Wittemann, S. Senz, U. Gosele, *Adv. Mater.* 21 (2009) 2681-2702
- 3.12. N. Wang, Y. H. Tang, Y. F. Zhang, C. S. Lee, S. T. Lee, *Phy. Rev. B.*, 58 (24) (1998) 16024-16026.
- 3.13. A. Klimovskaya, A. Sarikov, Y. Pedchenko, A. Voroshchenko, O. Lytvyn, A. Stadnik, *Nanoscale Res. Lett.*, 2011, 6:151.
- 3.14. H. J. Choi, J. G. Lee, *J. Mater. Sci.* 30 (1995) 1982
- 3.15. C.C. Battner, M. Zacharias, *Appl. Phys. Lett.* 89, 263106 (2006)
- 3.16. F. M. Kolb, H. Hofmeister, R. Scholz, M. Zacharias, U. Gösele, D. D. Ma, S. T. Lee, *J. Electrochem. Soc.* 151 (2004) G472

- 
- 3.17. S. Dhara, P. K. Giri, Int. J. Nanosci. 10, (2011) 13
- 3.18. S. D. Hutagalung, A. Ahmad, K. A. Yacoob, Sol. Sta. Sci. Techno. 16(1), (2008) 100-106.
- 3.19. J. H. Song, D. H. Lim, E. S. Oh, M. H. Cho, J. Korean. Phys. Soc. 57(6), (2010) 1467-1471
- 3.20. J. Niu, D. Yang, J. Sha, J. N. Wang, M. Li, Mat. Lett. 61, (2007) 894-896
- 3.21. Q. Hu, H. Suzuki, H. Gao, H. Araki, W. Yang, T. Noda, Chem. Phys. Lett. 378, (2003) 299-304
- 3.22. L. Cui, W. W. Xia, F. Wang, L. J. Yang, Y. J. Hu. Phys. Rev. B. 409(2013) 47-50
- 3.23. C. T. Kirk, Phys. Rev. B 38, (1998) 1255
- 3.24. K. Liu, Q. Feng, Y. Yang, G. Zhang, L. Ou, Y. Lu, J. Non-cryst. Solids. 353, (2007) 1534-1539.
- 3.25. G. E. A. Swann, S. V. Patwardhan, Clim. Past. 7, (2011) 65-74.
- 3.26. M. Bashouti, K. Sardashti, J. Ristein, S. Christiansen, Nanoscale Res. Lett. 8(41), (2013)
- 3.27. P. H. Gaskell, D. W. Johnson, J. Non-Cryst. Solids. 20, (1976) 171
- 3.28. N. Gabrielyan, K. Saranti, K. N. Manjunatha, S. Paul, Nanoscale Res. Lett. 8(83), (2013)
- 3.29. T. Murakami, B. Froment, V. Carron, M. Ouaknine, W. S. Yoo, Electrochem. Soc. Meeting, 203, (2003).
- 3.30. V. K. Pecharsky, P. Y. Zavalij, in ‘Fundamentals of powder diffraction and structural characterization’. Boston: Kluwer academic publishers, 2003
- 3.31. C. van Bockstael, PhD Thesis, University of Ghent, Belgium (2010).
- 3.32. D. Connetable, O. Thomas, J. Alloys. Compd. 509, (2010) 2639-2644

- 
- 3.33. R. Doering, Y. Nishi, in 'Handbook of semiconductor manufacturing technology', CRC Press (2007) 10-24
- 3.34. J. Kim, E. S. Lee, C. S. Han, Y. Kang, D. Kim, W. A. Anderson, Micro. Electro. Eng. 85, (2008) 1709-1712.
- 3.35. N. K. Hassan, M. R. Hashim, M. A. Mahdi, N. K. Allam, J. Sol. Sta. Sci. Techno. 1(2), (2012) 86-89
- 3.36. F. J. Li, S. Zhang, J. Lee, Thin Solid Films 558 (2014) 75-85
- 3.37. J. G. Stark, H. G. Wallace, Chemistry data book, International Ideas, (1982)
- 3.38. L. Pavesi, R. Turan, in 'Silicon nanocrystals: fundamentals, synthesis and applications', John Wiley & Sons, (2010) 341
- 3.39. RREF
- 3.40. S. Verma, in 'Optimizing the metal-induced growth of microcrystalline silicon for solar cells', ProQuest publishing, (2008)
- 3.41. C. Dertavernier, D. Deduytsche, J. Jordan-Sweet, C. Cabral,Jr, C. Lavoie, Electro. Chem. Soc. Transactions. 3(2), (2006) 131-138
- 3.42. D. J. Tweet, J. Maa, S. T. Hsu, Mater. Res. Soc. Meet. Proc. 670 (2001)
- 3.43. Y. C. Lin, Y. Chen, D. Xu, Y. Huang, Nano Lett. 10, (2010) 4721-4726
- 3.44. M. K. Datta, S. K. Pabi, B. S. Murty, Mater. Sci. Eng., A. 284, (2000) 219-225
- 3.45. H. Pan, S. Lim, C. Poh, H. Sun, X. Wu, Y. Feng, J. Lin, Nanotechnology. 16, (2005) 417-421
- 3.46. S. T. Lee, N. Wang, C.S. Lee, Mater. Sci. Eng., A. 286, (2000) 16-23
- 3.47. S. Wan, Y. Yu, J. Zhang, J. Non-Cryst. Solids. 355, (2009) 518-520
- 3.48. P. Farzinpour, A. Sundar, K. D. Gilroy, Z. E. Eskin, R. A. Hughes, S. Neretina, Nanotechnology. 23 (2012) 495604 (10pp)
- 3.49. P. Pignalosa, H. Lee, L. Qiao, M. Tseng, Y. Yi, AIP Adv. 1, (2011) 032124

- 
- 3.50. F. J. Li, S. Zhang, J. Lee, J. Guo, T. J. White, B. Li, D. Zhao, *J. Cryst. Growth.* 404, (2014) 26-33
- 3.51. J. M. Bae, W. J. Lee, J. W. Ma, M. H. Cho, J. P. Ahn, H. S. Lee, *Nano. Res.* 5(3), (2012) 152-163.
- 3.52. S. J. Pennycook, in 'Advances in imaging and electron physics', Elsevier Science, New York, 123 (2002) 173-206
- 3.53. H. Henrich, B. Yuan, H. Nukala, B. Yao, *Mater. Res. Soc. Symp. Proc.* 1184, (2009)
- 3.54. H. Czichos, T. Saito, L. Smith, in 'Springer handbook of materials measurement methods', Springer Science and Business Media, (2009) 170
- 3.55. H. Nukala, MSc Thesis, University of Central Florida, Orlando, (2008) 28
- 3.56. S. Subramanian, G. Clark, K. Ly, T. Chrastecky, *EDFAOO*, 13 (1) (2011) 20-28
- 3.57. G. A. Botton, J. A. Gupta, D. Landheer, J. P. McCaffrey, G. I. Sproule, M. J. Graham, *J. Appl. Phys.* 91(5), (2002) 2912-2928
- 3.58. L. A. J. Garvie, P. R. Buseck, *Am. Mineral.* 84, (1999) 946-964
- 3.59. P. Rez, J. Bruley, P. Brohan, M. Payne, L. A. J. Garvie, *Ultramicroscopy*. 59, (1995) 159-167
- 3.60. A. L. Ankudinov, B. Ravel, J. J. Rehr, S. D. Conradson, *Phys. Rev. B*. 58, (1998) 7565
- 3.61. N. Wang, Y. H. Tang, Y. F. Zhang, C. S. Lee, I. Bello, S. T. Lee, *Chem. Phys. Lett.* 299, (1999) 237.
- 3.62. D. P. Yu, Q. L. Hang, Y. Ding, H. Z. Zhang, Z. G. Bai, J. J. Wang, Y. H. Zou, W. Qian, G. C. Xiong, S. Q. Feng, *Appl. Phys. Lett.*, 73, (1998) 3076

- 
- 3.63. Y. Q. Zhu, W. B. Hu, W. K. Hsu, M. Terrones, N. Grobert, T. Karali, H. Terrones, J. P. Hare, P. D. Townsend, H. W. Kroto, D. R. M. Walton, *Adv. Mater.*, 11, (1999) 844.
- 3.64. J. H. Kim, H. H. An, C. S. Yoon, *J. Appl. Phys.*, 105, (2009) 076102
- 3.65. Y. W. Wang, C. H. Liang, G. W. Meng, X. S. Peng, L. D. Zhang, *J. Mater. Chem.*, 12, (2002) 651-653
- 3.66. H. Nishikawa, T. Shirayama, R. Nakamura, Y. Ohki, K. Nagaswa, Y. Hama, *Phys. Rev. B*, 45, (1992) 586
- 3.67. Y. Li, A. Yang, X. Zheng, R. Peng, G. Zhai, X. Zhang, *Mater. Sci. Semicond. Process.*, 15, (2012) 428-431
- 3.68. A. K. Sood, A. W. Sood, R. E. Welser, G. G. Pethuraja, Y. R. Puri, X. Yan, D. J. Poxson, J. Cho, E. F. Schubert, N. K. Dhar, D. L. Polla, P. Haldar, J. L. Harvey, *Mater. Sci. Appl.*, 3, (2012) 633-639
- 3.69. V. Y. Timoshenko, K. A. Gonchar, I. V. Mirgorodsky, N. E. Maslova, V. E. Nikulin, G. K. Mussabek, Y. T. Taurbaev, E. S. Svanbayev, T. I. Taurbaev, *Nanoscale Res. Lett.*, 6, (2011) 349
- 3.70. M. Hassan, M. F. Huq, Z. H. Mahmood, *Springerplus.*, 2, (2013) 151
- 3.71. L. I. Belogorokhova, A. L. Belogorokhov, S. A. Gavrilov, Y. V. Timoshenko, P. K. Kashkarov, M. G. Lisachenko, S. P. Kobeleva, *Phys. Status Solidi A*, 197, (2003) 228-231
- 3.72. B. S. Swain, B. P. Swain, S. S. Lee, N. M. Hwang, *J. Phys. Chem. C*, 116, (2012) 22036-22042
- 3.73. P. Spinelli, V. E. Ferry, J. van de Groep, M. van Lare, M. A. Verschuuren, R. E. I. Schropp, H. A. Atwater, A. Polman, *J. Opt.*, 14 (2012) 024002  
K. R. Catchpole, A. Polman, *Appl. Phys. Lett.*, 93, (2008) 191113

---

# CHAPTER 4

## 4 SUMMARY AND CONCLUSION

---

In recent years, one-dimensional (1-D) silicon nanostructures have attracted a lot of attention from researchers as a highly progressive field of study. This trait can be attributed to the novel electronic, optical and mechanical properties which are a result of the size confinement effects in 1-D Si-nanostructures as opposed to their bulk material counterparts. Such properties render 1-D Si-nanostructures as favorable candidate materials for huge applications in mesoscopic, nanodevice and photovoltaic research. 1-D Si nanostructures such as Si nanowires can be synthesized using techniques such as chemical vapour deposition (CVD), plasma enhanced CVD, annealing in reactive atmosphere, thermal evaporation, molecular beam epitaxy and other solution based methods.

In this work, a thermal chemical vapour deposition (TCVD) system was successfully assembled and set up and the temperature of the system calibrated. Silicon nanostructures were successfully synthesized using the 3-zone TCVD furnace and characterized. The optimization of the system was done by investigating the effects of several deposition parameters on the growth, morphology and structural properties of the grown SiNWs. The parameters were the effect of metal catalyst used, growth temperature and the source-to-substrate distance.

The morphology, composition, internal structure (crystallography) and optical properties were investigated using several techniques including FESEM, EDS, FTIR, XRD HRTEM, STEM, EELS, PL and UV-VIS.

The results obtained during characterization show that thin, hair-like and solid-filled Si nanostructures were obtained during growth. This indicated that SiNWs, not tubes, were successfully synthesized using the 3-zone TCVD at atmospheric pressure.

The investigation on the effect of catalyst showed that the use of a metal catalyst during nanowire growth does enhance the growth of SiNWs. Furthermore SEM results indicated that nickel (Ni) was the most ideal metal catalyst to be used during the SiNW synthesis when compared to gold (AU).

The study of the effect of temperature indicated that the ideal growth temperature for SiNWs in our system was 1000 °C. The SEM results showed that there was no growth observed at the other investigated growth temperatures.

The source-to-substrate distance investigation showed that optimal growth of the SiNWs occurred at a distance of about 11 cm from the source. The substrate closer (5 cm) to the source had no growth on the surface while the farthest substrate at about 17 cm from the source did show some stunted growth.

The TEM imaging results revealed that the grown Si nanostructures were amorphous SiNWs, which was in full agreement with the XRD measurements observed earlier. Further analysis using STEM confirmed that the grown Si nanostructures were not hollow or tube-like, but nanowires.

The compositional analysis carried out using SEM-EDS, TEM-EDS indicated that there was substantial amount of oxygen present in the SiNWs. This observation was further confirmed using the EELS spectrum which showed the  $\text{SiO}_2$  characteristic ELNES peaks from the SiNWs implying heavy oxidation. These oxidised SiNWs were then classified as being  $\text{SiO}_2$  nanowires, which complement the bonding

---

information obtained from FTIR initially and the broad SiO<sub>2</sub> characteristic peak observed in XRD.

The optical measurements conducted on the grown SiO<sub>2</sub> nanowires revealed very good photoluminescence properties that are characteristic of SiO<sub>2</sub> nanowires. UV-VIS spectroscopy of the grown structures exhibited very low reflectivities, rendering them as ideal materials for antireflective (AR) coatings for solar cell applications.

From this study it can be concluded that oxidised SiNWs were successfully synthesized using a 3-zone TCVD system and the optimal growth parameters were found to be 1000 °C at a source-to-substrate of 11 cm in an argon ambient using Ni as the metal catalyst.

In future work, it can be recommended that the TCVD be upgraded into being a high vacuum system in order to be able to control the oxygen content and pressure during growth hence eliminating the unwanted oxygen.

